



## ATLAS NOTE

November 29, 2014

### Measurement of Color Flow in $t\bar{t}$ using Jet Pull

Kiran Joshi<sup>c</sup>, David López Mateos<sup>b</sup>, Benjamin Nachman<sup>a</sup>, Thomas Neep<sup>c</sup>, Yvonne Peters<sup>c</sup>,  
Matthew Schwartz<sup>b</sup>, Ariel Schwartzman<sup>a</sup>, Maximilian Swiatlowski<sup>a</sup>

<sup>a</sup>*SLAC, Stanford University*

<sup>b</sup>*Harvard University*

<sup>c</sup>*The University of Manchester*

#### Abstract

Weighted radial moments over the constituents of a jet have previously been shown to be an experimental handle on color connections between the initiating partons. This note presents a measurement of the distribution of one such moment, the *jet pull* angle for jets produced in  $t\bar{t}$  events with one leptonically decaying  $W$  boson using  $20.3 \text{ fb}^{-1}$  of data recorded with the ATLAS detector at  $\sqrt{s} = 8 \text{ TeV}$ . The jet pull angle distribution is unfolded to remove the distortions introduced from detector effects and the resulting particle level distribution is compared with several color flow models. The data are in good agreement with the nominal Standard Model color flow model, at around XYZ  $\sigma$  in a Gaussian equivalent Z score, and are incompatible with an inverted color flow model close to XYZ  $\sigma$ .

Not reviewed, for internal circulation only

## 17 **Contents**

18	<b>1 Introduction and Motivation</b>	3
19	<b>2 Jet Pull Definition</b>	4
20	<b>3 Monte Carlo Samples and Dataset</b>	6
21	3.1 2012 Dataset . . . . .	6
22	3.2 Detector Simulation . . . . .	6
23	3.3 List of Monte Carlo Samples . . . . .	6
24	3.4 Simulation for Exotic Color Flow . . . . .	7
25	3.4.1 Inverting the Color Structure . . . . .	8
26	3.5 Triggers . . . . .	8
27	<b>4 Object and Variable Definitions</b>	12
28	4.1 Variable Inputs: Jets, Tracks, and $b$ -tagging . . . . .	12
29	4.1.1 Clusters . . . . .	12
30	4.1.2 Jets . . . . .	13
31	4.2 Event Selection . . . . .	16
32	<b>5 Truth Studies</b>	20
33	5.1 Rivet implementation . . . . .	20
34	5.2 Comparisons of Truth Level Distributions . . . . .	22
35	<b>6 Comparisons</b>	25
36	6.1 Data/MC . . . . .	25
37	6.2 Fast versus Full Detector Simulation . . . . .	35
38	<b>7 Analysis Strategy</b>	41
39	7.1 Background Estimation . . . . .	41
40	7.2 Response Matrix Binning . . . . .	41
41	<b>8 Systematic Uncertainties</b>	46
42	8.1 Experimental Uncertainties . . . . .	46
43	Cluster Angular Resolution . . . . .	47
44	Cluster Energy Scale . . . . .	54
45	8.1.1 Detector-level comparisons . . . . .	57
46	8.2 Theoretical Uncertainties . . . . .	57
47	<b>9 Results</b>	64
48	9.1 Unfolding . . . . .	64
49	9.2 Unfolding Checks . . . . .	65
50	9.2.1 Number of Iterations . . . . .	66
51	9.2.2 Statistical Pull . . . . .	68
52	9.3 Cross-checks and closure tests . . . . .	69
53	9.4 Systematic uncertainties . . . . .	69
54	9.4.1 Unfolding non-closure . . . . .	70
55	9.4.2 Systematic uncertainty breakdown . . . . .	72
56	9.5 Unfolded Data . . . . .	74

57	<b>10 Summary and Conclusions</b>	<b>76</b>
58	<b>11 Todo List</b>	<b>77</b>
59	<b>A Simulation Details</b>	<b>83</b>
60	A.1 QCD octet electroweak boson . . . . .	83
61	<b>B Additional Experimentl Studies</b>	<b>85</b>
62	B.1 Jet Origin Correction . . . . .	85
63	B.2 Jet Angular Resolution from Track Jets . . . . .	90
64	B.3 Cluster Energy Modeling for non-isolated Tracks . . . . .	94

Not reviewed, for internal circulation only

## 65 1 Introduction and Motivation

66 Due to the confining nature of the strong force, measuring the chromodynamic connections between  
 67 partons produced in  $pp$  collisions at the Large Hadron Collider (LHC) directly is not possible. However,  
 68 some information from the color connections of partons is retained by the observable objects - collimated  
 69 streams of particles known as *jets*. This has been demonstrated by studying the event energy distribution  
 70 inside and between jets in events of various topologies. The first such measurement was by the JADE  
 71 collaboration in 3-jet events at PETRA [1]. The JADE collaboration reported that the third leading jet  
 72 in tri-jet events had a rather different composition than the leading or subleading jet in the same events  
 73 or the two leading jets in dijet events. Among other properties, it was found that these third (gluon-like)  
 74 jets had a broader distribution of energy and particle multiplicity as a function of distance from the jet  
 75 axis compared to the other (quark-like) jets. Comparison with the models of the time suggested that  
 76 this observation was in support of fragmentation along the color axes of the initiating partons. There is  
 77 now a variety of three-jet studies aimed at investigating this phenomena of *color coherence* performed at  
 78 PETRA [1, 2], PEP [3–6], Tevatron [7, 8], and LHC [9].

79 With center of mass energies large enough to produce on-shell  $W$  and  $Z$  bosons, the highest energy  
 80 experiments since LEP have studied color flow directly from the decay of heavy color singlets. For  
 81 instance, L3 [10] and DELPHI [11] studied hadronic diboson  $WW$  events in which the energy density  
 82 between jets associated with the same  $W$  decay compared to the density between jets from different  $W$   
 83 decays was found to be sensitive to the color flow of models used to describe the data. Additional studies  
 84 at LEP [12, 13] and the Tevatron [14] have used the known initial color state of the electroweak bosons  
 85 to constrain models of color flow in hadronic final states.

86 All of the studies described thus far have used either the distribution of energy within a jet or the dis-  
 87 tribution of energy between jets as sensitive observables to constrain models of color flow. The combina-  
 88 tion of the orientation and distribution of intrajet and interjet radiation can provide additional discriminat-  
 89 ing power. First defined in Ref. [15], the *jet pull* is a kinematic variable built from momentum-weighted  
 90 radial moments of jet constituents (*jet substructure*) combined with information from the relative orienta-  
 91 tions of jets in the event (*jet superstructure*) that was designed to be sensitive to the color flow between  
 92 the initiating partons of jets. Since its inception, jet pull has been suggested as a discriminating variable  
 93 to isolate color singlets such as Higgs bosons from color octets (e.g. gluons) as suggested in Ref. [16]  
 94 and used experimentally in Ref. [17–19].

95 The first experimental measurement of color connection using jet pull was performed in  $t\bar{t}$  events  
 96 with one lepton in the final state at D0 [20]. Such events provide a relatively pure sample of hadronically  
 97 decaying  $W$  bosons. By fitting the data with Monte Carlo (MC) templates constructed from the jet  
 98 pull distribution, exotic color flow models could be constrained directly. The purpose of this note is to  
 99 describe a study aimed at probing the color flow in  $t\bar{t}$  at the LHC, where the  $t\bar{t}$  cross section and integrated  
 100 luminosity are much higher than at the Tevatron. Furthermore, we will unfold the jet pull distribution to  
 101 correct for distortions from the detector reconstruction, in order to make the measurement available for  
 102 MC tuning or testing models of color flow beyond the Standard Model. The first such tests are performed  
 103 in this note by comparing the unfolded jet pull distribution with various model predictions. While many  
 104 models of beyond the SM leading order color flow in  $t\bar{t}$  are excluded by other experimental studies, there  
 105 are at least two important reasons for constraining models of exotic color flow with this measurement.  
 106 First, it is essential to calibrate the sensitivity of jet pull to the underlying color structure. This is needed  
 107 so that if new physics is discovered, jet pull can be reliably used to constrain its properties. A second  
 108 reason to measure the color structure in  $t\bar{t}$  is that there are feasible models which are unconstrained by  
 109 other experimental searches. For instance, leptophobic flavor changing neutral currents (FCNC) with  
 110 a mass near the  $W$  mass could avoid previous detection but could be observed using pull angle-related  
 111 techniques if they are not color singlets.

This note is organized as follows. Section 2 formally defines the jet pull angle and sets the notation and nomenclature. Section 3 describes all of the simulation and data samples. Section 4 details the object and event selection. Truth studies are shown in Section 5, data/MC control plots are in Section 6 and the analysis strategy is outlined in Section 7. Section 8 lists and describes all of the systematic uncertainties considered in the analysis. The results for the unfolded distribution and comparisons to beyond the SM leading order color flow models are in Section 9. Section 10 contains conclusions and future outlook.

Not reviewed, for internal circulation only

## 2 Jet Pull Definition

The pull vector for a given jet  $J$  is defined as

$$\sum_{i \in J} \frac{p_T^i |r_i|}{p_T^J} \vec{r}_i, \quad (1)$$

where the sum runs over constituents of the jet  $J$  and  $\vec{r}_i = (\Delta y_i, \Delta\phi_i)$  with respect to the position of the jet axis in rapidity ( $y$ ) - azimuthal angle ( $\phi$ ) space. Given the pull vector for jet  $J_1$ , a variable sensitive to the underlying color connections to another jet  $J_2$  is the angle the pull vector for  $J_1$  makes with respect to the vector connecting  $J_1$  and  $J_2$  in  $(\Delta y, \Delta\phi)$  [15]. This is shown graphically in Fig. 1 and will be called the *pull angle* and denoted  $\theta_P(J_1, J_2)$ . The pull angle is symmetric above zero when it takes values between  $-\pi$  and  $\pi$  and so henceforth,  $\theta_P(J_1, J_2)$  refers to modulus of the angle in  $(\Delta y, \Delta\phi)$  space with  $0 < \theta_P \leq \pi$ .

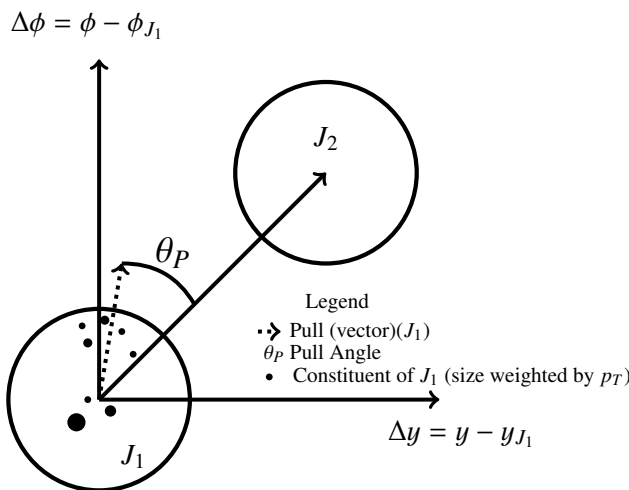


Figure 1: For a jet  $J_1$  with a set of constituents (calorimeter clusters, tracks, stable generator particles, or charged stable MC particles), one can compute the pull vector labeled as Pull (vector)( $J_1$ ). The sensitive variable is not the entire vector, but the angle,  $\theta_P$ , that this vector makes with respect to another specified jet  $J_2$ . Since the pull vector is weighted by  $p_T$  and  $\Delta R$  to the jet axis, large angle soft radiation can contribute just as much if not more than central hard constituents.

Reconstructed jets are clustered with the anti- $k_t$  algorithm [21] with radius parameter 0.4 from topological calorimeter clusters [22], treated as massless particles. Clusters are calibrated using the local cluster weighting (LCW) algorithm [23], and jets are calibrated to account for a reconstruction bias as well as to mitigate the contribution from pileup [24]. To investigate jet pull angle properties in simulation without the distortions arising from detector resolution, truth jets are formed from the four-vectors

<sup>131</sup> of Monte Carlo (MC) stable particles<sup>1</sup> as inputs to the anti- $k_t$   $R = 0.4$  clustering algorithm (see Sec. 5.1  
<sup>132</sup> for more details). More information about the objects used in the analysis is given below in Sec. 4.

<sup>133</sup> The jet pull vector is a weighted sum over jet constituents. Studies in this note exploit different sets  
<sup>134</sup> of jet constituents: for reconstructed jets, the nominal constituents are the calorimeter clusters used in the  
<sup>135</sup> jet construction (*calorimeter pull*). Truth jets correspondingly use all MC stable particles (*all particles*  
<sup>136</sup> *pull*). Alternatively, the tracks assigned to a jet can be used as constituents in the pull vector calculation  
<sup>137</sup> (*track pull*). These tracks<sup>2</sup> are required to have  $p_T \geq 500$  MeV and other criteria described in Sec. 4.  
<sup>138</sup> Tracks are associated to jets using ghost-association [25]: an assignment of tracks to jets by adding to  
<sup>139</sup> the jet clustering process *ghost* versions of tracks that have the same direction but infinitesimally low  
<sup>140</sup>  $p_T$ . The corresponding constituents in truth jets are the charged stable particles clustered within the jet  
<sup>141</sup> (*charged particles pull*). Note that in the case of reconstructed jets the jet axis is always determined  
<sup>142</sup> using the calorimeter, and for truth jets the jet axis is always determined using all stable particles. For  
<sup>143</sup> nomenclature, the all particles/calorimeter pull angle will be referred to as the pull angle or  $\theta_P$  and  
<sup>144</sup> decorated with the word ‘truth’ if the context is ambiguous. The charged particles/track pull angle will  
<sup>145</sup> be further decorated with the word ‘charged.’

<sup>146</sup> There are advantages and disadvantages for the track pull and likewise for the calorimeter pull. Both  
<sup>147</sup> constituent inputs are studied in parallel and the final result will either use one or both, depending on the  
<sup>148</sup> discrimination power and systematic uncertainty estimates.

<sup>149</sup> The pull vector contains information beyond simply the angle with respect to another jet in the event.  
<sup>150</sup> Define the jet pull vector magnitude  $|v_p(J)|$  as follows:

$$|v_p(J)| = \left| \sum_{i \in J} \frac{p_T^i |r_i|}{p_T^J} \vec{r}_i \right|.$$

<sup>151</sup> In dedicated phenomenological studies [16], it was shown that the pull magnitude is not useful in discriminating octet from singlet color states. However, it is a useful handle on the jet pull angle resolution [26].  
<sup>152</sup>  
<sup>153</sup> The jet pull vector magnitude can be considered a radial moment, with the radial distance  $\Delta R$  from the  
<sup>154</sup> jet axis weighted by the fractional constituent  $p_T$ .

<sup>155</sup> For a detailed discussion of the jet pull angle detector performance, please see Ref. [26].

---

<sup>1</sup> $c\tau > 10$  mm.

<sup>2</sup>The track momentum 3-vector is measured in the ATLAS tracker and each track is assigned the mass of the pion.

### 156 3 Monte Carlo Samples and Dataset

157 This section describes the datasets and Monte Carlo (MC) samples used in this analysis. All samples in  
 158 Analysis Object Data (AOD) format from official productions are converted into an NTuple (in the form  
 159 of a D3PD) in the COMMON format [27].

160 **3.1 2012 Dataset**

161 The raw data samples used in this analysis were recorded by the ATLAS detector over the period 5 April  
 162 – 6 December 2012, corresponding to runs 200841 to 215643 (data-taking periods A3 – L3). This  
 163 corresponds to an integrated luminosity of  $20.28 \text{ fb}^{-1}$  after application of basic data quality requirements  
 164 via the standard ATLAS Good Run List<sup>3</sup>. The uncertainty on the luminosity is 2.8% [28, 29]. The  
 165 analysis uses data from the Muon physics stream. The average number of interactions per  $pp$  bunch  
 166 crossing was 20.7.

167 **3.2 Detector Simulation**

168 Simulated events produced by Monte Carlo generators are processed with a full ATLAS detector and  
 169 trigger simulation [30] based on the Geant4 [31] toolkit and reconstructed using the same software  
 170 as the experimental data. The average number of additional  $pp$  collisions per bunch crossing (pileup  
 171 interactions) was 20.7 over the full 2012 run. The effects of pileup were modeled by adding multiple  
 172 minimum-bias events simulated with PYTHIA 8.160 [32], with the A2 tune and the MSTW2008LO PDF,  
 173 to the generated hard-scatter events. The distribution of the number of interactions is then weighed to re-  
 174 flect the pileup distribution in the 2012 data. All of the nominal MC samples are produced using the full  
 175 detector simulation. However, due to limited computing resources, some systematics variation samples  
 176 are produced using a fast simulation framework where the showers in the electromagnetic and hadronic  
 177 calorimeters are simulated using a parameterized description [33] and GEANT4 is used for the rest of the  
 178 detector (in particular for the tracking in the inner detector). The fast simulation framework is known to  
 179 work well for reproducing event kinematic properties, such as jet  $p_T$  spectra, but may not accurately cap-  
 180 ture the detector distortions of the distribution of energy inside of jets. Shower shapes are parameterized  
 181 for single pions (applied to all hadrons), electrons, and photons. These parameterizations accurately de-  
 182 scribe longitudinal shower properties (including fluctuations and correlations) but reproduces the lateral  
 183 shower properties only on average [33]. For further discussion on the fast versus full detector simulation,  
 184 see Sec. 6.2.

185 **3.3 List of Monte Carlo Samples**

186 The list of default Monte Carlo samples is given in Table 1. Top quark pair production is simulated using  
 187 the next-to-leading-order (NLO) generator PowHeg [34–36] with NLO parton density function (PDF) set  
 188 CT10 [37, 38] with parton showering from PYTHIA 6 using the Perugia2011C tune. A second NLO full  
 189 detector simulation sample is available using MC@NLO 4.06 [39, 40] with the NLO parton density function  
 190 (PDF) set CT10 [37, 38], and parton showering and underlying event modelled with fortran HERWIG [41]  
 191 and JIMMY [42], respectively. The single top ( $s$ -,  $t$ -, and  $Wt$ -channel) backgrounds are modeled with  
 192 Powheg and PYTHIA 6, as with the nominal  $t\bar{t}$ . The PDF set CT10f4 [37] is used for the  $t$ -channel and  
 193 CT10 is used for the  $s$ - and  $Wt$ -channels. For the  $Wt$ -channel, the ‘inclusive Diagram Removal’ (DR)  
 194 scheme is used for overlap with  $t\bar{t}$  (the ‘inclusive Diagram Subtraction’ (DS) scheme is used to asses  
 195 systematic uncertainties). The  $W$ +jets and  $Z$ +jets backgrounds are modelled with ALPGEN 2.1.4 [43],

---

<sup>3</sup>The official standard GRL for 2012 data (/afs/cern.ch/user/a/atlasdqm/grlgen/AllGood/data12\_8TeV.periodAllYear\_DetStatus-v61-pro14-02\_DQDefects-00-01-00\_PHYS\_StandardGRL\_All\_Good.xml) is used.

<sup>196</sup> PYTHIA 6 and the CTEQ6L1 PDF set (using the ‘on the fly’ (OTF) scheme [44]) with the application  
<sup>197</sup> of the Heavy Flavour Overlap (HFOR) tool. Dibosons are generated with fortran HERWIG using the  
<sup>198</sup> CTEQ6L1 PDF set. For all uses of PYTHIA 6, the version is 426.2 and the tune is the Perugia2011C  
<sup>199</sup> tune [45]. In addition, for all uses of HERWIG, the version is 6.520.2 and the tune is the AUET2 tune [46].

<sup>200</sup> Additional ATLAS samples for comparison and the evaluation of systematic uncertainties are given  
<sup>201</sup> in Table 2. In particular, fast detector simulation samples have been produced with PowHeg +PYTHIA 6  
<sup>202</sup> and PowHeg +HERWIG so that the showering model can be compared. The reconstructed fast simulation  
<sup>203</sup> is not used for the nominal part of the analysis - for further discussion on the fast versus full detector  
<sup>204</sup> simulation, see Sec. 6.2. Additional samples exist for standard theory uncertainties corresponding to  
<sup>205</sup> various scale variations. There are also centrally produced samples with different levels of CR in the  
<sup>206</sup> PYTHIA tuning. A low CR sample exists with the fast detector simulation and a ‘no’ CR tuning also  
<sup>207</sup> exists, but only at the initial evgen stage. It is not expected that CR, which is a color flow effect in the  
<sup>208</sup> parton shower will have a large impact on the pull distribution, which is mostly sensitive to the color flow  
<sup>209</sup> determined during the hard scatter. This is confirmed by some preliminary studies shown below and also  
<sup>210</sup> investigations from the BOOST2012 report [47], which show that the difference between PYTHIA and  
<sup>211</sup> HERWIG is larger than the difference in the pull distribution between various color reconnection tunes.  
<sup>212</sup> See Sec. 8.2 for more details.

<sup>213</sup> The MC samples with exotic leading order color flow are described in the next subsection.

Process	ID	ME	Shower+UE	Tune	PDF
$t\bar{t}$ (lepton filter)	117050	Powheg	Pythia6 426.2	P2011C	CT10
W+jets	Many <sup>4</sup>	Alpgen 2.1.4	Pythia6 426.2	P2011C	CTEQ6L1
Z+jets	Many <sup>5</sup>	Alpgen 2.1.4	Pythia6 426.2	P2011C	CTEQ6L1
Single Top, $s$ -channel	110119	Powheg	Pythia6 426.2	P2011C	CT10
Single Top, $Wt$ -channel	10140	Powheg	Pythia6 426.2	P2011C	CT10
Single Top $t$ -channel	110090,110091	Powheg	Pythia6 426.2	P2011C	CT10
Dibosons WW	105985	fHerwig	fHerwig 6.520.2	AUET2	CTEQ6L1
Dibosons WZ	105986	fHerwig	fHerwig 6.520.2	AUET2	CTEQ6L1
Dibosons ZZ	105987	fHerwig	fHerwig 6.520.2	AUET2	CTEQ6L1

Table 1: Default Monte Carlo samples.

ID	ME	Shower	Tune	PDF	Note
105200	MC@NLO	Herwig+Jimmy	AUET2	CT10	Fullsim, Alternative to Nom
117426	Powheg	Pythia6	P2012loCR	CT10	FastSim, reduced CR
105860	Powheg	Herwig+Jimmy	AUET2	CT10	FastSim
105861	Powheg	Pythia6	AUET2B	CT10	FastSim
117429	Powheg	Pythia6	P2012mpiHi	CT10	FastSim, high MPI
117836,40,42,46	Powheg	Pythia6	P2011C	CT10	Fullsim, various top quark masses
117209-10	AcerMC	Pythia6	AUET2B	CTEQ6L1	Fastsim More/Less ISR/FSR

Table 2: Additional central ATLAS  $t\bar{t}$  production samples used in this analysis.

### <sup>214</sup> 3.4 Simulation for Exotic Color Flow

<sup>215</sup> Described in this section is an exotic model of colorflow. An alternative model with the same phe-  
<sup>216</sup> nomenology is described in Appendix A.1 (not part of the main analysis). In the model described below,

217 the leading order color string between the two quark decay products from the on-shell  $W$  is inverted with  
 218 a  $b$ -quark. The second model (described in the appendix) is for a new boson with the same properties as  
 219 the  $W$ , except that it is a color octet instead of a singlet. It is produced via  $t \rightarrow Wb$  just as in the usual SM  
 220 top quark and decays into quarks. Phenomenologically, these two models are essentially the same. The  
 221 advantages of the flipped model is that there is an easy procedure for applying the flip to any simulated  
 222  $t\bar{t}$  samples for which an LHE file exists, as described in the next subsection.

### 223 3.4.1 Inverting the Color Structure

224 A sample event from a typical  $t\bar{t}$  LHE file is shown in the top panel of Fig. 2. The LHE contains only the  
 225 hard scatter information. The second and third columns give some particle identification information, the  
 226 fourth-sixth columns describe where in the event record the particles belong and the rest of the columns  
 227 list the particles quantum numbers. We are most interested in the column for the ‘color’ quantum number.  
 228 All of the MC generators use an large  $N_c$  limit and assign a new color-anti color whenever a color charge  
 229 is created (which is why in this figure they begin at 501). The first of the color columns is the color  
 230 and the second column is the anti-color. Color cannot be created or destroyed so the total color must  
 231 be the same at the end of the hard scatter (status 23) as it was in the beginning (status -21). The most  
 232 relevant numbers in the example in Fig. 2 are the color and anti-color of the quark and anti-quark decay  
 233 products of the  $W^-$ : 502. Note that the  $W^-$  and the  $\bar{t}$  are *removed from the event record*. This is one of the  
 234 drawbacks from the color-flipping procedure: the tops and  $W$  bosons participating in the color flipping  
 235 must be removed because otherwise PYTHIA will complain that an unphysical color flow has occurred.  
 236 Just before the  $W$  is removed, its decay products are identified and their color strings are flipped with  
 237 the  $\bar{b}$  in the event. This is seen in the lower panel of Fig. 2, where the quark from the  $W$  has color 502  
 238 while the anti-quark has color 503 (the anti-color from the original  $W$  is with the  $\bar{b}$ ). The color flipping is  
 239 also represented pictorially in the cartoon in Fig. 3, where the color flow in a Standard Model  $t\bar{t}$  event is  
 240 compared to that in which the color flip has been implemented. It is then critical that the particle numbers  
 241 and mothers are re-aligned since the showering models all have many internal consistency checks (for  
 242 all particles that have their mother removed, set the mother to 3 and 4). Some care must be taken for  
 243 generators that allow for  $b$  quarks in the PDF. In this case, identifying the quark with which to switch the  
 244 color must be taken with care - this is solved by checking for the parent of the  $b$  or  $\bar{b}$ .

245 Ten million total events have been generated (flipped) and LHE files have been created. The sam-  
 246 ples have been fully simulated and reconstructed and are listed in Table 3. Histograms comparing  
 247 NTUP\_TRUTH are shown in this section. Figure 4 shows an example plot comparing the pull vector  
 248 angle and pull vector magnitude distributions for the color flipped Powheg+Pythia with the nominal  
 249 (truth level) Powheg+Pythia. As expected, the nominal samples peak at zero for the pull angle between  
 250 the  $W$  daughters (in this case, chosen as the leading non  $b$ -jets) while the color flipped model is nearly  
 251 uniform. Figures 5 and 6 show the kinematic distribution for the  $W$  daughters, which as expected are  
 252 nearly identical between the two models. The pull vector angle in this case is sensitive to the differences  
 253 between the flipped and nominal color flows while the event kinematics are not. Figure 7 shows the  
 254 invariant mass of the two  $W$  daughters. Since the radiation pattern is altered between the two models, it  
 255 is not unexpected that the invariant mass is different. One may argue then that in this model, the invari-  
 256 ant mass could be used alongside the pull angle to differentiate the models. However, if a new massive  
 257 resonance decaying into hadronic final states is discovered, the mass will not be known ahead of time  
 258 and so only the pull angle will be able to distinguish octet from singlet.

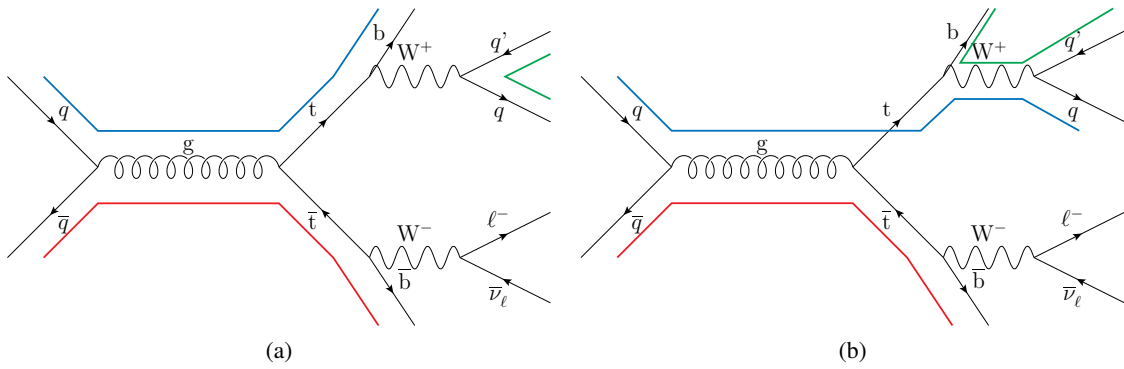
### 259 3.5 Triggers

260 This analysis makes use of single muon and single electron triggers. A logical OR between EF\_mu24i\_tight,  
 261 EF\_mu36\_tight, EF\_e24vhi\_medium and EF\_e60\_medium is used for the whole data taking period. The

----- PYTHIA Event Listing (hard process) -----										
no	id	name	status	mothers	daughters	colors	px	py	pz	
0	90	(system)	-11	0	0	0	0.000	0.000	0.000	8000.000
1	2212	(p+)	-12	0	0	3	0	0	0.000	0.000 4000.000 4000.000
2	2212	(p+)	-12	0	0	4	0	0	0.000	-4000.000 4000.000
3	21	(g)	-21	1	0	5	8	504	503	0.000 0.000 94.198
4	21	(g)	-21	2	0	5	8	501	504	0.000 0.000 -466.748 466.748
5	6	(t)	-22	3	4	9	10	501	0	81.617 -59.344 -265.703 333.045
6	-5	bbar	23	3	4	0	0	0	503	-0.916 -37.444 -61.245 71.944
7	3	s	23	3	4	0	0	502	0	-54.108 10.412 -0.850 55.107
8	-4	cbar	23	3	4	0	0	0	502	-26.593 86.377 -44.751 100.851
9	24	(W+)	-22	5	0	11	12	0	0	86.539 -59.228 -98.855 166.058
10	5	b	23	5	0	0	0	501	0	-4.922 -0.116 -166.849 166.988
11	-13	mu+	23	9	0	0	0	0	0	33.200 0.577 6.352 33.807
12	14	nu mu	23	9	0	0	0	0	0	53.339 -59.805 -105.207 132.250
Charge sum: 0.000				Momentum sum:				-0.000	0.000	-372.550 560.947
----- PYTHIA Event Listing (hard process) -----										
no	id	name	status	mothers	daughters	colors	px	py	pz	
0	90	(system)	-11	0	0	0	0	0.000	0.000	8000.000
1	2212	(p+)	-12	0	0	3	0	0	0.000	4000.000 4000.000
2	2212	(p+)	-12	0	0	4	0	0	0.000	-4000.000 4000.000
3	21	(g)	-21	1	0	5	8	504	503	0.000 0.000 94.198
4	21	(g)	-21	2	0	5	8	501	504	0.000 0.000 -466.748 466.748
5	6	(t)	-22	3	4	9	10	501	0	81.617 -59.344 -265.703 333.045
6	-5	bbar	23	3	4	0	0	0	502	-0.916 -37.444 -61.245 71.944
7	3	s	23	3	4	0	0	502	0	-54.108 10.412 -0.850 55.107
8	-4	cbar	23	3	4	0	0	0	503	-26.593 86.377 -44.751 100.851
9	24	(W+)	-22	5	0	11	12	0	0	86.539 -59.228 -98.855 166.058
10	5	b	23	5	0	0	0	501	0	-4.922 -0.116 -166.849 166.988
11	-13	mu+	23	9	0	0	0	0	0	33.200 0.577 6.352 33.807
12	14	nu mu	23	9	0	0	0	0	0	53.339 -59.805 -105.207 132.250
Charge sum: 0.000				Momentum sum:				-0.000	0.000	-372.550 560.947

Not reviewed, for internal circulation only

Figure 2: Snippets from an LHE file for a nominal color flow (top) and inverted color flow (bottom).

Figure 3: Cartoons showing the color flow present in (a) a leading order Standard Model  $t\bar{t}$  event, (b) a leading order  $t\bar{t}$  event with color flipping applied.

ID	ME	Shower	Tune	PDF	Note
117512	Powheg	Pythia6	P2011C	CT10	Fullsim, Inverted Color
117515	Powheg	Herwig+Jimmy	AUET2	CT10	Fullsim, Inverted Color

Table 3: Inverted color flow samples produced with the ATLAS production system.

262 offline selection is discussed in Sec. 4.

Not reviewed, for internal circulation only

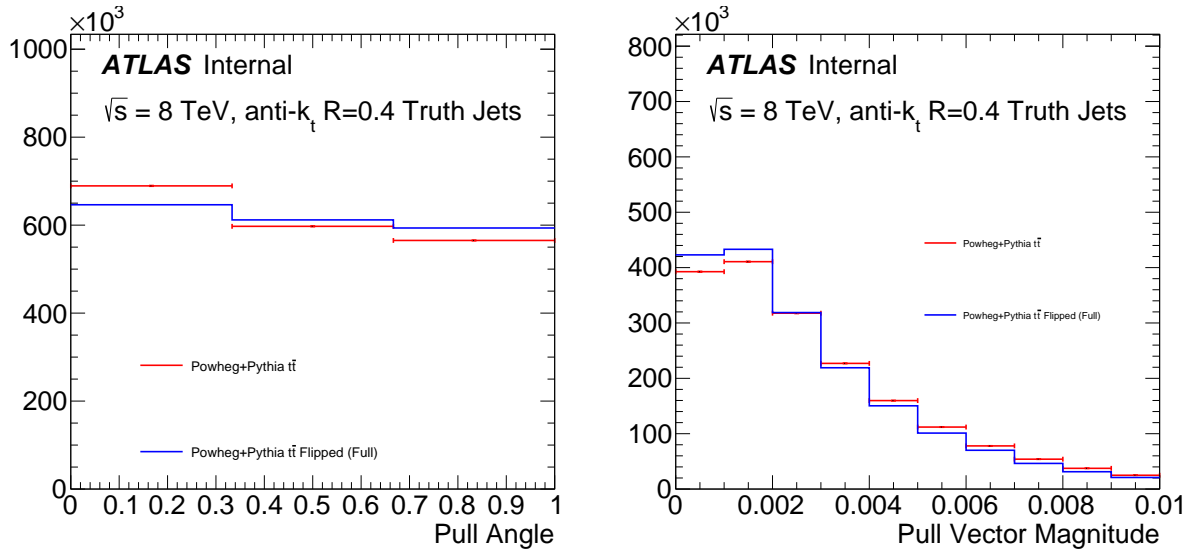


Figure 4: Pull vector angle and pull vector magnitude for the color flipped Powheg+Pythia sample.

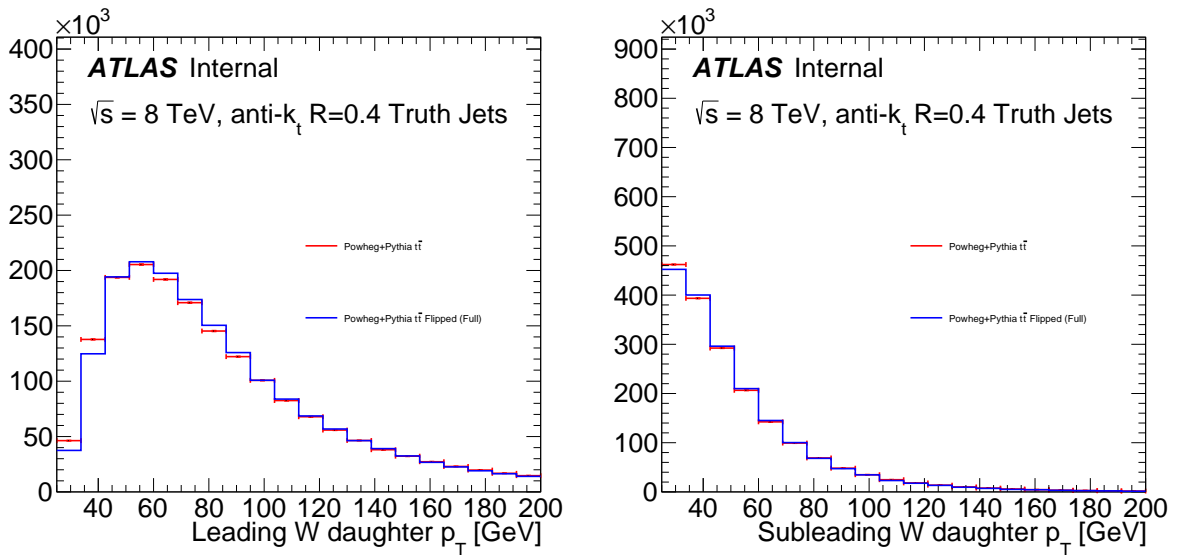


Figure 5: Transverse momentum spectra for the color flipped Powheg+Pythia sample.

Not reviewed, for internal circulation only

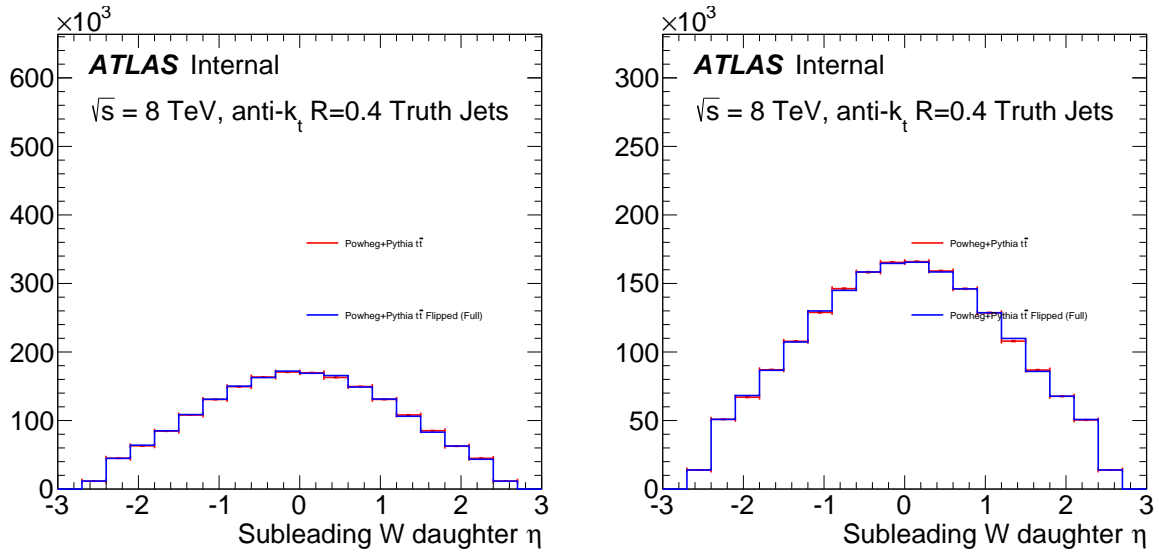
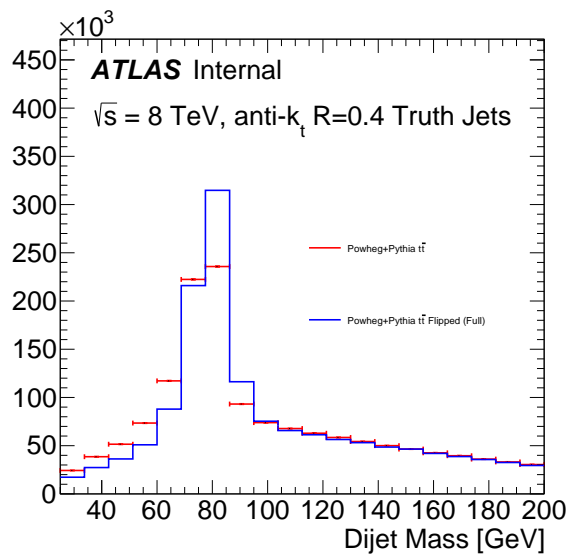


Figure 6: Pseudorapidity spectra for the color flipped Powheg+Pythia sample.

Figure 7: Invariant mass for the two leading non *b*-jets for the color flipped Powheg+Pythia sample.

## 263 4 Object and Variable Definitions

### 264 4.1 Variable Inputs: Jets, Tracks, and $b$ -tagging

265 The inputs to the jet pull vector are jets (and their constituent calorimeter clusters) and tracks. Jets are  
 266 further classified as having likely originated from a  $b$ -quark using a  $b$ -tagging algorithm. Electrons,  
 267 muons and missing transverse momentum are used in the  $t\bar{t}$  selection. The objects are constructed,  
 268 calibrated, and corrected as per TopRootCoreRelease-14-00-25.

#### 269 4.1.1 Clusters

270 Energy depositions in the calorimeters are organized into topological calorimeter clusters [22] and cali-  
 271 brated using the local cluster weighting (LCW) algorithm [23]. Clusters are treated as massless four-  
 272 vectors. While there is a spread in the  $z$ -location of the primary vertex, the default clusters are not  
 273 *origin-corrected* to point toward the primary vertex instead of the geometric center of the detector. Jets  
 274 (described next) are nominally formed from the non-origin corrected clusters. For substructure, the res-  
 275 olution of clusters and jets can be improved by origin correcting jets, as is done with the nominal jet  
 276 calibration prescription. Correcting the jets without correcting the clusters introduces a bias that can  
 277 impact any substructure variable that relies on a jet axis, like the pull angle. For more details about this  
 278 bias, see Appendix B.1. To compute substructure variables, we origin correct clusters<sup>6</sup> (the jet axis is  
 279 then constructed from the four vector sum of corrected clusters). The prescription for origin correcting  
 280 clusters is given below:

```
281 float radius = cl_centerMag->at(i)/cosh(cl_lc_eta->at(i));
282 float neweta = eta = asinh(sinh(cl_lc_eta)-vxp_z/radius);
283 cluster.SetPtEtaPhiM(cl_lc_pt->at(i)*cosh(cl_lc_eta->at(i))/cosh(neweta),
284     neweta,
285     cl_lc_phi->at(i),
286     0.0);
```

287 The quantity  $vxp_z$  is the  $z$ -location of the primary vertex. The reason for the value of  $neweta$  is given  
 288 by

$$z = R \sinh \eta \quad (2)$$

$$z \mapsto z' = z - z_{\text{corr}} \quad (3)$$

$$\eta \mapsto \eta' = \text{asinh}(z'/R) = \text{asinh}(z/R - z_{\text{corr}}/R) = \text{asinh}(\sinh(\eta) - z_{\text{corr}}/R) \quad (4)$$

289 where  $R$  is the radial location of the cluster (called `centermag` above). The  $p_T$  of the corrected cluster  
 290 results from a similar logic:

$$p_T = E/\cosh(\eta) \mapsto E/\cosh(\eta') = p_T \cosh(\eta)/\cosh(\eta') \quad (5)$$

---

<sup>6</sup>Thanks to Chris Young for suggesting the cluster origin correction and Dag Gillberg for the full form of the correction given in this section.

291 **4.1.2 Jets**

292 The nominal jets are clustered in  $y - \phi$  space using the anti- $k_t$   $R = 0.4$  [21] algorithm reconstructed from  
 293 the nominal clusters described in Sec. 4.1.1 and calibrated to account for the detector response as well  
 294 as to mitigate the contribution from pileup [24]. Jets are required to be central ( $|\eta| < 2.1$ ) so that their  
 295 charged particles are within the  $|\eta| < 2.5$  coverage of the ID. For jets with  $p_T < 50$  GeV, a jet vertex  
 296 fraction of at least 50% is required to reduce the impact of pileup. Jet calibration is performed using  
 297 the tool `ApplyJetCalibration-00-03-35` [50] that takes advantage of the newest global sequential  
 298 calibration algorithm. The jet  $\eta$  is also calibrated. An important component of this calibration is the jet  
 299 origin correction, which corrects the jet centers so that they point to the primary vertex instead of the  
 300 geometric center of the detector. The jet pull angle is very sensitive to the jet angular resolution, which  
 301 is significantly reduced by the origin correction. For consistency, the clusters must also be corrected, as  
 302 described in Sec. 4.1.1. For consistency, the four-vector sum of the corrected clusters is used for the jet  
 303 axis instead of the origin corrected jet axis. The difference between these two axes is in general very  
 304 small. Figures 8 and 9 show the jet axis resolution (difference between truth and reconstructed jet axes)  
 305 for various configurations. The takeaway message is that (1) the cluster origin correction improves the jet  
 306 angular resolution and (2) effectively reproduces the jet-based origin correction. Therefore, the nominal  
 307 measurement is made with **origin-corrected clusters** and **the four-vector sum of these clusters for the**  
 308 **jet axis**.

Not reviewed, for internal circulation only

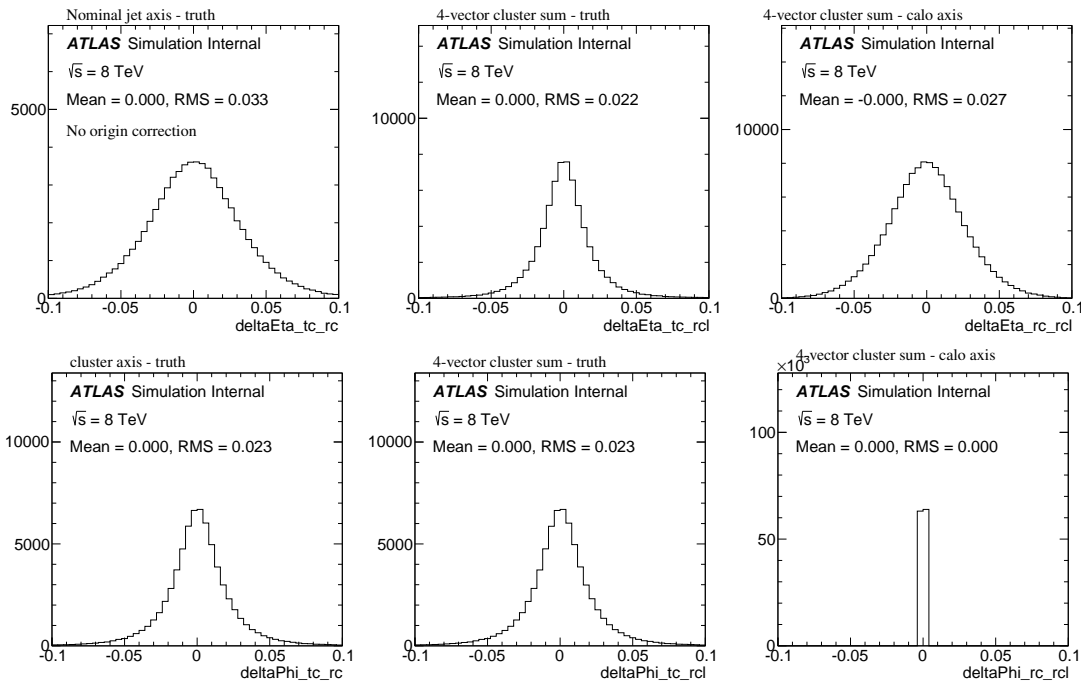


Figure 8: Various jet angular resolutions in  $t\bar{t}$  simulation without any jet origin corrections, but with cluster origin corrections. The top row of plots show the  $\eta$  resolution and the bottom row shows the  $\phi$  resolution. The first column is the resolution of the nominal jet axis, the middle column is the resolution of the axes formed from the four-vector sum of clusters and the last column is the difference between the two definitions of the reconstructed axes.

Not reviewed, for internal circulation only

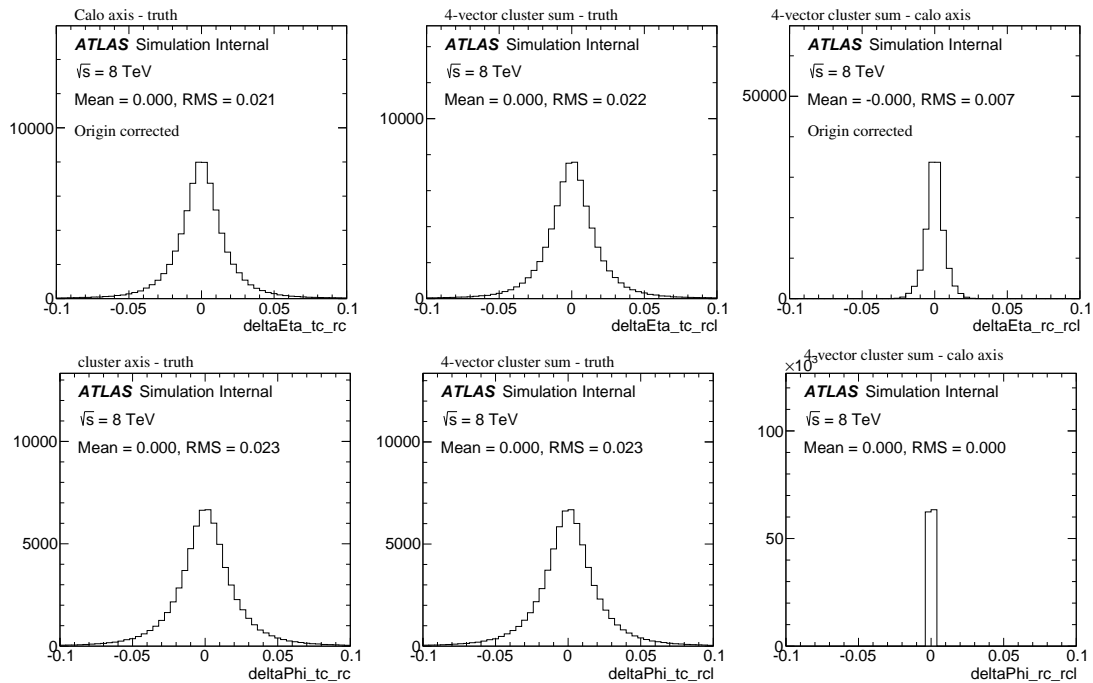


Figure 9: Various jet angular resolutions in  $t\bar{t}$  simulation with jet origin corrections in addition to cluster origin corrections. The top row of plots show the  $\eta$  resolution and the bottom row shows the  $\phi$  resolution. The first column is the resolution of the nominal jet axis, the middle column is the resolution of the axes formed from the four-vector sum of clusters and the last column is the difference between the two definitions of the reconstructed axes.

309 **Tracks** used to calculate the jet charge are required to have  $p_T \geq 500$  MeV,  $|\eta| < 2.5$ , and a  $\chi^2$  per degree  
 310 of freedom (resulting from the track fit) less than 5.0. Additional quality criteria are applied to  
 311 select tracks originating from the collision vertex: tracks must have

- 312 • at least one hit in the pixel detector,
- 313 • at least six hits in the silicon microstrip tracker,
- 314 • a longitudinal impact parameter with respect to the primary vertex (PV)  $|z_0^{\text{PV}}| \leq 2$  mm, and
- 315 • a transverse impact parameter with respect to the primary vertex  $|d_0^{\text{PV}}| \leq 2.5$  mm.

316 Tracks are associated to jets using ghost association [25]: an assignment of tracks to jets by adding  
 317 to the jet clustering process *ghost* versions of tracks that have the same direction but infinitesimally  
 318 low  $p_T$ . In the simulation, we will use truth jets, which are jets clustered with the same anti-  
 319  $k_t R = 0.4$  algorithm, but with all (detector-)stable MC particles as inputs. The ‘tracks’ of a truth  
 320 jet are simply the charged particles clustered into the jet.

321 ***b*-tagging** Jets are identified as *b*-quark jets using the multivariate discriminant ‘MV1’ [51] which includes impact parameter and secondary vertex information as inputs. The chosen MV1 working point corresponds to an average *b*-tagging efficiency of 70% for *b*-jets in simulated  $t\bar{t}$  events.

324 **Muons** The muon selection follows the ATLAS top group recommendations [52]. The standard quality  
 325 criteria include:

- 326 • ‘Tight’ combined muons (`author==12`). ‘Combined’ muons are made from tracks that have  
 327 been independently reconstructed in the Muon Spectrometer (MS) and the Inner Detector  
 328 (ID) with the STACO algorithm.
- 329 •  $p_T > 25$  GeV and  $|\eta| < 2.5$ .
- 330 • At least one hit in the b-layer if expected
- 331 • Number of pixel hits + number of crossed dead pixel sensors  $> 0$
- 332 • Number of SCT hits + number of crossed dead SCT sensors  $> 4$ .
- 333 • Number of pixel holes + number of SCT holes  $< 3$
- 334 •  $|z_0| < 2$  mm (with respect to the primary vertex)
- 335 • For  $n$  the sum of the hits in the TRT plus the number of TRT outliers,  
 336 – If  $0.1 < |\eta| < 1.9$  require  $n > 5$  and the number of outliers/ $n < 0.9$

337 Muon isolation is constructed using the *mini-isolation* variable [53, 54], which is defined as

$$I_{\text{mini}} = \sum_{\text{tracks}} p_T^{\text{track}},$$

338 for all tracks (excluding the muon track) with  $\Delta R(\mu, \text{track}) < 10$  GeV/ $p_T^\mu$ . Muons are required to  
 339 have  $I_{\text{mini}}/p_T^\mu < 0.05$ . This dynamic isolation requirement improves acceptance for highly boosted  
 340 top quark events in which the lepton and a nearby (*b*)-jet are very close. Following the standard  
 341 recommendation, muons are required to be isolated ( $\Delta R > 0.4$ ) from  $R = 0.4$  anti- $k_t$  jets. The same  
 342 criteria is applied to these jets as listed above.

343 **Electrons** The electron selection follows the ATLAS top group recommendations [55].

- 344 • ‘Tight++’ electrons and `author==1` or `author==3`.

- 345     • cluster  $E/\cosh\eta > 25$  GeV and  $|\eta| < 2.47$ , but not  $1.37 < |\eta| < 1.52$  (cluster  $\eta$ ).  
 346     •  $|z_0| < 2$  mm (with respect to the primary vertex).  
 347     • OQ&1446 quality criteria (avoid dead OTX)

348     The only non-standard criteria is the isolation, for which we require

- 349     1.  $\text{Etcone}20 > 6$  GeV  
 350     2.  $\text{Ptcone}30 > 6$  GeV

351     And as with muons, electrons are required to be isolated from jets. Jets are removed if  $\Delta R < 0.2$   
 352     to an electron and electrons with  $\Delta R < 0.4$  (after the electron jet overlap removal) are deemed  
 353     non-isolated and thus not considered.

354     **Missing Transverse Momentum** Missing transverse momentum is often denoted  $\vec{E}_T^{\text{miss}}$ . The  $\vec{E}_T^{\text{miss}}$  is  
 355     recalculated using calibrated objects as per the procedure in `TopRootCore`. The  $E_T^{\text{miss}}$  is the mag-  
 356     nitude of the two vector transverse missing momentum.

## 357     4.2 Event Selection

358     The reconstructed event selection uses an extended (one additional  $b$ -tag) version of the semi-leptonic  
 359     selections of `TopD3PDSelection-14-00-90`. In particular, selected events are triggered using isolated  
 360     single muons with offline  $p_T > 25$  GeV and  $|\eta| < 2.5$ . Basic quality criteria are imposed, including the  
 361     existence of at least one primary vertex associated with five or more tracks with transverse momentum  
 362      $p_T > 0.4$  GeV. Candidate reconstructed  $t\bar{t}$  events are chosen by further requiring missing transverse  
 363     momentum,  $E_T^{\text{miss}} > 20$  GeV, where the  $E_T^{\text{miss}}$  takes into account reconstructed physics objects such as  
 364     leptons and jets as well as energy not associated to a particular final state object [56]. In addition, the  
 365     sum of the missing transverse momentum and the transverse mass<sup>7</sup> of the  $W$  is required to be greater than  
 366     60 GeV. Events must also have at least four jets with  $|\eta| < 2.5$  ( $|\eta| < 2.1$  for all track pull angle studies)  
 367     and  $p_T > 25$  GeV. Exactly two of these jets must be identified as  $b$ -quark jets using the multivariate  
 368     discriminant ‘MV1’ [51] which includes impact parameter and secondary vertex information as inputs.  
 369     The chosen MV1 working point corresponds to an average  $b$ -tagging efficiency of 70% for  $b$ -jets in  
 370     simulated  $t\bar{t}$  events. This procedure selects a sample that is expected to contain approximately 90%  $t\bar{t}$   
 371     production (see Sec. 6). See Table 4 for the cutflow for both the data in the muon stream as well as for  $t\bar{t}$   
 372     MC produced with Powheg full detector simulation.

373     There are several strategies for identifying the hadronic decay products of the  $W$  bosons. Two strate-  
 374     gies are explored in this note:

- 375     1. Identify the leading two non  $b$ -tagged jets as the  $W$  daughters. A further cut can be placed on their  
 376       invariant mass.  
 377     2. Of the non  $b$ -tagged jets above  $p_T > 25$  GeV, pick the pair whose invariant mass is closest to 80  
 378       GeV. A further cut can be placed on how close this pair is to 80 GeV.

379     Each option above has its relative merits. For instance, (2) has a slightly higher purity in the following  
 380     sense. Since  $W$  bosons are color singlets, it is possible in the (`Pythia`) MC event record to unambiguously  
 381     assign a particle as being an descendant of a  $W$  boson or not. Thus, one can assign to any (detector) stable  
 382     hadron the fraction of the  $W$  boson energy it carries. Using a standalone version of `Pythia` 6 (for full

---

<sup>7</sup>The transverse mass,  $m_T$ , is defined as  $m_T^2 = 2p_T^{\text{lep}} E_T^{\text{miss}} (1 - \cos(\Delta\phi))$ , where  $\Delta\phi$  is the azimuthal angle between the lepton and the missing transverse momentum direction. The quantity  $p_T^{\text{lep}}$  is the transverse momentum of the charged lepton.

Not reviewed, for internal circulation only

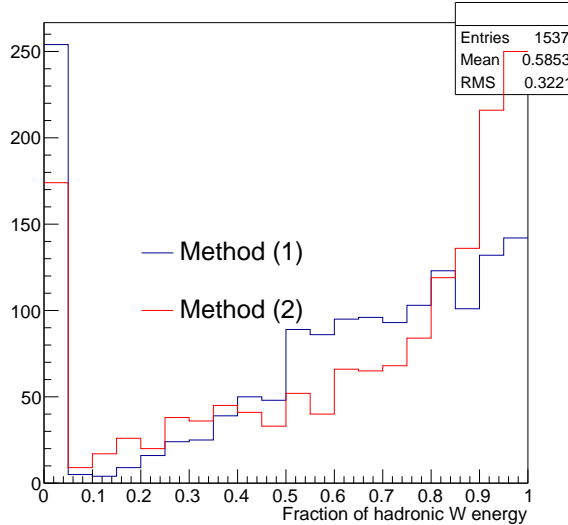


Figure 10: Fraction of the  $W$  boson energy carried by the sum of the two selected  $W$  daughter jets.

383 and unbroken access to the truth record), it is verified that the sum of all fractions equals one. Figure 10  
 384 shows the weight for the two jets chosen via methods (1) and (2). If we define purity as the fraction  
 385 of the  $W$  boson energy carried by the two jets, then method (2) has a slightly higher purity. On the  
 386 other hand, method (1) may be preferred when testing exotic color models, since a mass-based selection  
 387 will be affected by the radiation pattern and could be different between models, whereas the leading jet  
 388 transverse momenta should be the same (see Sec. 3.4.1). Unless otherwise mentioned, method (1) is used  
 389 in all subsequent studies.

390 The two  $b$ -tagged jets are labeled  $B_1, B_2$  and the  $W$  daughter jets are labeled  $J_1, J_2$ , as in Fig. 11 (for  
 391 option (2) in the  $W$  daughter labeling).

392 A truth object based selection is constructed analogously to the reconstructed event selection. The  
 393 input objects are those described in the next section on truth studies, but all other selections are the same  
 394 including jet  $p_T$  thresholds, muon requirements, isolation, etc. Figure 24 shows the distribution of the  
 395  $\Delta R$  between the selected reconstructed jets and truth jets using MC@NLO  $t\bar{t}$ . The spikes in the first bin  
 396 correspond to the cases where the truth selection picks the same jet and correspond to 81% of cases for  
 397 the leading jet and 70% of cases for the sub-leading jet. Some fraction of the time, the  $p_T$  ordering is  
 398 flipped between the truth and reco selections (as determined by  $\Delta R$ ). The left plot of Fig. 13 shows the  
 399 minimum  $\Delta R$  between the reco  $J_1$  and either  $J_1$  or  $J_2$  from the truth selection. The purity for the leading  
 400 reco jet is increased by about 10% with respect to Fig. 12. The right plot of Fig. 13 shows the maximum  
 401 of this same quantity for the reco  $J_1$  and  $J_2$ ; while in some cases the leading reco jet is the subleading  
 402 truth jet, it is often not the case that the subleading reco jet is the leading truth jet (and so the 72% is not  
 403 a large improvement over the 70% in the right plot of Fig. 12).

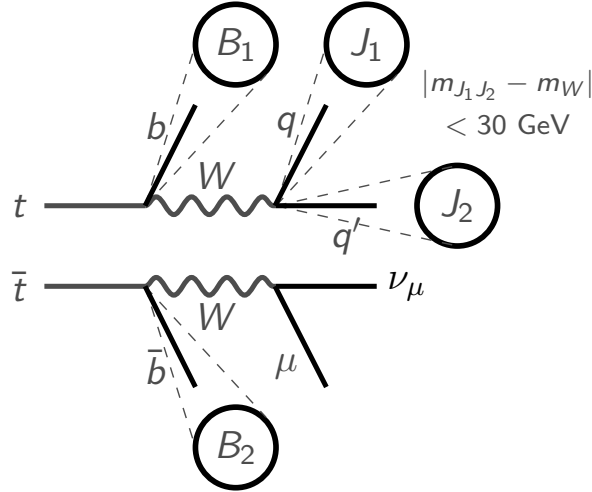


Figure 11: Schematic representation of the object selection. At least four jets are required: two  $b$ -tagged jets  $B_1, B_2$  and of the remaining non  $b$ -tagged jets, two are required to have an invariant dijet mass close to  $m_W$ , and are labelled  $J_1, J_2$ . The muon is used to trigger and a cut on the missing energy from the neutrino is used to purify the sample in  $t\bar{t}$  events.

Not reviewed, for internal circulation only

Selection	Data	Efficiency	Powheg	Fullsim	Efficiency
Skim+Slim	2.33e8	100%	1.50e7		100%
GRL	2.24e8	96%	1.50e7		100%
Detector Problems	2.23e8	100%	1.50e7		100%
Vertex	2.23e8	100%	1.50e7		100%
Muon Trigger	2.23e8	100%	3.53e6		24%
$\geq 1$ muon	1.08e8	48%	2.74e6		78%
$= 1$ muon	1.01e8	95%	2.62e6		96%
No electrons	1.01e8	100%	2.60e6		99%
No bad jets	9.85e7	98%	2.54e6		98%
$\geq 2$ jets	5.26e6	5%	2.36e6		93%
$\geq 3$ jets	1.39e6	26%	1.87e6		79%
$\geq 4$ jets	4.28e5	31%	1.09e6		58%
MET	4.09e5	96%	1.05e6		96%
MET+MT	3.75e5	92%	9.97e5		95%
$\geq 1$ $b$ -jet	1.95e5	52%	8.60e5		86%
$\geq 2$ $b$ -jets	82766	42%	4.18e5		49%
$\geq 2$ non $b$ -jets	78896	95%	3.98e5		95%

Table 4: Cutflow for the muon channel in data. Efficiencies are computed with respect to the previous cut. MC event counts are unweighted. [NUMBERS ARE OUTDATED]

Not reviewed, for internal circulation only

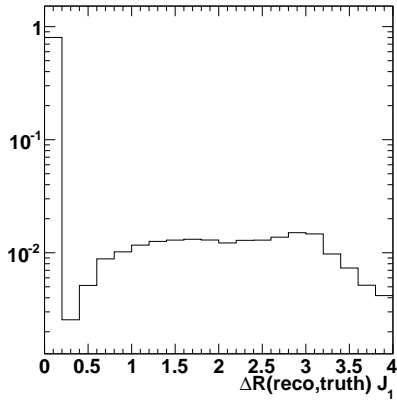
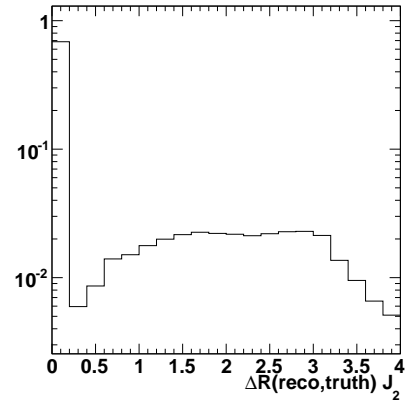
**Fraction with  $< 0.4$  is 0.81****Fraction with  $< 0.4$  is 0.70**

Figure 12:  $\Delta R$  between the selected  $W$  daughter jets (using method (1)) and the truth jets selected by the same procedure.

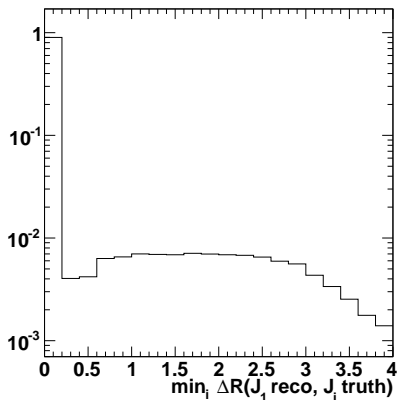
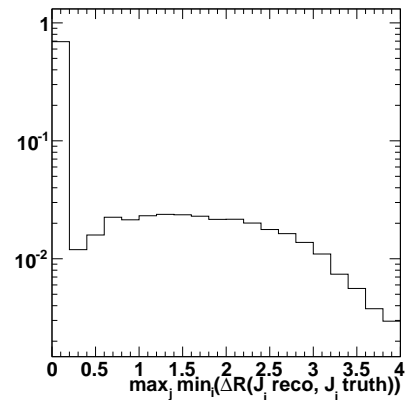
**Fraction with  $< 0.4$  is 0.91****Fraction with  $< 0.4$  is 0.72**

Figure 13: The left plot shows the smaller of  $\Delta R(J_1, J'_1)$  and  $\Delta R(J_1, J'_2)$  where the prime denotes a truth jet. The right plot shows the maximum over this quantity for the two  $W$  daughter jets.

## 404 5 Truth Studies

405 The analysis framework has two parallel structures, a D3PD-based analysis (using the `ProofAna` frame-  
 406 work [57]) and a Rivet based analysis. The former is used for all studies involving reconstructed objects  
 407 while the latter is useful for making comparisons on truth level distributions and can also be made public  
 408 with the results.

### 409 5.1 Rivet implementation

410 Rivet [58] is a framework for Robust Independent Validation of Experiment and Theory. Analysis code  
 411 written with Rivet runs directly on the generic HepMC event record (and therefore also ATLAS EVNT  
 412 files), which is output by all modern shower Monte Carlo programs. Having an analysis written in Rivet  
 413 can make it very easy to compare unfolded data to theory predictions from any MC generator, since  
 414 EVNT-level events can be generated very quickly.

415 It is important that the Rivet analysis provides results consistent with those obtained using the stan-  
 416 dard D3PD-bases analysis code, and also that it is written in such a way that only information about the  
 417 stable final-state particles is used. Requiring that the “parent” of a lepton be a W-boson, for example, is  
 418 not only an unphysical property to check but also cannot be implemented in events from all MC gener-  
 419 ators. The SHERPA [59] event generator does not write information about intermediate particles which  
 420 are in principle not experimentally detectable to its event record, and therefore checks such as the one  
 421 mentioned should be avoided.

422 The Standard Model and Top working groups have produced a document [60] which contains recom-  
 423 mendations for selecting particle-level objects in a generator-independent way. These recommendations  
 424 are implemented in both the Rivet and D3PD-based analysis codes. The latter through a slightly modi-  
 425 fied version of the code in the `TopFiducial` package. The definitions used to construct and select the  
 426 relevant particle-level objects are as follows:

427 **Electrons** Stable final-state particles with  $|PdgId|=11$ , with no physical parent<sup>8</sup> that is a hadron or tau.

428 **Muons** Stable final-state particles with  $|PdgId|=13$ , with no physical parent that is a hadron or tau.

429 **Neutrinos** Stable final-state particles with  $|PdgId|=12, 14, 16$  with no physical parent that is a hadron.

430 **Photons used for lepton dressing** Stable final-state particles with  $PdgId=22$ , with no physical parent  
 431 that is a hadron or tau.

432 **Inputs to jet clustering** Stable final-state particles which do not satisfy any of the definitions above.

433 Particle-level missing transverse energy is calculated by taking the vector-sum of all neutrinos which  
 434 satisfy the above requirement. Electrons and muons are dressed by combining with them any photons  
 435 which satisfy  $\Delta R(\text{photon}, \text{lepton}) < 0.1$ . In [60] it is suggested to “investigate further the matching using  
 436 a cluster algorithm, like e.g. anti-kt ( $R = 0.1$ ) expected to be more appropriate in complex topologies”.  
 437 The method of lepton dressing was studied using Rivet. Electrons, muons and photons were selected  
 438 according to the definitions above and used as input to the anti- $k_t$  jet clustering algorithm with  $R=0.1$ .  
 439 The  $p_T$  of each anti- $k_t$ -dressed leptons was then compared to the corresponding lepton dressed using the  
 440 standard  $\Delta R$  dressing technique. As shown in Figure 14 for the vast majority of events the difference  
 441 between the two dressing techniques is exactly zero – the same photons are selected to dress the leptons  
 442 in each case. In the tiny number of cases where the two methods of dressing are not identical, it is the  
 443 leptons dressed using the anti- $k_t$  method which are very slightly harder than the  $\Delta R$ -dressed ones: the tail  
 444 to the left of the distributions can be seen to be very slightly higher than the tail to the right.

---

<sup>8</sup>The parent of a given particle is designated physical if it has a HepMC status code==2.

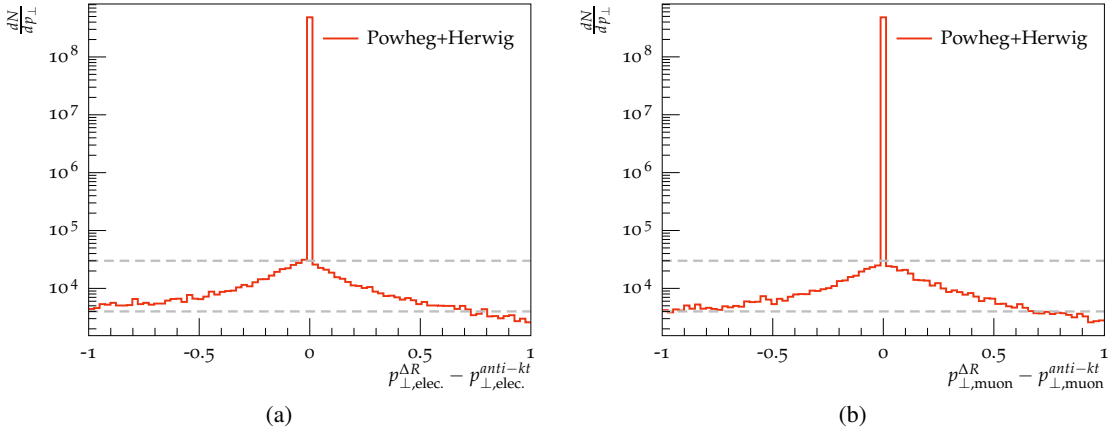


Figure 14: The difference in  $p_T$  between electrons (a) and muons (b) dressed using an anti- $k_t$  technique and those dressed using a standard  $\Delta R$  dressing method. The axis are given in units of GeV.

445 Particle-level b-jets are identified by ghost-matching B-hadrons to jets. Specifically, B-hadrons with  
 446  $p_T > 5$  GeV are selected from the event record <sup>9</sup>, and scaled such that their  $p_T$  and energy is negligible.  
 447 These scaled B-hadrons are then added to the list of particles used in the jet clustering. They point in  
 448 the same direction as the original B-hadrons, but they will not affect the clustering in any way. Once the  
 449 jets have been built, any which contain one or more of the ghost B-hadrons are labelled as particle-level  
 450 b-jets.

451 Figure 15 shows comparisons of the pull angle distributions produced by the Rivet and D3PD-based  
 452 analysis codes. The two sets of distributions are consistent with each other.

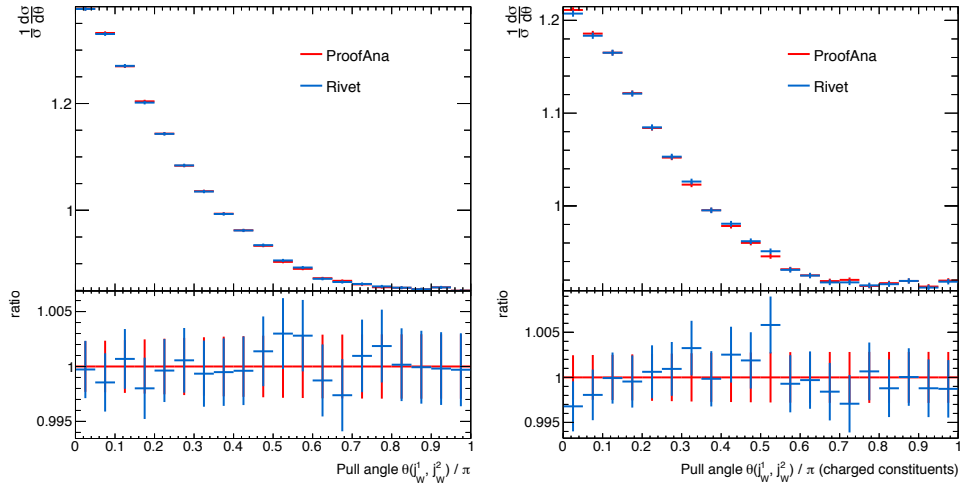


Figure 15: Comparison of the pull angle distribution between the two W daughter jets obtained using the Rivet and D3PD-based implementations of the analysis.

<sup>9</sup>Note: B-hadrons are not stable, final-state particles. However a check can be made on their HepMC status code (==2) to ensure that they have been considered by the generator to be “physical, but decayed”

## 453 5.2 Comparisons of Truth Level Distributions

454 This section contains some additional comparisons of the nominal and color inverted  $t\bar{t}$  MC samples.  
 455 From Sec. 3.4.1, we know that the difference in the radiation pattern leads to a different invariant mass  
 456 distribution for the leading non  $b$ -tagged jets. In the context of the color flow measurement in  $t\bar{t}$ , one may  
 457 argue that the invariant mass then could be used to distinguish the two models. This is not the purpose  
 458 of the measurement (for a new resonance, we will not know its mass and so certainly the mass cannot  
 459 be used), but we should check the impact on the present analysis. Figure 16 shows the invariant mass  
 460 before and after re-weighting events to have the same mass spectrum. The corresponding pull angle  
 461 distributions are in Fig. 17, where one can see that there is a truly negligible impact on the invariant mass  
 462 and so it is inconsequential if the mass is re-weighted. Similar behavior is seen for the charged particle  
 463 pull angle in Fig. 18.

Not reviewed, for internal circulation only

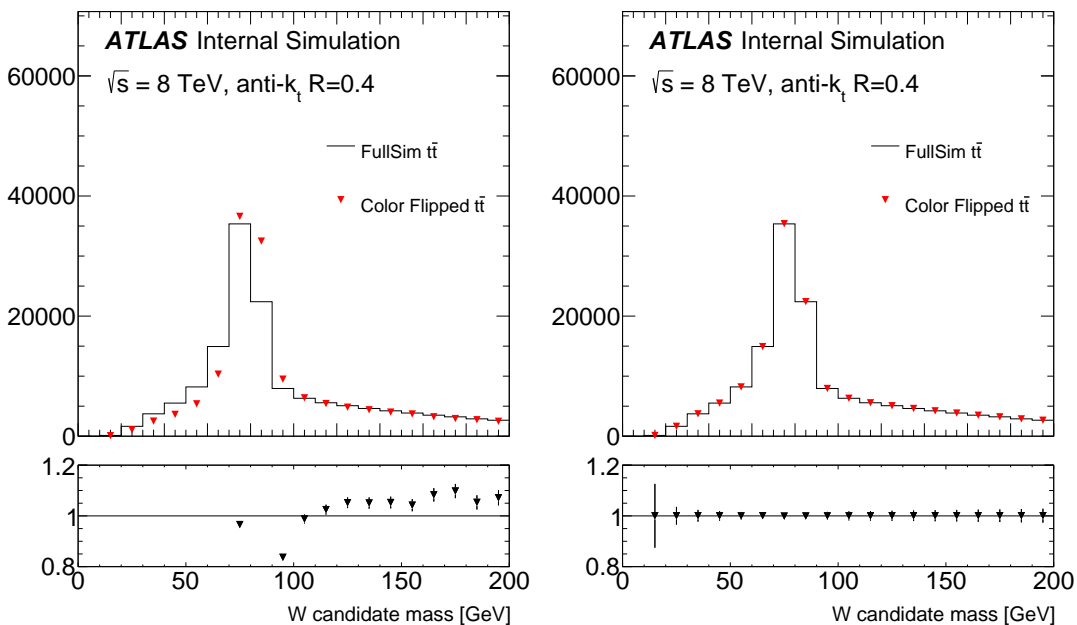


Figure 16: The invariant mass of the leading non  $b$ -tagged jets with no re-weighting applied (left) and a weighting to the invariant mass spectrum (right).

464 Another quick study is to check the impact on the  $W$  daughter selection choice discussed in Sec. 4.2.  
 465 Figure 19 shows that the gain in discrimination power is marginal, due mostly to the fact that most of the  
 466 events have 4 jets and so the two selection methods pick the same jets in most cases.

Not reviewed, for internal circulation only

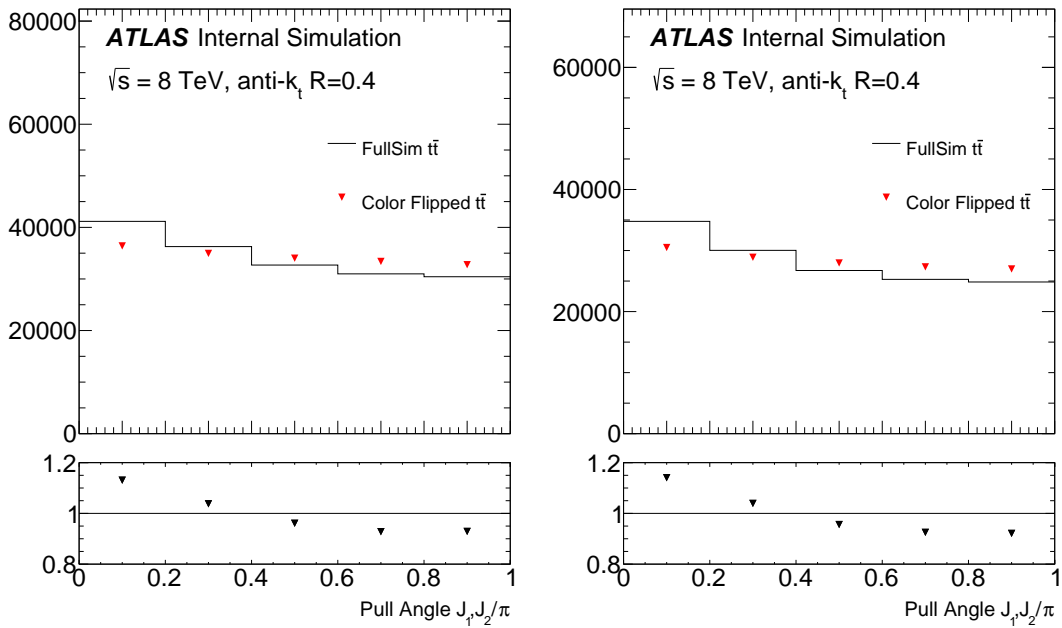


Figure 17: The pull angle with no re-weighting applied (left) and a weighting to the invariant mass spectrum (right).

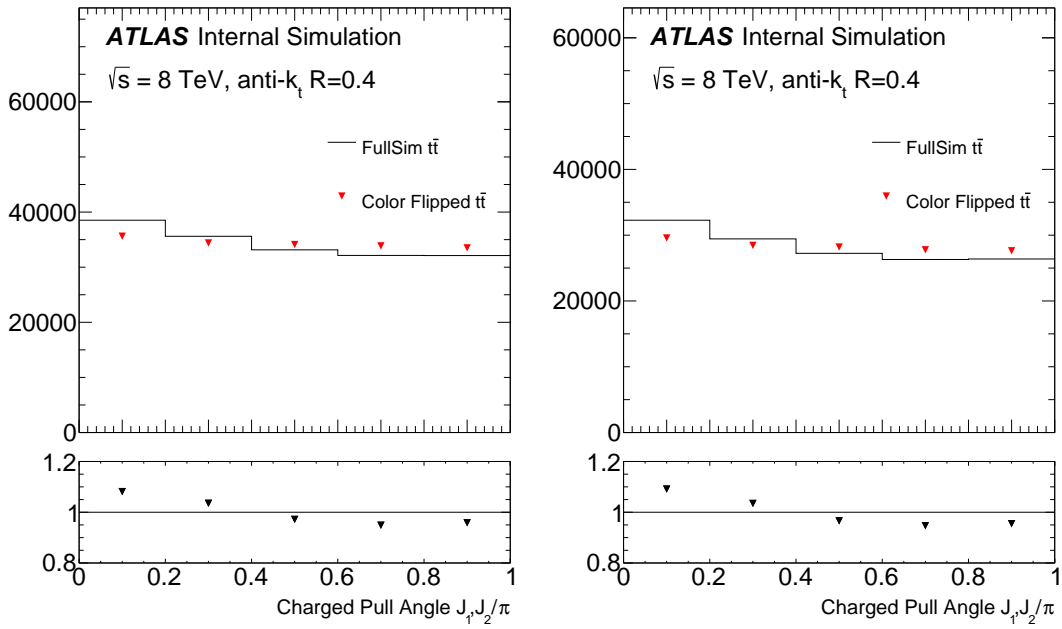


Figure 18: The charged particle pull angle with no re-weighting applied (left) and a weighting to the invariant mass spectrum (right).

Not reviewed, for internal circulation only

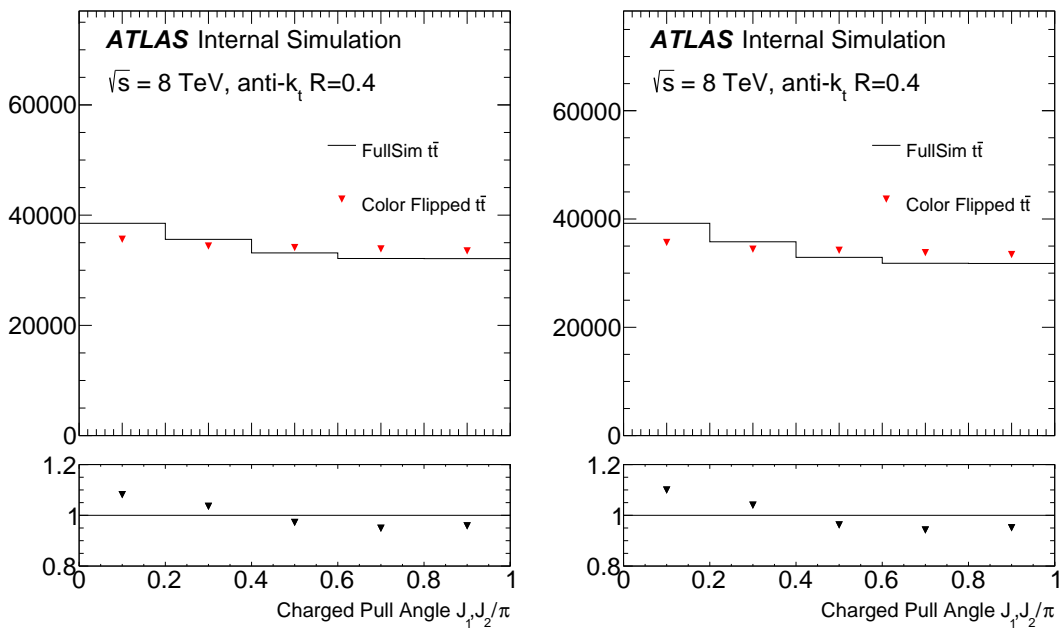


Figure 19: The charged particle pull angle for nominal  $W$  selection (left) and for the non  $b$ -tagged jets with invariant mass closest to  $m_W$  (right).

Not reviewed, for internal circulation only

## 467 6 Comparisons

### 468 6.1 Data/MC

469 This section contains various distributions comparing the data with MC including the detector simulation.  
 470 In all figures, the MC is normalized by cross section to  $20.3 \text{ fb}^{-1}$  - see Table 5 for the expected  
 471 background composition. The fake background is estimated from data with the matrix method, as de-  
 472 scribed in Ref. [61]. Two data samples—tight and loose— are defined based on their observed muon  
 473 isolation, and measured efficiency values for these selections are used to estimate the number of events  
 474 with fake leptons using the formula:

$$N_{\text{fake}}^{\text{tight}} = \frac{\epsilon^{\text{fake}}}{\epsilon^{\text{real}} - \epsilon^{\text{fake}}} \cdot (\epsilon_{\text{real}} N^{\text{loose}} - N^{\text{tight}}). \quad (6)$$

475 The  $W+\text{jets}$  are normalized using the charge asymmetry method<sup>10</sup>, in which the (heavy) flavor fractions  
 476 are fit in each charge bin and the overall normalization is given by

$$N_{W^+} + N_{W^-} = \frac{N_{W^+}^{\text{MC}} + N_{W^-}^{\text{MC}}}{N_{W^+}^{\text{MC}} - N_{W^-}^{\text{MC}}} (N_{W^+}^{\text{Data}} - N_{W^-}^{\text{Data}}). \quad (7)$$

477 The normalizations are converted to scale factors and extrapolated to the four jet inclusive bin. The scale  
 478 factors are given by  $1.3 \pm 0.03$  for the bb/cc component,  $0.74 \pm 0.04$  for the single c component and  
 479  $0.96 \pm 0.02$  for the light component. With the current selection, the predicted contribution from  $t\bar{t}$  is  
 480 89%, from single top is 2% and from  $W+\text{jets}$  is 5%. Figures 20, 22, and 26 show the basic kinematic  
 481 selection of the leading and subleading jets. The uncertainty band on the Standard Model is from the  
 482 contribution of the jet energy scale and resolution uncertainties as well as a 6% uncertainty on the top pair  
 483 production cross section. In particular, Fig. 20 shows the  $p_T$  distribution for the leading and subleading  
 484  $W$  daughter candidate jets. These are the leading and sub-leading non b-tagged jets. Since the pull  
 485 vector angle  $\theta_P(J_1, J_2) \neq \theta_P(J_2, J_1)$  in general as the former uses the substructure of  $J_1$  and the latter  
 486 uses the substructure of  $J_2$ , both are used in the measurement of the pull angle distribution (in fact,  
 487 this information is largely uncorrelated [26]). The  $\eta$  of the two  $W$  daughter candidate jets are shown in  
 488 Fig. 22, the  $\Delta R$  in Fig. 24 and the dijet mass and  $p_T$  in Fig. 26.

Process	Preselection	% of SM	$ v_p  > 0.004$	%	$ v_p^{\text{charged}}  > 0.004$	%
Data	78896	N/A	29651	N/A	25944	N/A
Standard Model	$82888 \pm 160$		$32028 \pm 106$	100%	$28649 \pm 97$	100%
$t\bar{t}$	$73961 \pm 117$	89%	$28411 \pm 73$	89%	$25201 \pm 68$	88%
$Wt$ -channel single top	$621.0 \pm 16.6$	0.7%	$235.4 \pm 10$	0.7%	$222.5 \pm 10$	0.8%
$s-$ and $t$ -channel single top	$1186.3 \pm 22.6$	1.4%	$449.6 \pm 14$	1.4%	$395.4 \pm 13$	1.4%
$W+\text{jets}$	$4386.0 \pm 63$	5%	$1570.5 \pm 36$	5%	$1561.9 \pm 38$	5%
$Z+\text{jets}$	$653.7 \pm 10.9$	0.8%	$251.7 \pm 7$	0.8%	$251.8 \pm 6.5$	0.8%
Dibosons	$45.1 \pm 2.8$	< 0.1%	$19.2 \pm 2$	< 0.1%	$19.0 \pm 2$	< 0.1%
Multijets	$2523.6 \pm 89.0$	3%	$1091.0 \pm 65$	3%	$997.2 \pm 55$	3%

Table 5: Event yield and expected background composition (normalized by cross section to  $(20.3 \text{ fb}^{-1})$  for the MC). Uncertainties only reflect MC statistics (except for multijets). [NUMBERS OUTDATED]

<sup>10</sup>See [https://twiki.cern.ch/twiki/bin/view/AtlasProtected/WplusJetsBackgroundsforTopAnalyses#Latest\\_W\\_jet\\_SF\\_for\\_8\\_TeV\\_full\\_d](https://twiki.cern.ch/twiki/bin/view/AtlasProtected/WplusJetsBackgroundsforTopAnalyses#Latest_W_jet_SF_for_8_TeV_full_d).

489 The remaining figures show aspects of the jet pull vector. Figures 27 and 28 show the pull angle  
 490 between  $J_1$  and  $J_2$  (as well as vice versa) for the calorimeter pull and the track pull, respectively. The  
 491 corresponding pull vector magnitudes are shown in Fig. 33 and 36.

Not reviewed, for internal circulation only

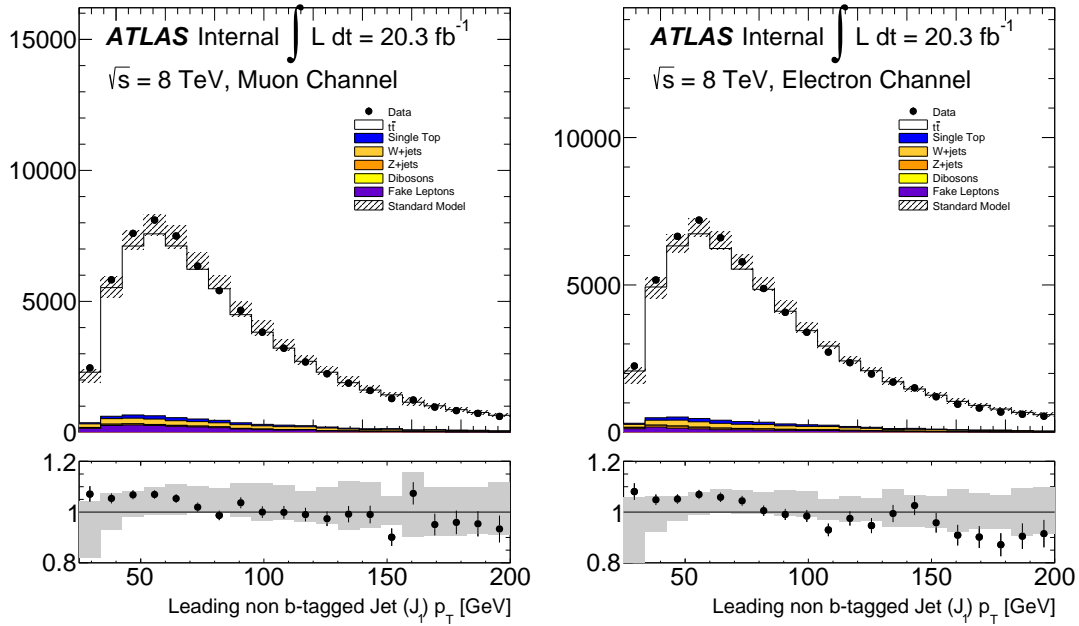


Figure 20: The leading  $W$  daughter jet  $p_T$ .

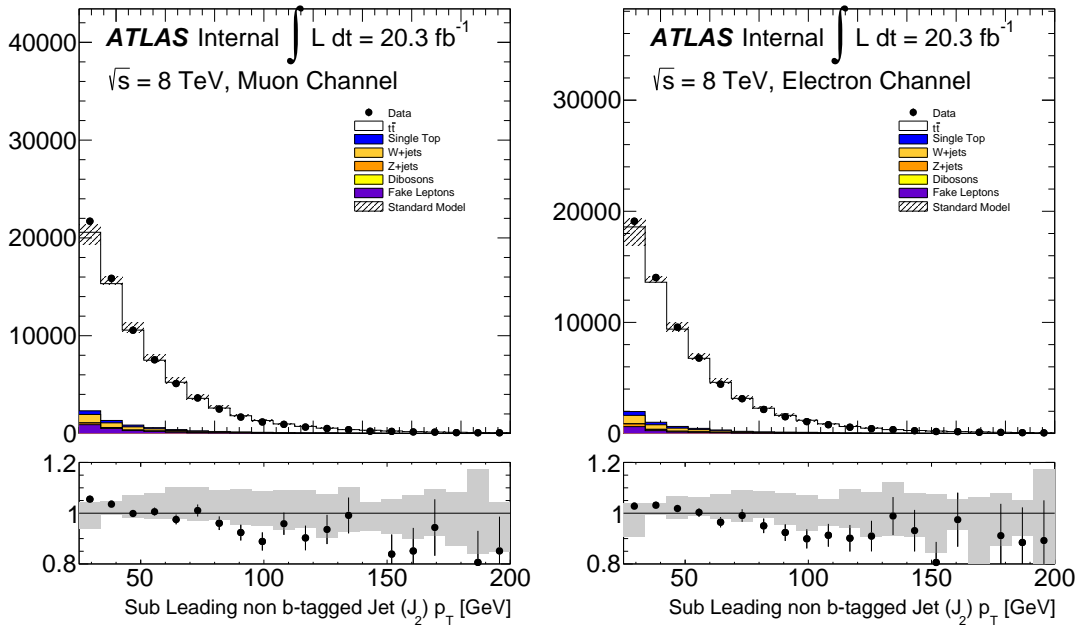
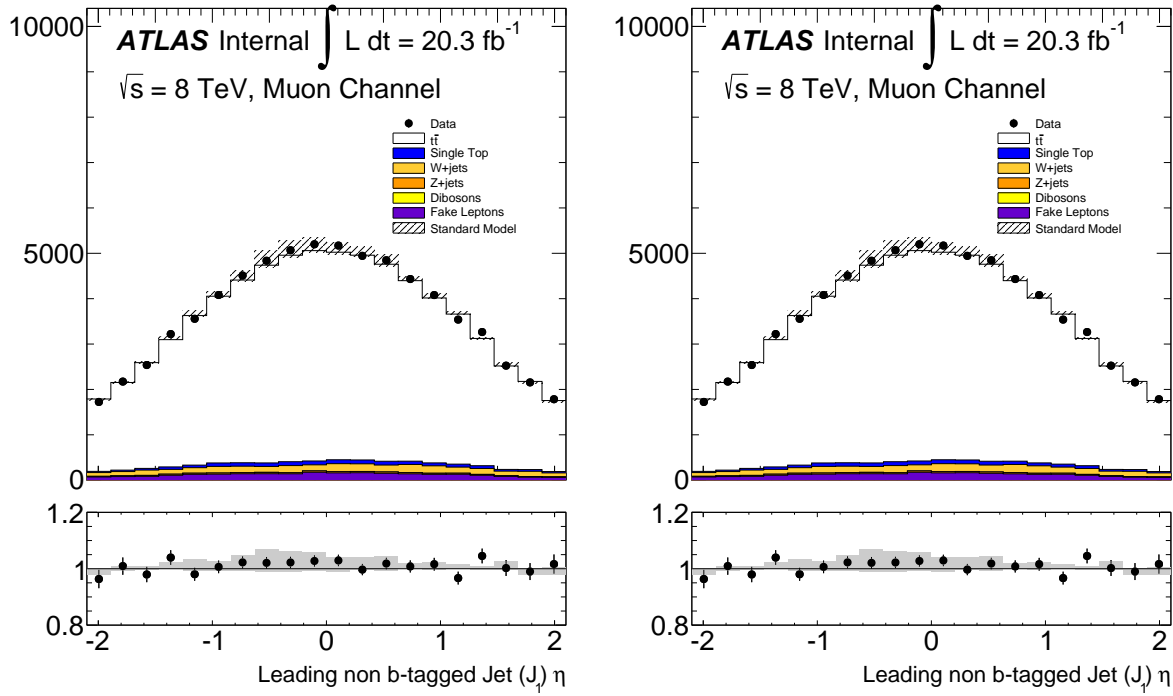
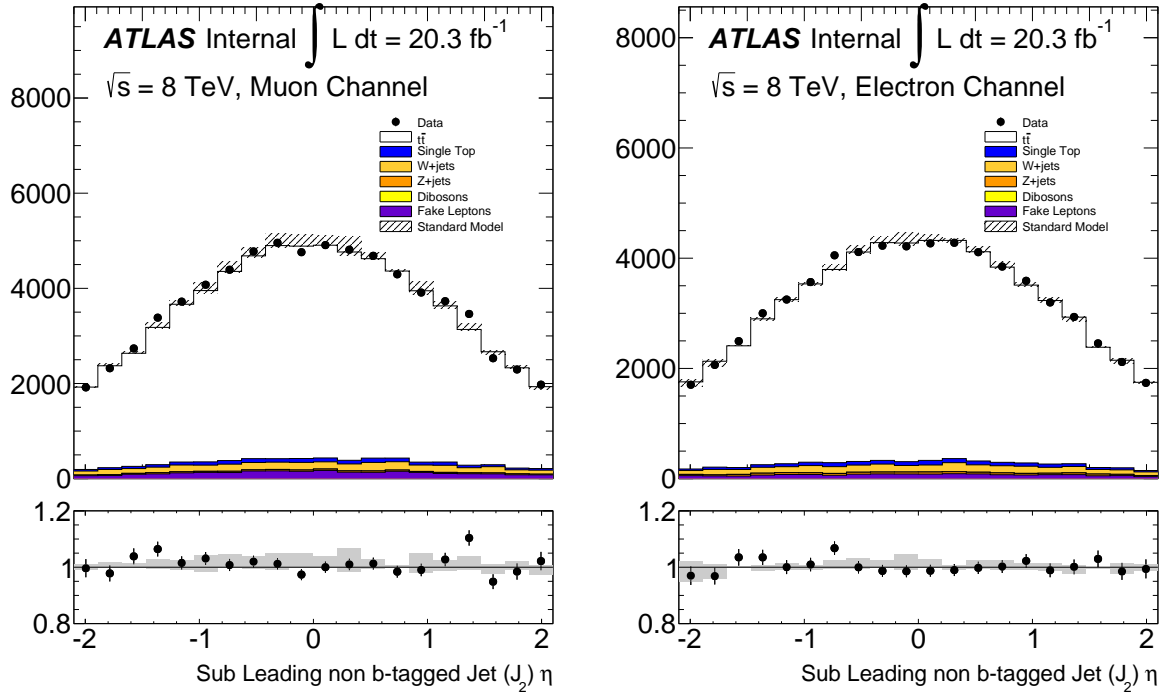
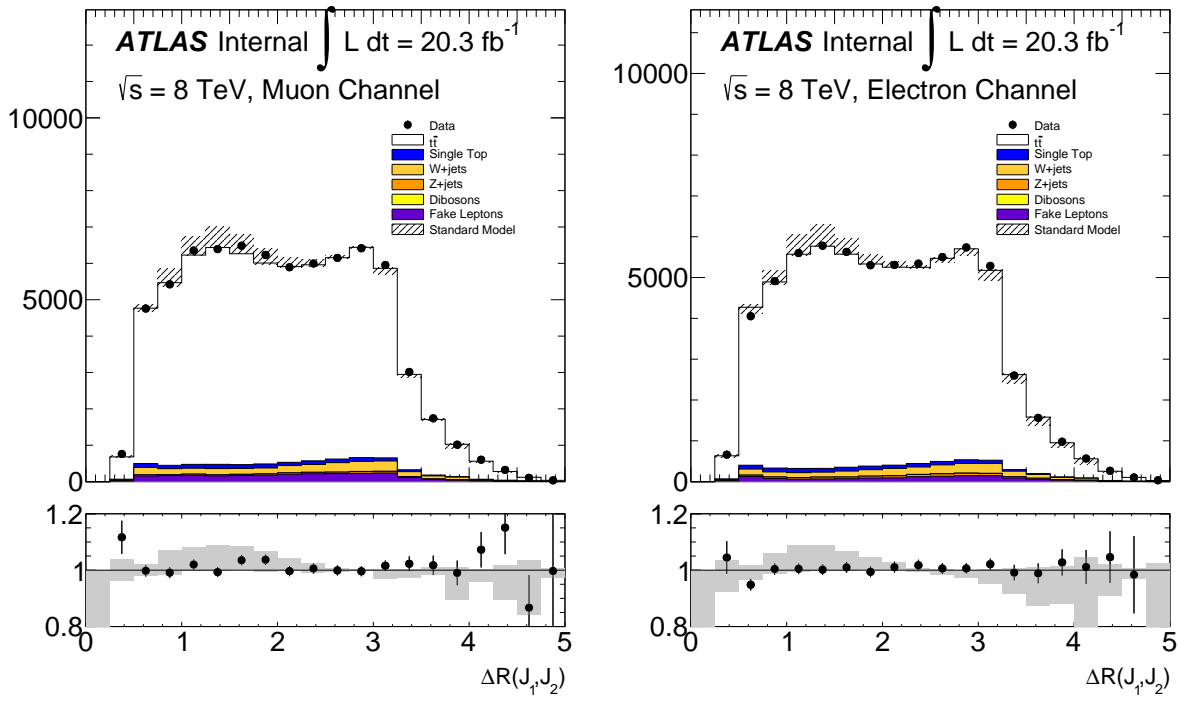
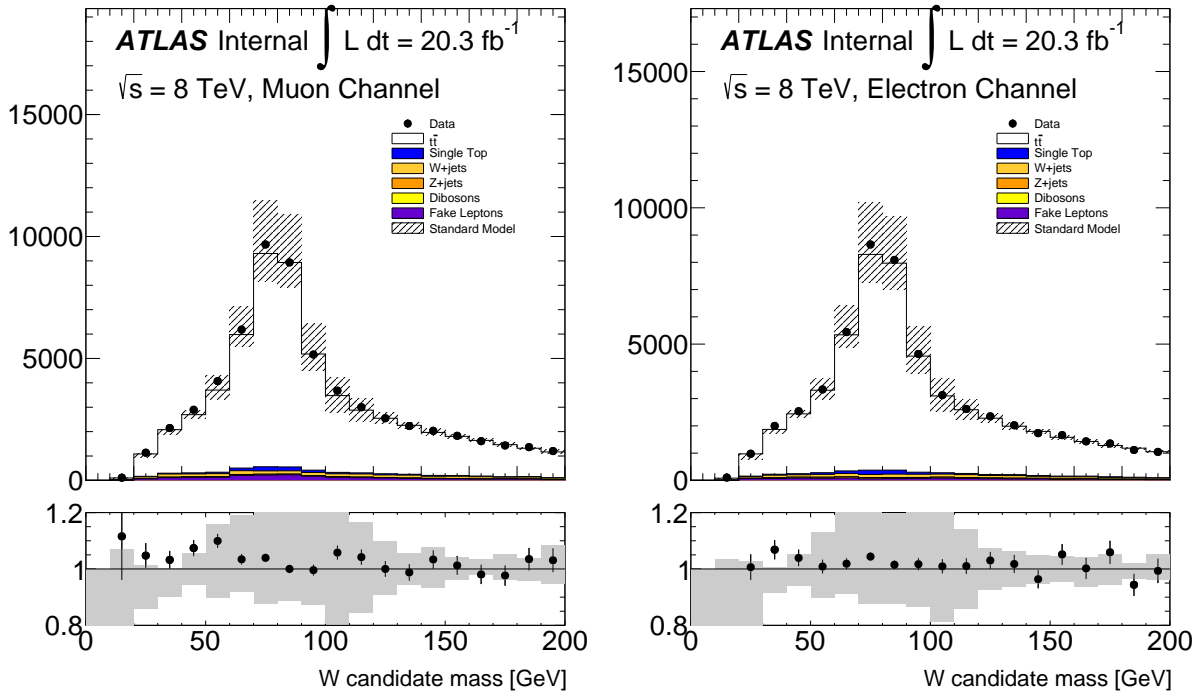


Figure 21: The sub-leading  $W$  daughter jet  $p_T$ .

Not reviewed, for internal circulation only

Figure 22: The leading  $W$  daughter jet  $\eta$ .Figure 23: The sub-leading  $W$  daughter jet  $\eta$ .

Not reviewed, for internal circulation only

Figure 24: The  $\Delta R$  between  $J_1$  and  $J_2$ .Figure 25: The dijet invariant mass of the combination of the leading and subleading  $W$  daughter candidate 4-vectors.

Not reviewed, for internal circulation only

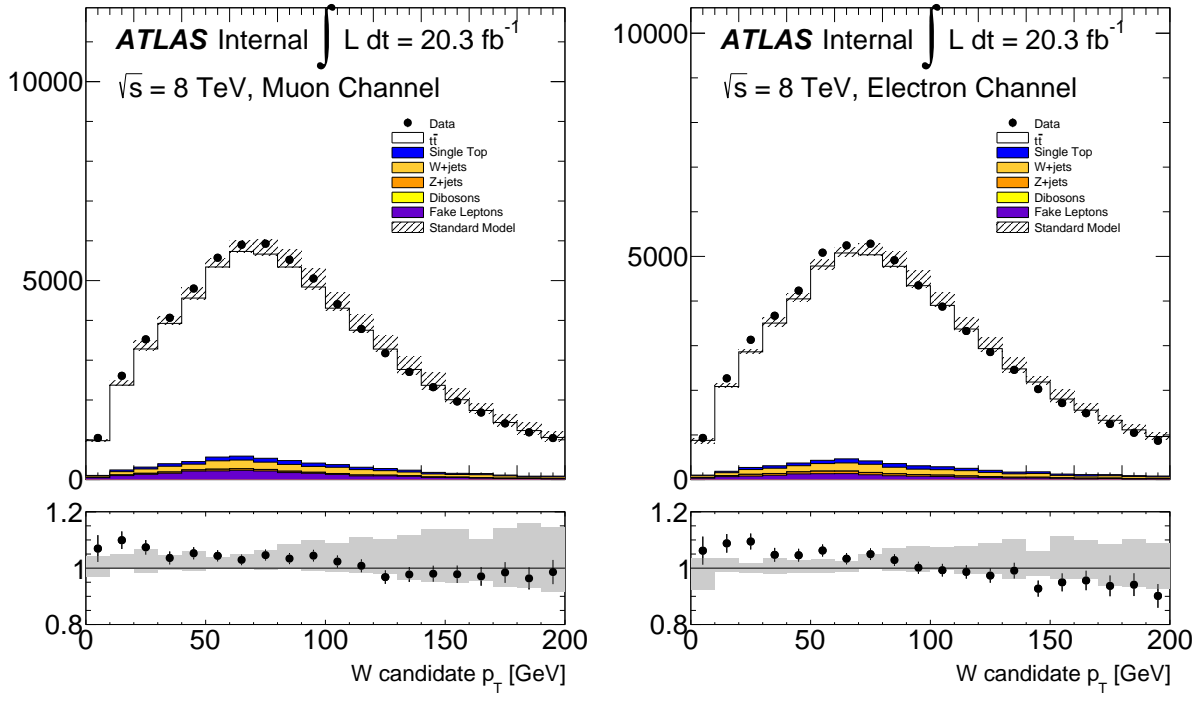


Figure 26: The  $p_T$  (right) of the combination of the leading and subleading  $W$  daughter candidate 4-vectors.

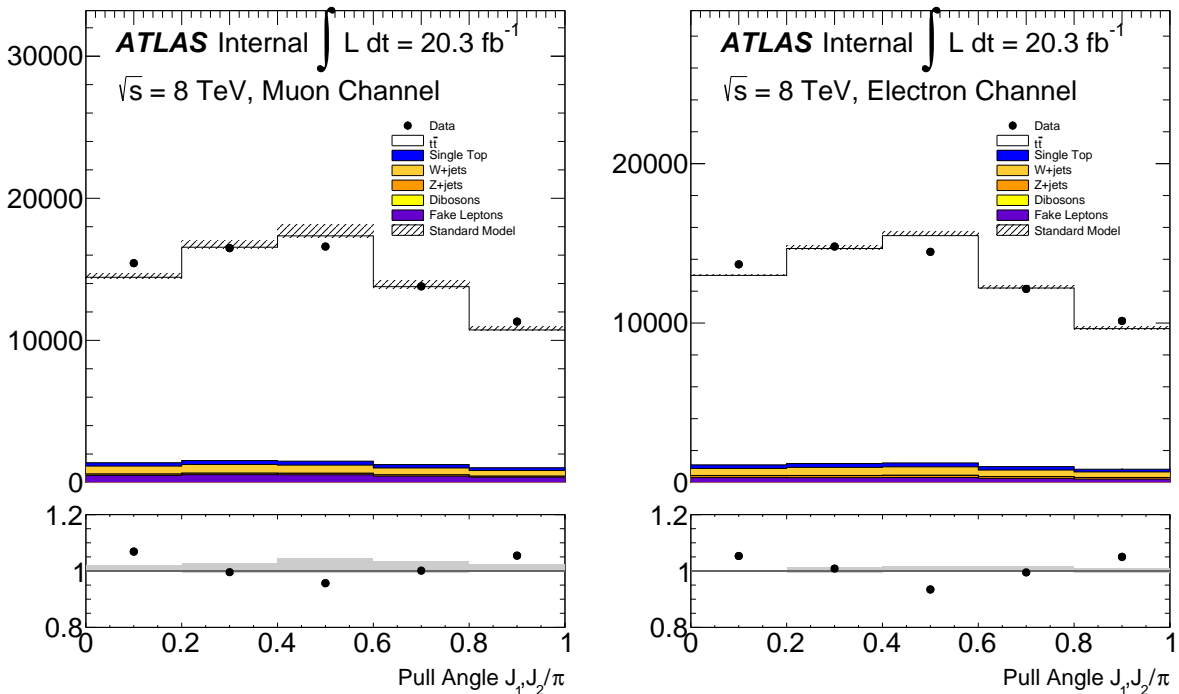


Figure 27: The jet pull angle for  $J_1$  with respect to  $J_2$  with the jet origin correction (but no cluster correction). One can clearly see the mis-modelling of the jet angular resolution.

Not reviewed, for internal circulation only

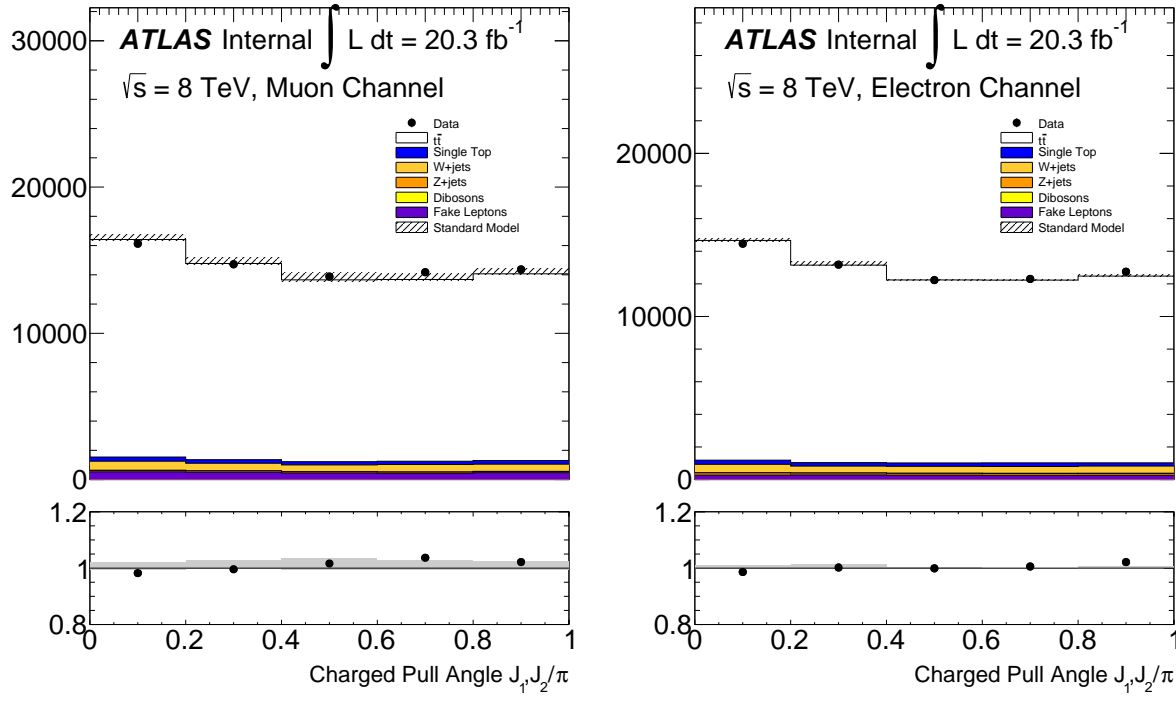


Figure 28: The jet track pull angle for  $J_1$  with respect to  $J_2$  with the jet origin correction (but no cluster correction). One can clearly see the mis-modelling of the jet angular resolution.

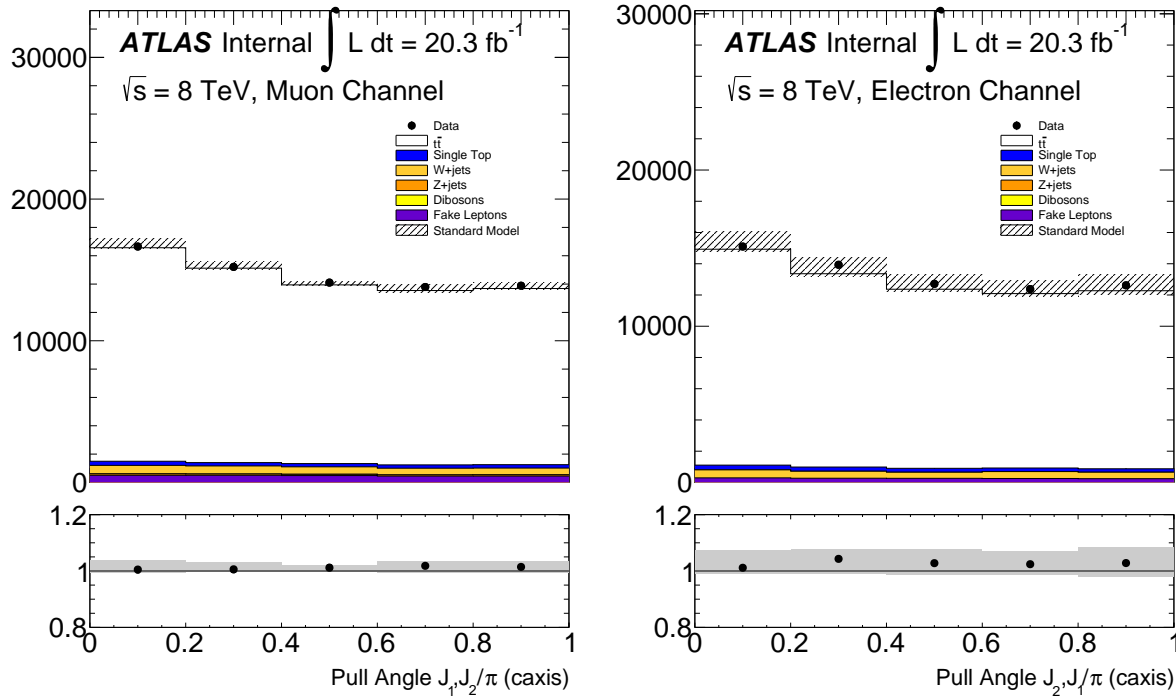


Figure 29: The jet pull angle for  $J_1$  with respect to  $J_2$  with cluster origin corrections and the jet axis constructed from the four-vector sum of clusters.

Not reviewed, for internal circulation only

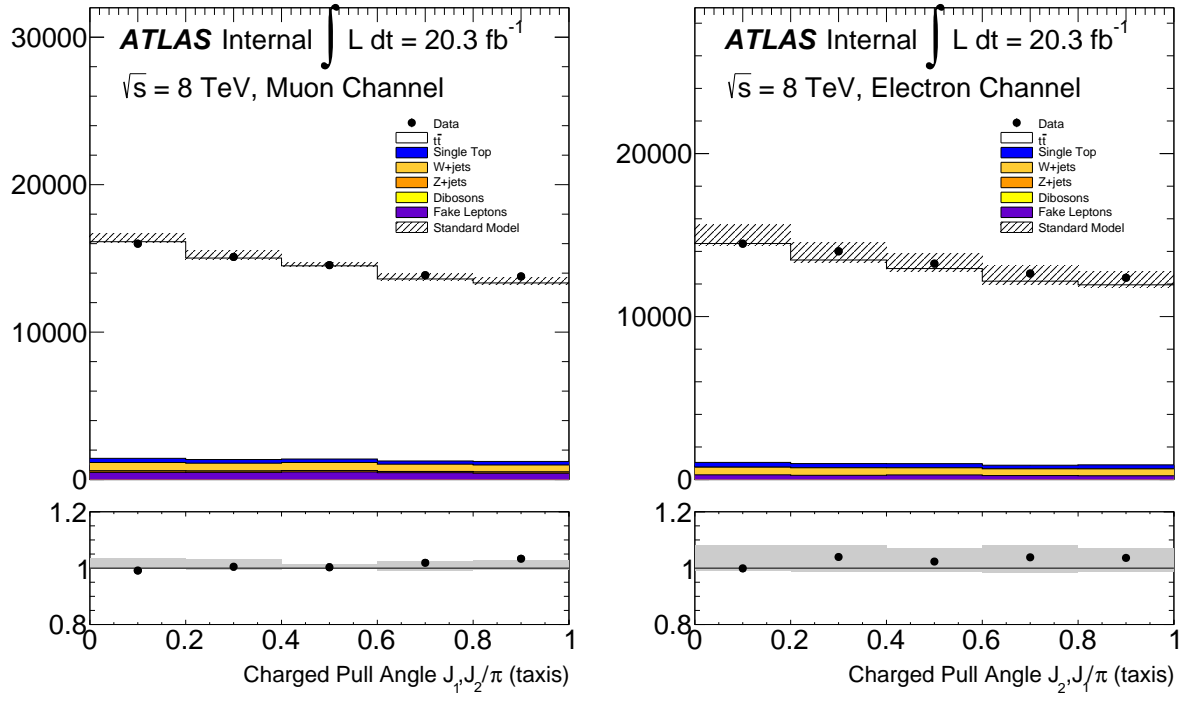


Figure 30: The jet track pull angle for  $J_1$  with respect to  $J_2$  were the jet axis is the four-vector sum of tracks.

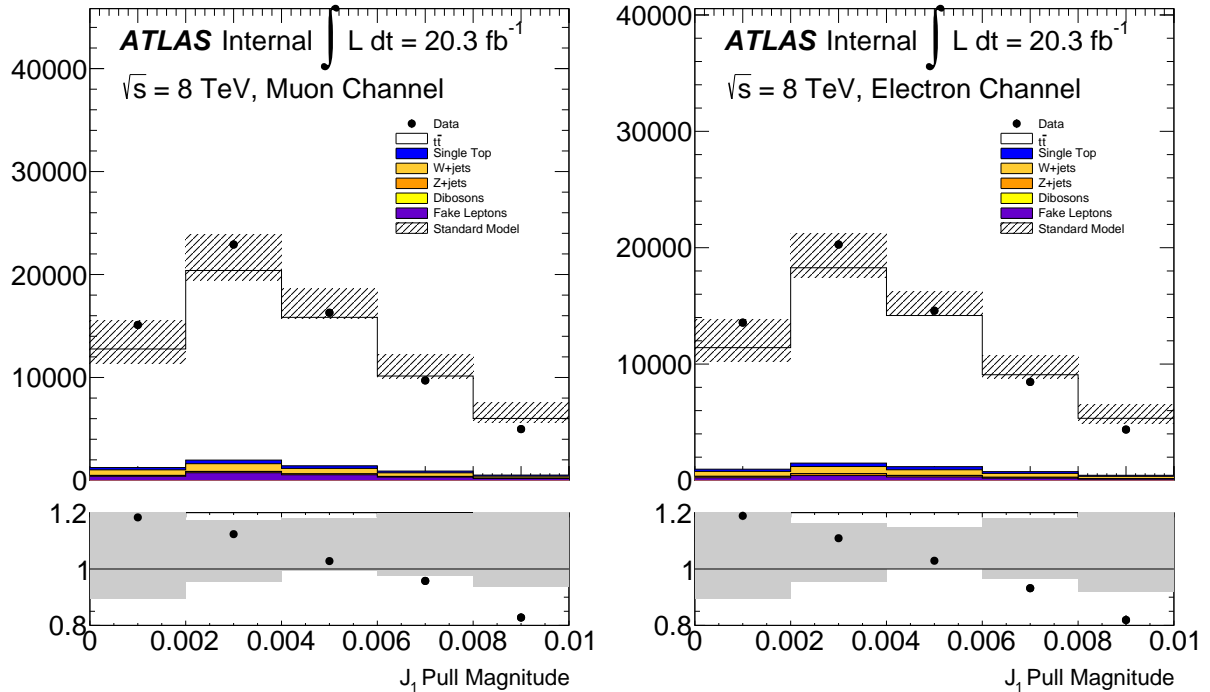


Figure 31: The jet pull vector magnitude for  $J_1$  with the jet origin correction (but no cluster correction). One can clearly see the mis-modelling of the jet angular resolution.

Not reviewed, for internal circulation only

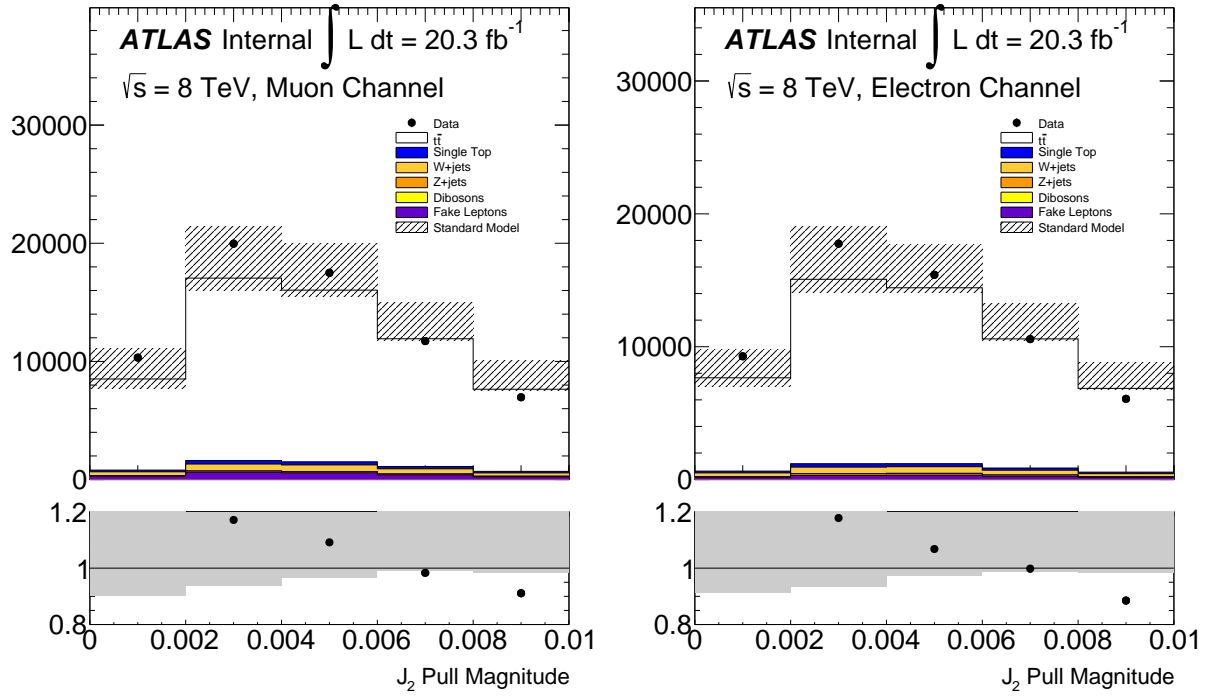


Figure 32: The jet pull vector magnitude for  $J_2$  with the jet origin correction (but no cluster correction). One can clearly see the mis-modelling of the jet angular resolution.

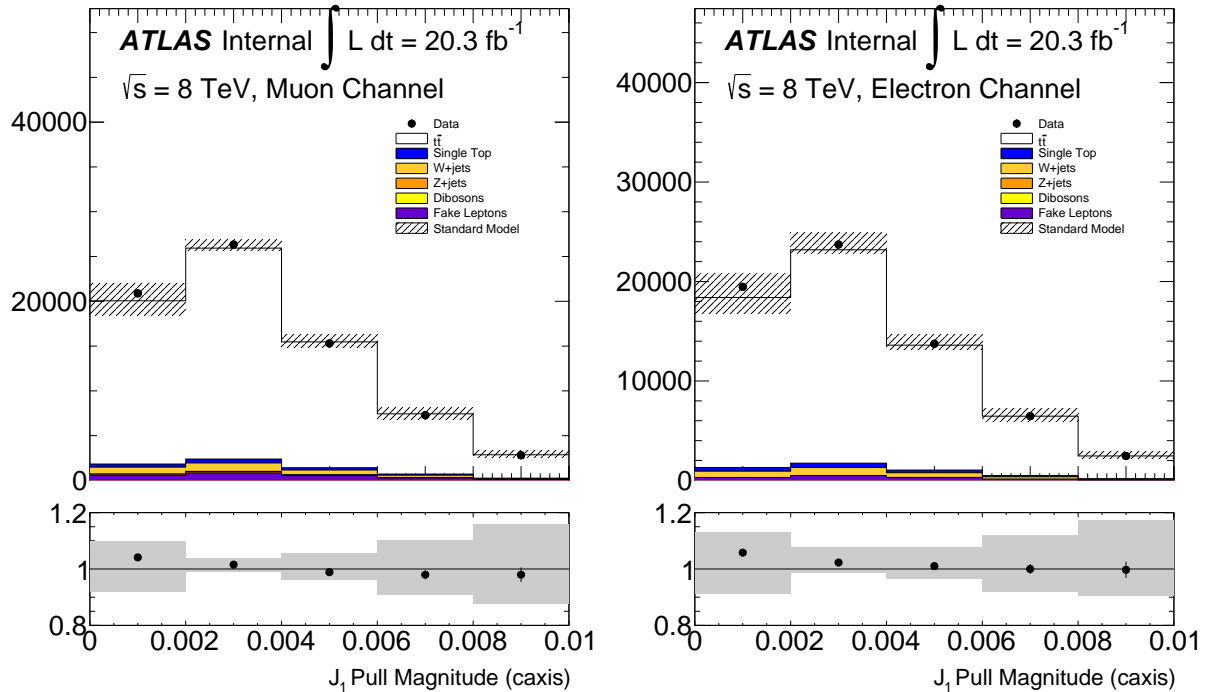


Figure 33: The jet pull vector magnitude for  $J_1$  with cluster origin corrections and the jet axis constructed from the four-vector sum of clusters.

Not reviewed, for internal circulation only

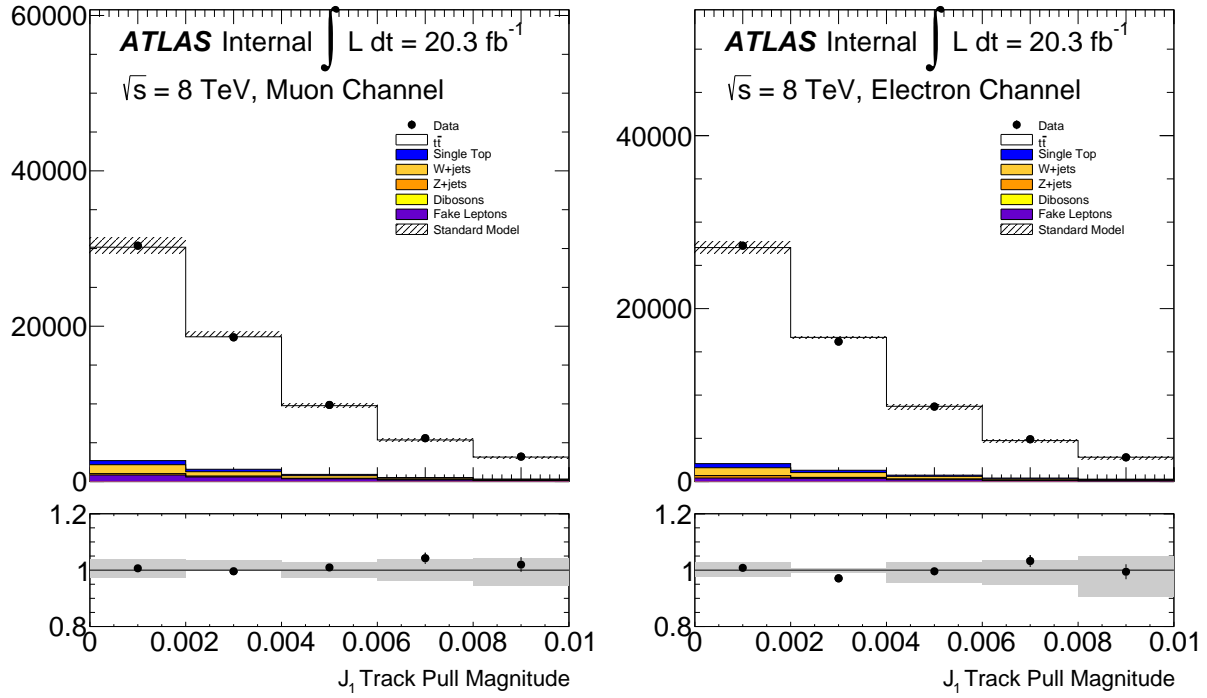


Figure 34: The jet track pull vector magnitude for  $J_1$  with the jet origin correction (but no cluster correction). One can clearly see the mis-modelling of the jet angular resolution.

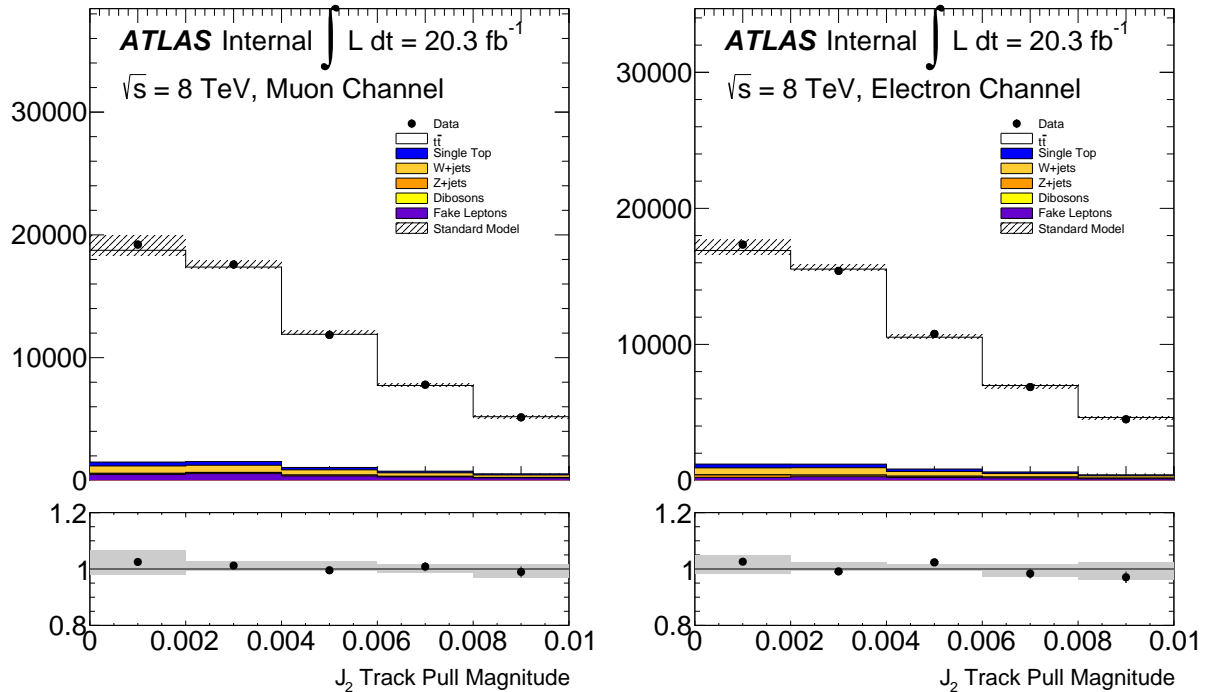


Figure 35: The jet track pull vector magnitude for  $J_2$  with the jet origin correction (but no cluster correction). One can clearly see the mis-modelling of the jet angular resolution.

Not reviewed, for internal circulation only

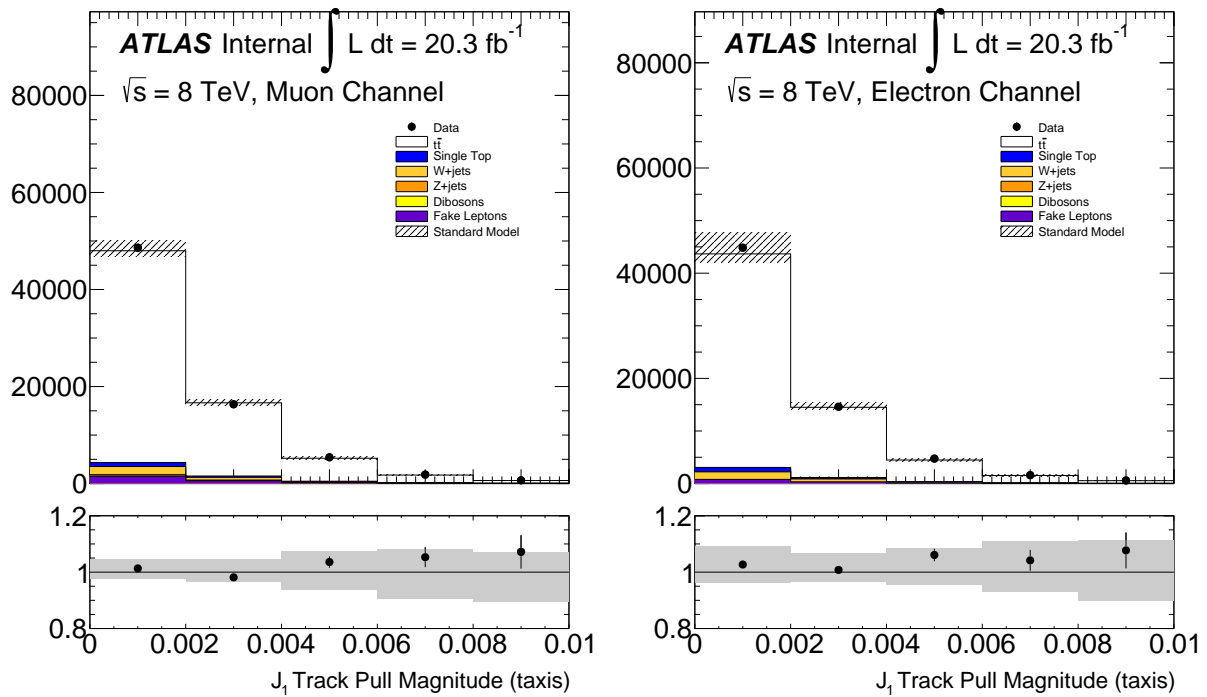


Figure 36: The jet track pull vector magnitude for  $J_1$  were the jet axis is the four-vector sum of tracks.

## 492 6.2 Fast versus Full Detector Simulation

493 The nominal samples used in the analysis as well as all experimental systematic uncertainties are com-  
 494 puted using full detector simulation. However, some of the theoretical systematic uncertainties are es-  
 495 timated with fast simulation. Many analyses in ATLAS use the fast detector simulation ATLAS Fast II  
 496 (AFII) in order to increase MC statistics. This section contains comparisons for key variables between  
 497 AFII and the full detector simulation. Figures 37, 38, 39, and 40 show the basic kinematic selection of  
 498 the leading and subleading jets. These are expected to be well-modeled by the fast simulation. There are  
 499 some notable differences, especially at low  $p_T$ , but these are due mostly to the fact that a different tune of  
 500 Pythia was used for the full and fastsim samples (the jet resolution is also different). Figure 45 shows for  
 501 instance that the  $p_T$  spectrum differences are already apparent at truth level. This difference in tune does  
 502 not impact the pull angle (Fig. 46), but does have a small impact on the pull vector magnitude (Fig. 47).

503 The remaining figures show the jet substructure variables, in particular the jet pull angle and pull  
 504 vector magnitude. Figures 41 and 42 show the pull angle between  $J_1$  and  $J_2$  (as well as vice versa) for  
 505 the calorimeter pull and the track pull, respectively. The corresponding pull vector magnitudes are shown  
 506 in Fig. 43 and 44. Since the fastsim tracking is the same as the fullsim tracking, as expected, the charged  
 507 particle pull angle is reasonably well modeled by the fastsim. The all particles pull angle is not well  
 508 modeled.

Not reviewed, for internal circulation only

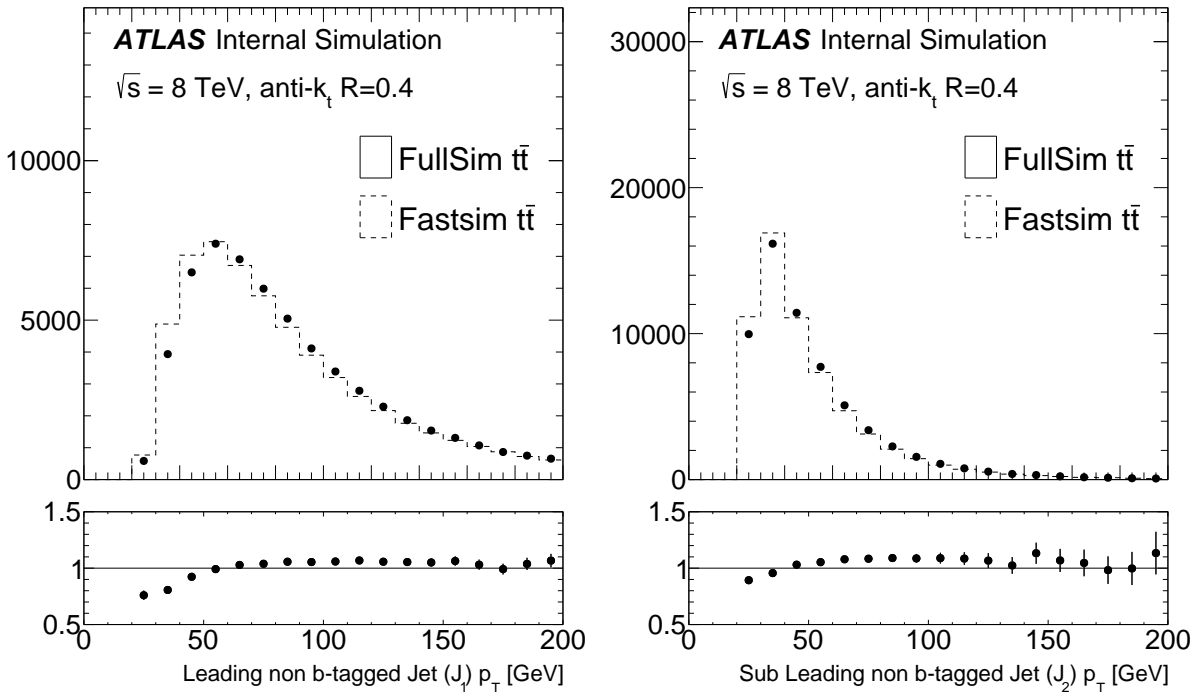
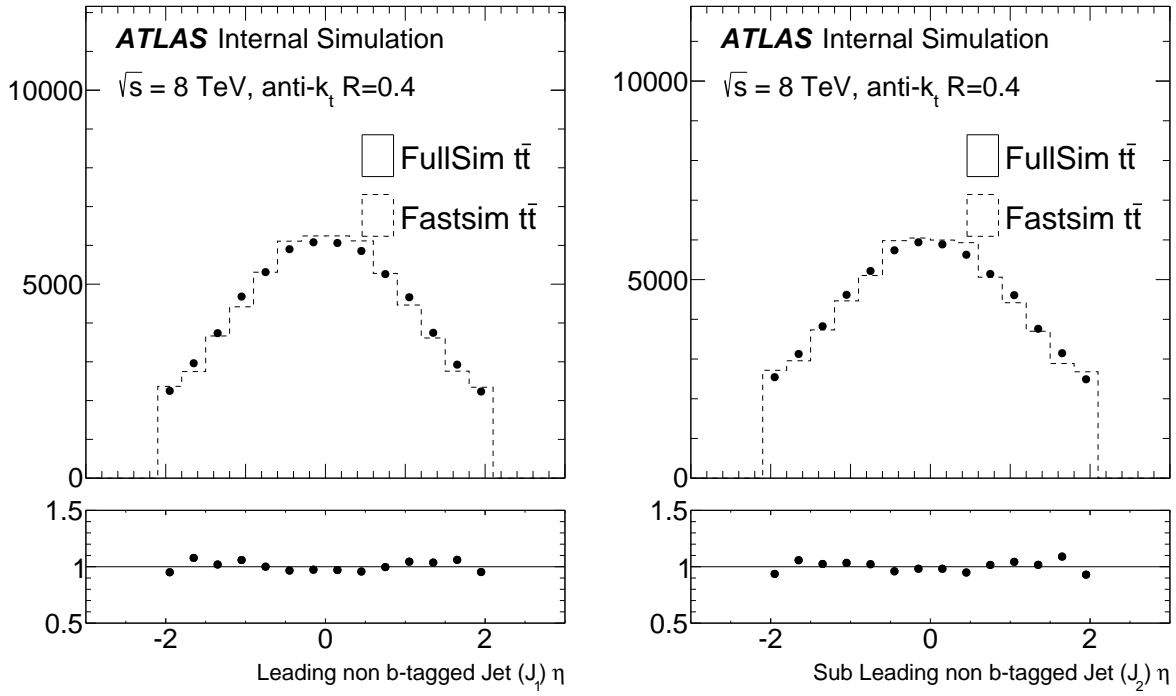
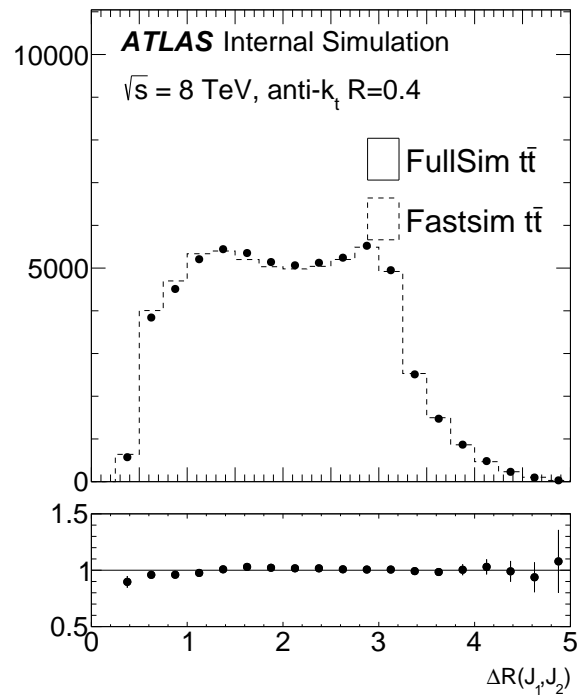


Figure 37: The leading and sub-leading  $W$  daughter jet  $p_T$ .

Not reviewed, for internal circulation only

Figure 38: The leading and sub-leading  $W$  daughter jet  $\eta$ .Figure 39: The  $\Delta R$  between  $J_1$  and  $J_2$ .

Not reviewed, for internal circulation only

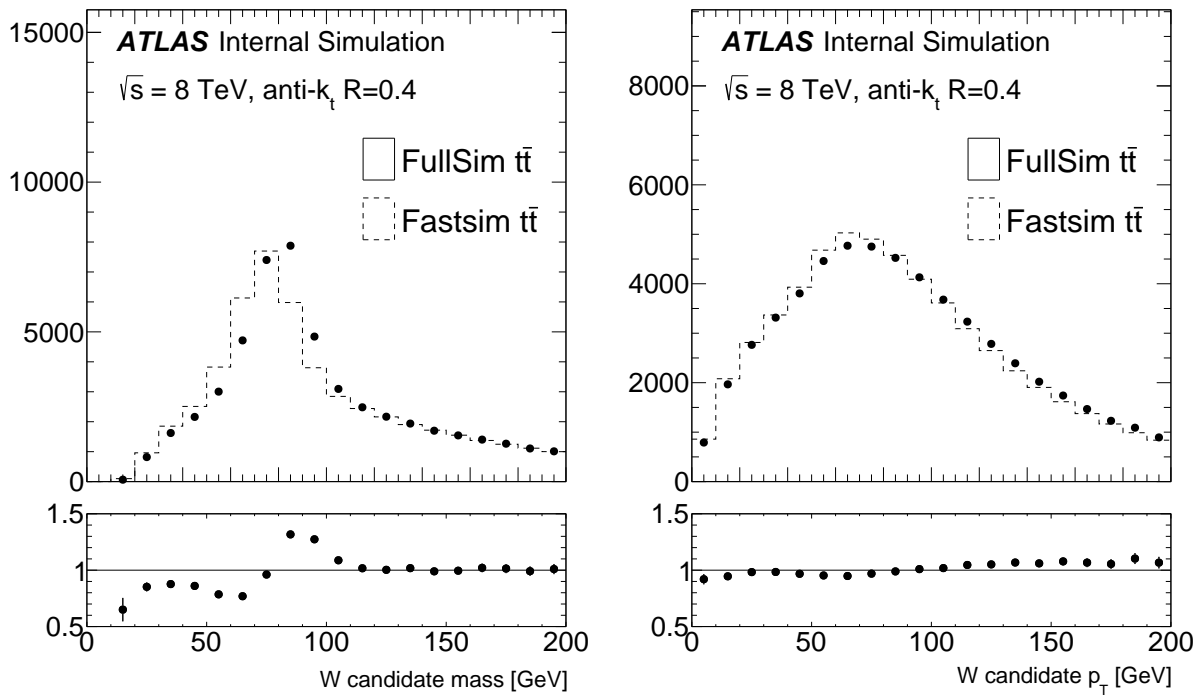


Figure 40: The dijet invariant mass (left) and  $p_T$  (right) of the combination of the leading and subleading  $W$  daughter candidate 4-vectors.

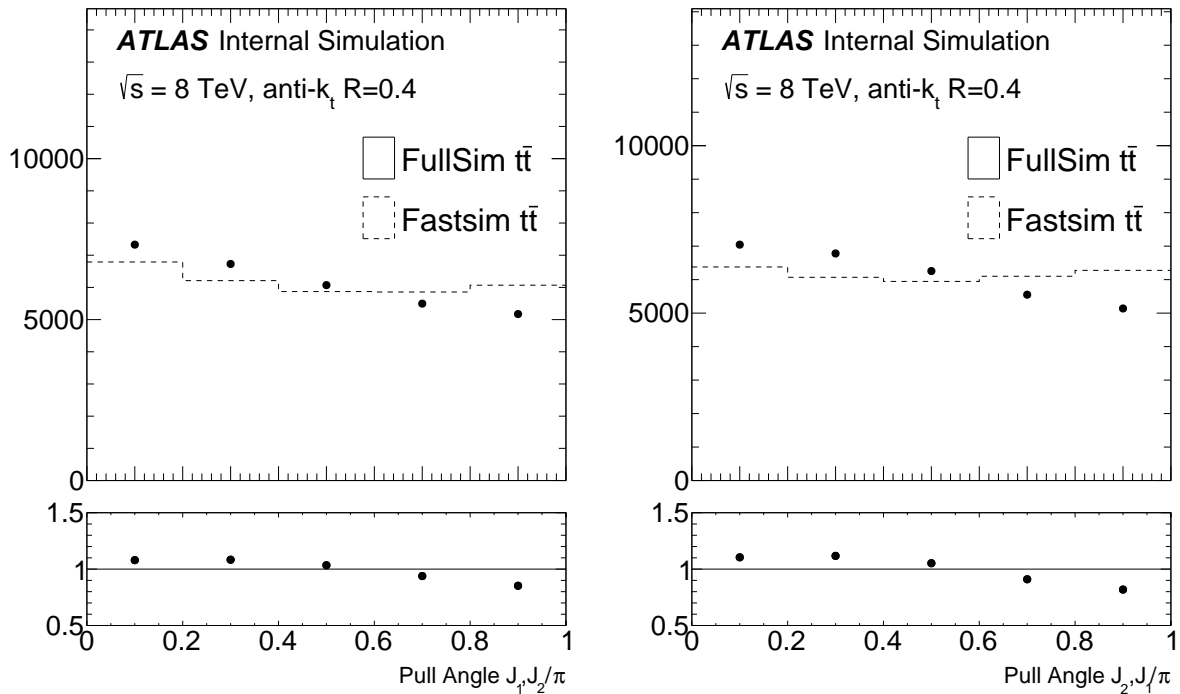
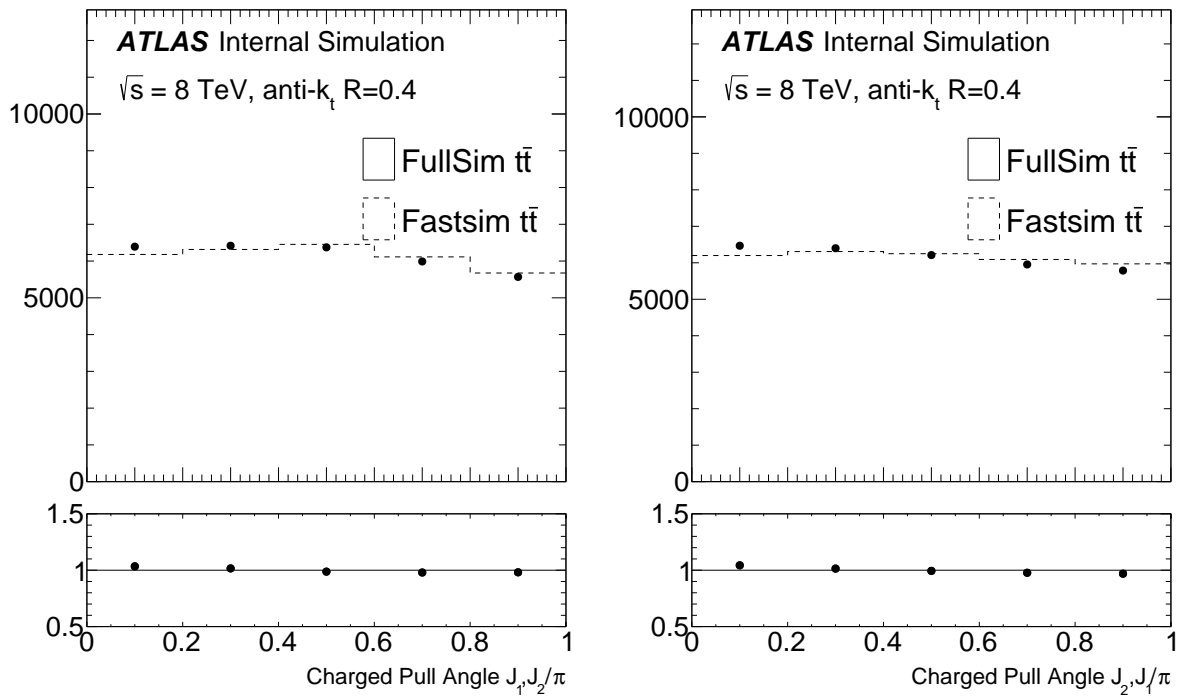
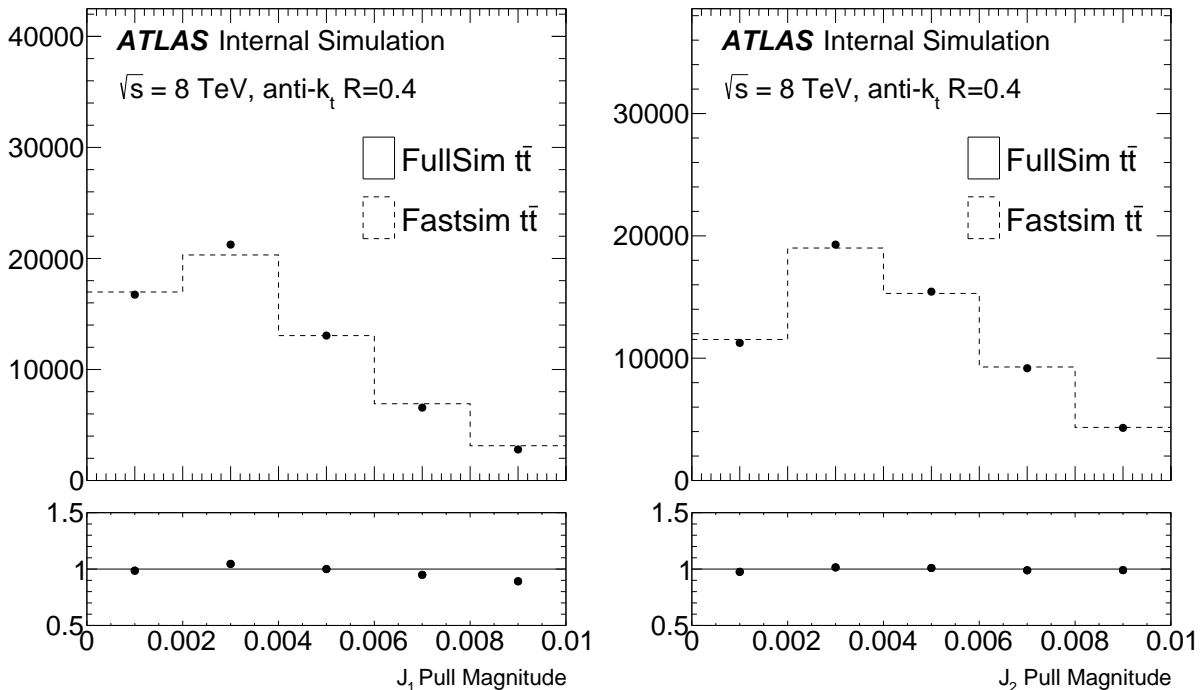
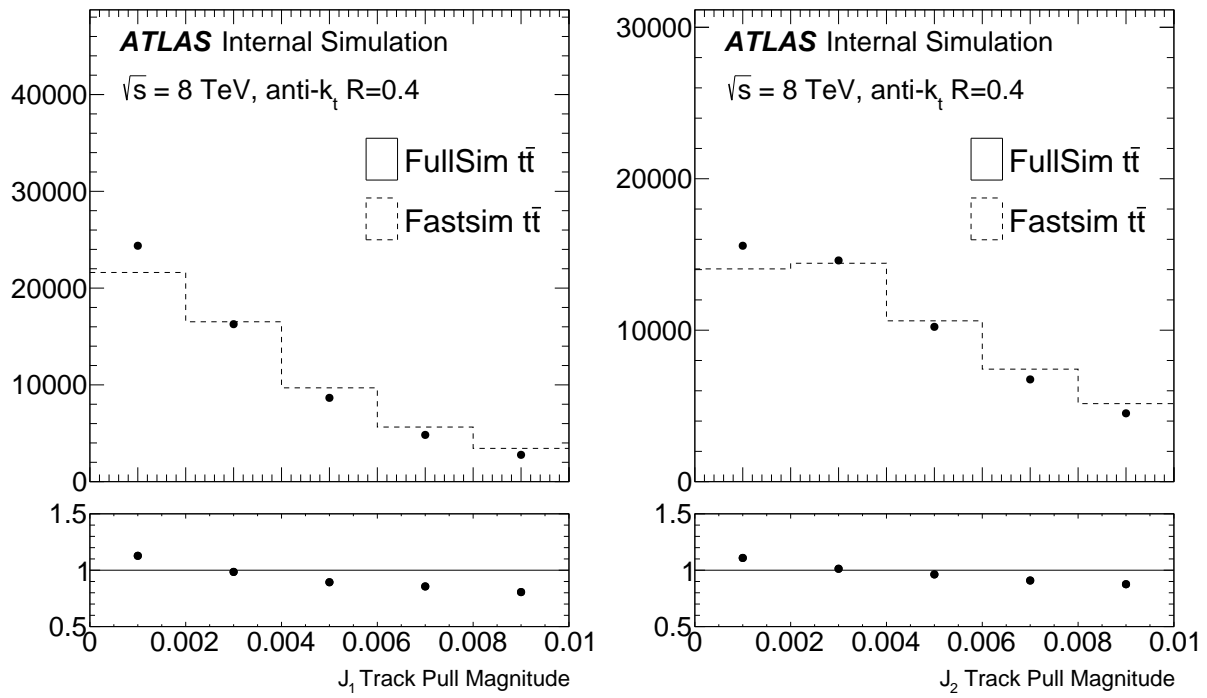
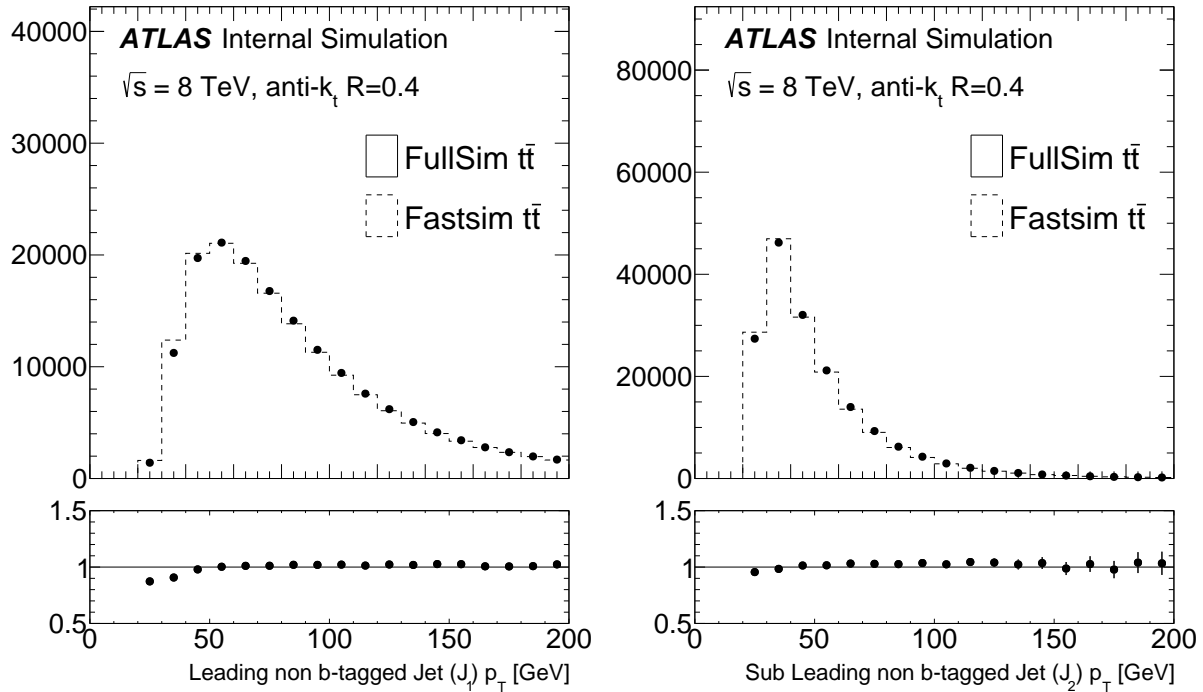


Figure 41: The jet pull angle for  $J_1$  with respect to  $J_2$  (left) and for  $J_2$  with respect to  $J_1$  (right).

Not reviewed, for internal circulation only

Figure 42: The jet track pull angle for  $J_1$  with respect to  $J_2$  (left) and for  $J_2$  with respect to  $J_1$  (right).Figure 43: The jet pull vector magnitude for  $J_1$  (left) and  $J_2$  (right).

Not reviewed, for internal circulation only

Figure 44: The jet track pull vector magnitude for  $J_1$  (left) and  $J_2$  (right).Figure 45: The leading and sub-leading  $W$  daughter jet  $p_T$  at truth level.

Not reviewed, for internal circulation only

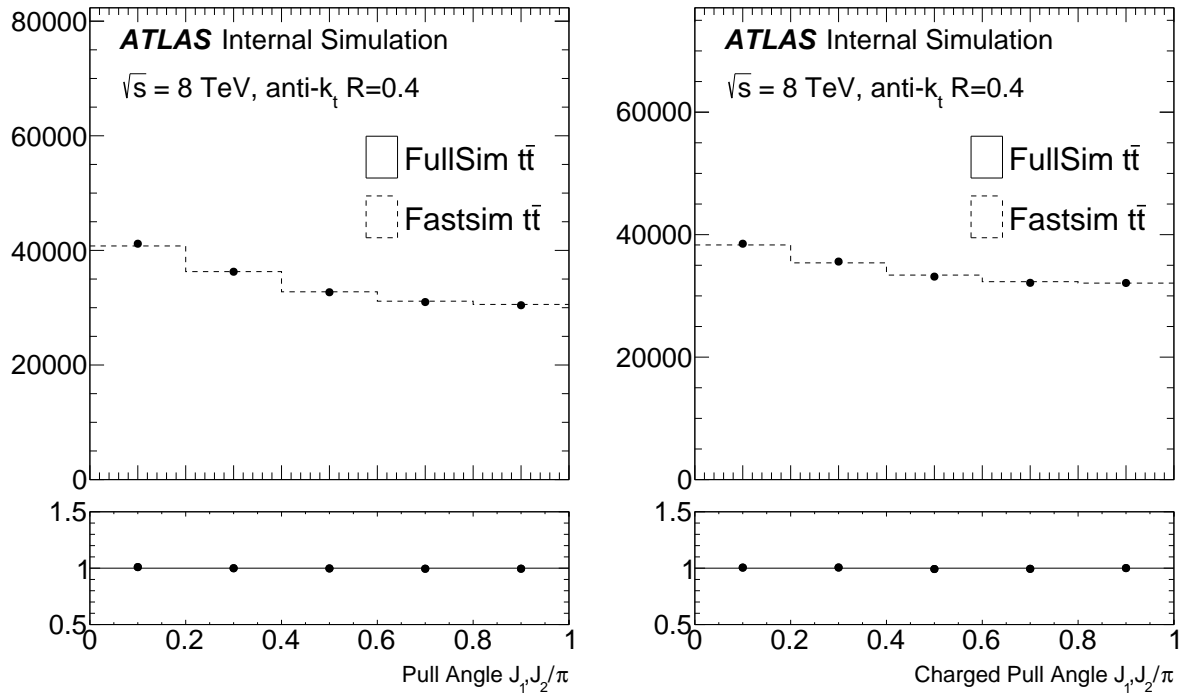


Figure 46: The jet pull angle for  $J_1$  with respect to  $J_2$  for all particles (left) and for charged particles (right) at truth level.

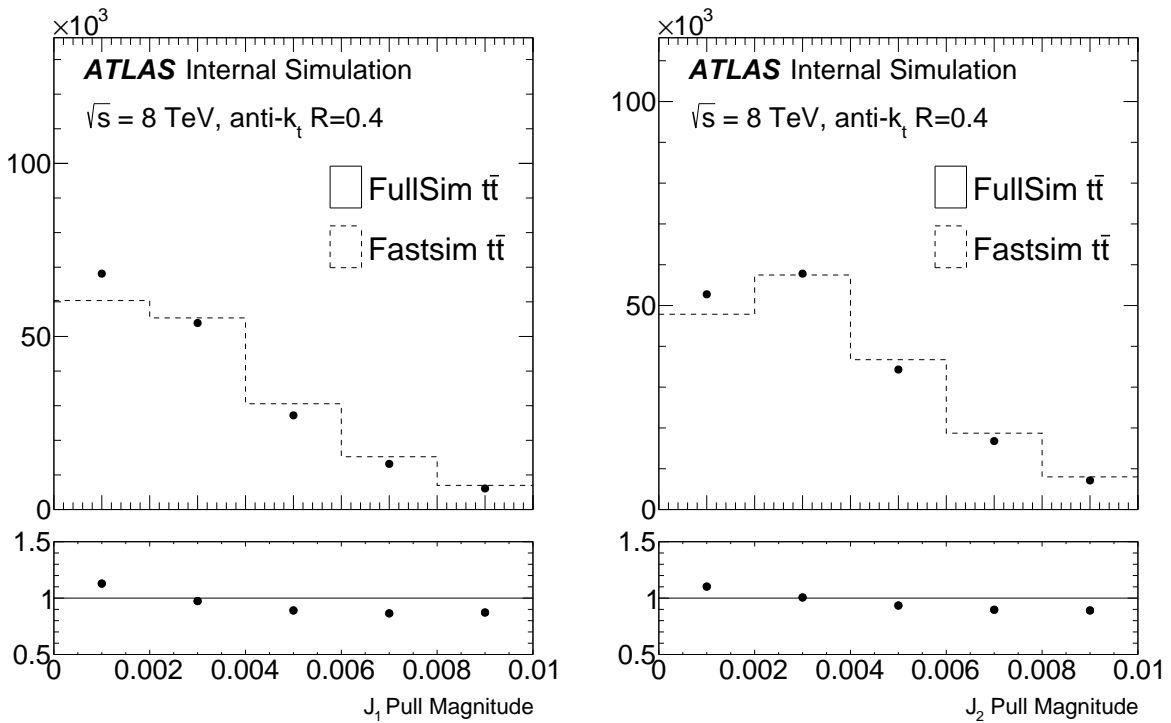


Figure 47: The jet pull vector magnitude for  $J_1$  (left) and  $J_2$  (right) at truth level.

## 509 7 Analysis Strategy

510 The analysis consists of two parts: unfold the pull angle distribution and compare the unfolded dis-  
 511 tribution to various color flow models. There are theoretical and experimental systematic uncertainties  
 512 associated with the response matrix used to compute the unfolded distribution. The impact of each source  
 513 of systematic uncertainty is estimated by varying the response matrix from the propagation of the uncer-  
 514 tainty’s impact on inputs to the event-by-event pull angle calculations. This will result in a systematic  
 515 error band on the unfolded distribution. Alongside this systematic uncertainty band is the statistical un-  
 516 certainty, which is computed by bootstrapping the data and re-running the unfolding procedure. For both  
 517 sources, the uncertainties are correlated across bins and so the relevant output is a covariance matrix. A  
 518 simple  $\chi^2$  can then be used to compare the unfolded data with various model predictions.

### 519 7.1 Background Estimation

520 The data/MC plots in Sec. 6 show that the estimated background composition is very small,  $\lesssim 10\%$ .  
 521 For most of these backgrounds, the pull angle is not expected to have any structure. The only non-  
 522 trivial background is the  $Wt$ -channel single top, for which there is a true hadronically decaying  $W$  boson  
 523 which should contain the same color structure as the ‘signal’  $t\bar{t}$ . This background constitutes less than one  
 524 percent of the total expected background yield and so this effect can be safely ignored. The backgrounds  
 525 are subtracted in the unfolding process.

### 526 7.2 Response Matrix Binning

527 From dedicated performance studies of the jet pull angle, it is known that the RMS of the response  
 528  $\theta_P^{\text{truth}} - \theta_P^{\text{reco}}$  depends on  $p_T$  and on the magnitude of the pull vector [26].

529 The number of bins used in the response matrices was chosen by requiring that the bin purities  
 530 (i.e. the diagonal entries of the response matrices) remain above 50%. The cut on  $|v_p|$  was fixed at  
 531  $|v_p| > 0.004$ , and the number of bins used in the response matrices were varied until an optimum was  
 532 found. The cut on  $|v_p|$  can be justified by considering the affect that changing the cut has on the ability to  
 533 distinguish the color-flipped pull distribution from the one produced by the Standard Model. Figure 48  
 534 shows comparisons of the truth-level Standard Model and color-flipped pull angle distributions obtained  
 535 using different choices of pull vector magnitude cut. It can be seen that the choice of  $|v_p| > 0.004$   
 536 maximises the difference between the Standard Model and color-flipped predictions for both the charged  
 537 and all particles pull angle distributions.

538 Figure 49 shows response matrices for the charged particle pull angle estimated using PowHeg+PYTHIA,  
 539 for three different choices of binning. When just three bins are used (Figure 49(a)) all diagonal entries  
 540 contain values larger than 50%. With 5 bins (Figure 49(c)) only the first and last bins along the diagonal  
 541 have entries larger than 50%, the remaining bins have values closer to 45% which is not optimal when  
 542 performing unfolding. When using 4 bins (Figure 49(b)) the second and third bins have diagonal entries  
 543 close to 50%. By optimizing the binning slightly and widening the second and third bins, all bin values  
 544 can be brought above 50%. A four bin pull angle distribution contains more information about the shape  
 545 of the distribution, and is preferable to the three bin version. The final choice of the binning for the  
 546 charged particle pull angle distribution is shown in Figure 50.

547 Equivalent plots for the all particles pull angle are shown in Figure 51. The dedicated performance  
 548 studies of the jet pull angle have shown that the RMS of the pull angle response is larger for the all particle  
 549 pull angle than for the charged particle equivalent. This can be clearly seen when looking at the four and  
 550 five bin response matrices shown in Figure 51(b) and (c). No four bin configuration could be found in  
 551 which all diagonal entries remained above 50%, and so the choice was made to use three bins as shown  
 552 in Figure 51(a).

Not reviewed, for internal circulation only

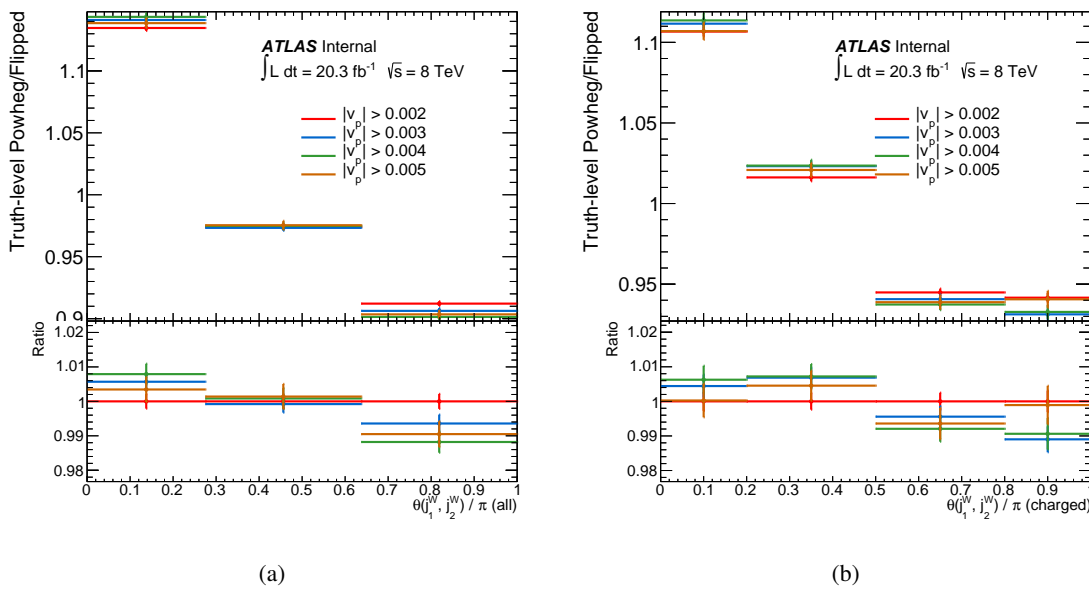


Figure 48: Comparisons between the truth-level predictions of the all particles (a) and charged particles (b) pull angle distributions produced using Standard Model and color-flipped  $t\bar{t}$  MC samples, for different choices of pull vector magnitude cut.

Not reviewed, for internal circulation only

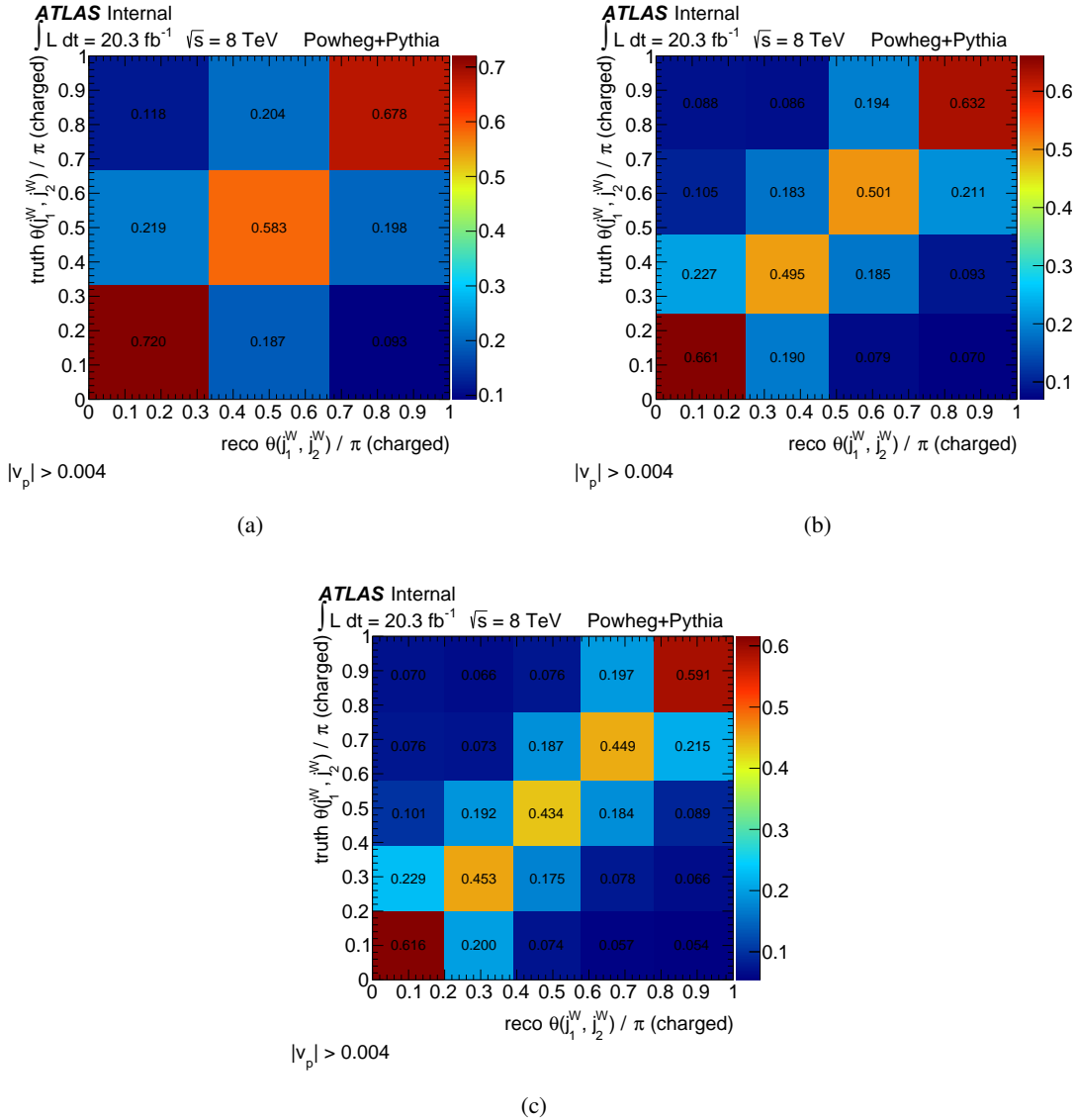
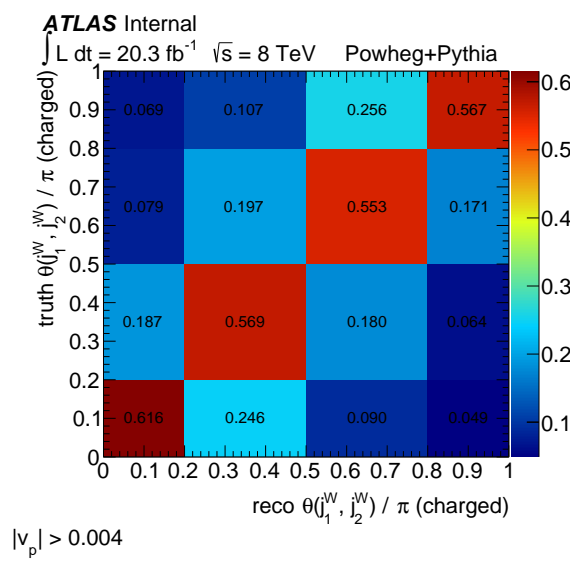


Figure 49: Response matrices for the charged particle pull angle estimated using PowHeg+PYTHIA. Three different choices of binning are explored.

Not reviewed, for internal circulation only



(a)

Figure 50: Response matrix for the charged particle pull angle using the final choice of binning, estimated with PowHeg+PYTHIA.

Not reviewed, for internal circulation only

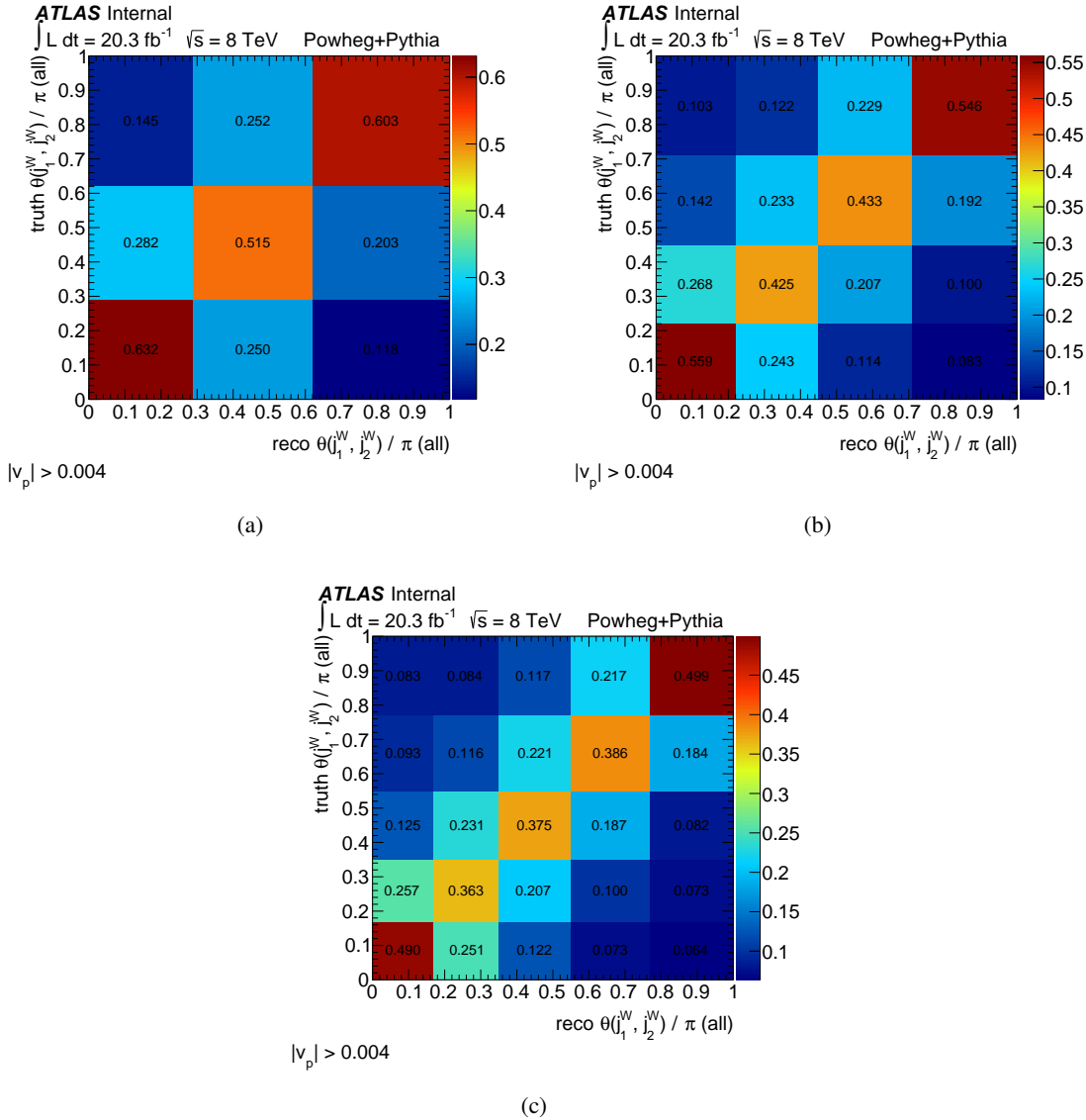


Figure 51: Response matrices for the all particles pull angle estimated using PowHeg+PYTHIA. Three different choices of binning are explored.

## 553 8 Systematic Uncertainties

554 Systematic uncertainties come in two varieties: experimental and theoretical. The procedure for esti-  
 555 mating each source is described one at a time in the sections below. Note that since there are two input  
 556 constituents, not all uncertainties impact both definitions of the pull angle. This is specified explicitly  
 557 after each item.

### 558 8.1 Experimental Uncertainties

559 **Jet energy scale** The jet energy is scaled up and down (in a fully correlated way) by the  $\pm 1\sigma$  uncertainty  
 560 on the jet energy scale obtained using the tool provided by the Jet/Etmiss group [62]. This is  
 561 not expected to have a large impact on the measurement since the jet energy does not change  
 562 the pull angle. It will however, impact the acceptance directly through the  $p_T$  thresholds and  
 563 indirectly through the pull vector magnitude. Impacts **both** the track and calorimeter pull angle.  
 564 Uncertainties are computed using `JetUncertainties-00-08-07` [50].

565 **Jet energy resolution** An extra  $p_T$  smearing is added to the jets based on their  $p_T$  and  $\eta$  to account for  
 566 a possible underestimate of the jet energy resolution in the MC simulation. This impacts the final  
 567 result (i.e. only through the acceptance) as the jet energy scale uncertainty. Impacts **both** the track  
 568 and calorimeter pull angle.

569 **Tracking Efficiency** The tracking reconstruction efficiency systematic uncertainty is estimated by re-  
 570 moving tracks associated to jets with an  $\eta$  dependent probability [63]. The probability in the  
 571 region  $2.3 < |\eta| < 2.5$  is 7%,  $1.9 < |\eta| < 2.3$  corresponds to 4%,  $1.3 < |\eta| < 1.9$  is 3%, and  
 572  $0. < |\eta| < 1.3$  is 2%. This uncertainty **only** impacts track pull.

573 **Tracking  $p_T$**  Tracks are removed with some probability depending on the jet  $p_T$ . There is no expected  
 574 loss for jets below 400 GeV. Between 400 and 500 GeV, 0.08% of tracks are removed (randomly),  
 575 for jets between 500 and 600 GeV, we remove 0.8%, between 600 and 800 we remove 1.9% and  
 576 between 800 and 1000 we remove 3.7%. There is currently no prescription for jets above 1 TeV  
 577 (which is inconsequential for this analysis). This uncertainty **only** impacts track pull.

578 **Angular Resolution** There are several methods for estimating the angular resolution uncertainty on the  
 579 jet axis. One method is to use the measured angular resolution (and uncertainty) between track  
 580 jets and calorimeter jets, described in Appendix B.2. For reasons described in the appendix, we  
 581 do not use this method and instead estimate the jet angular resolution uncertainty from the prop-  
 582 agated uncertainties in the cluster uncertainties. In other words, whenever the clusters are varied  
 583 in accordance with one of the uncertainty procedures described below, the jet axis is recomputed  
 584 and so the smearing of the jet axis is accounted for, in a fully correlated manner, with the cluster  
 585 uncertainties.

586 To evaluate the calorimeter cluster experimental uncertainties, prescriptions similar to those used in  
 587 previous analyses [65–67], which were based on previous E/p measurements [68] are evaluated using the  
 588 most current data.

589 **Cluster Angular Resolution** The 2011 prescription for the cluster angular resolution uncertainty is to  
 590 smear all clusters independently by 5 mrad [69] in both  $\eta$  and  $\phi$ . The 5 mrad was determined by studies  
 591 of the differences between data and MC in the  $\Delta\phi/\eta$  between isolated tracks and isolated clusters. Recent  
 592 studies with the 2012 dataset<sup>11</sup> have been performed and those results are presented here. Overall, we  
 593 find that when we control for neutral particles, the cluster angular resolutions are much better (by a factor  
 594 of 5 in the endcap and 50 in the barrel) than the 2011 studies. This is most likely due to the removal  
 595 of the contribution from neutrals. **To be conservative, we use the 5 mrad prescription from 2011.**  
 596 Additional validation for the modeling of the energy of clusters in bins of cluster isolation are shown in  
 597 Appendix B.3.

598 For the 2012 study of the cluster angular resolution, a selection enriched in  $Z \rightarrow \mu\mu$  ( $p_T^Z > 30$   
 599 GeV) events is chosen. Tracks are selected which have a maximum of one cluster within  $\Delta R < 0.15$   
 600 around their position extrapolated to the second layer of the calorimeter. Fig. 52 shows the distribution  
 601 of  $\Delta R(\text{track, calo})$  for such tracks in the barrel,  $|\eta| < 0.6$  (endcap  $2 < |\eta| < 2.4$  in Fig. 53). In all plots,  
 602 there are clearly two peaks. The first peak is from clusters due to a single charged particle, whereas the  
 603 second peak comes from cases in which there is also a neutral particle in the same cluster (which shifts  
 604 the cluster center). To study the impact of single particles, further analysis is only performed on cases in  
 605 which  $\Delta R(\text{track, calo}) < 0.075$  to remove the second peak.

606 Figures 54, 55, 56 and 57 show the data and MC distributions and differences between  $\Delta\eta$  and  $\Delta\phi$   
 607 in various regions of the calorimeters in both the barrel and endcap. The plots that are denoted ‘second  
 608 layer’ have no further selections on tracks and clusters. The plots with other designations have further  
 609 requirements on the clusters (tracks still extrapolated to the second layer):

```
610 Lar: |eta|<0.6 && log10(cl_centerlambda->at(minDRi))>2.2 &&
611     log10(cl_centerlambda->at(minDRi))<2.5
612 Tile: |eta|<0.6 && log10(cl_centerlambda->at(minDRi))>2.9 &&
613     log10(cl_centerlambda->at(minDRi))<3.2
614 LAr: 2.0<|eta|<2.4 && std::fabs(sinh(cl_em_eta->at(minDRi))*  

615     cl_centermag->at(minDRi)/cosh(cl_em_eta->at(minDRi)))<4600.
616 HEC: 2.0<|eta|<2.4 && std::fabs(sinh(cl_em_eta->at(minDRi))*  

617     cl_centermag->at(minDRi)/cosh(cl_em_eta->at(minDRi)))>4600.
```

618 We find the the cluster angular uncertainties are comparable in the various regions.

Not reviewed, for internal circulation only

---

<sup>11</sup>The data in the following plots are from Chris Young; the tabulation and interpretation are presented here for the first time.

Not reviewed, for internal circulation only

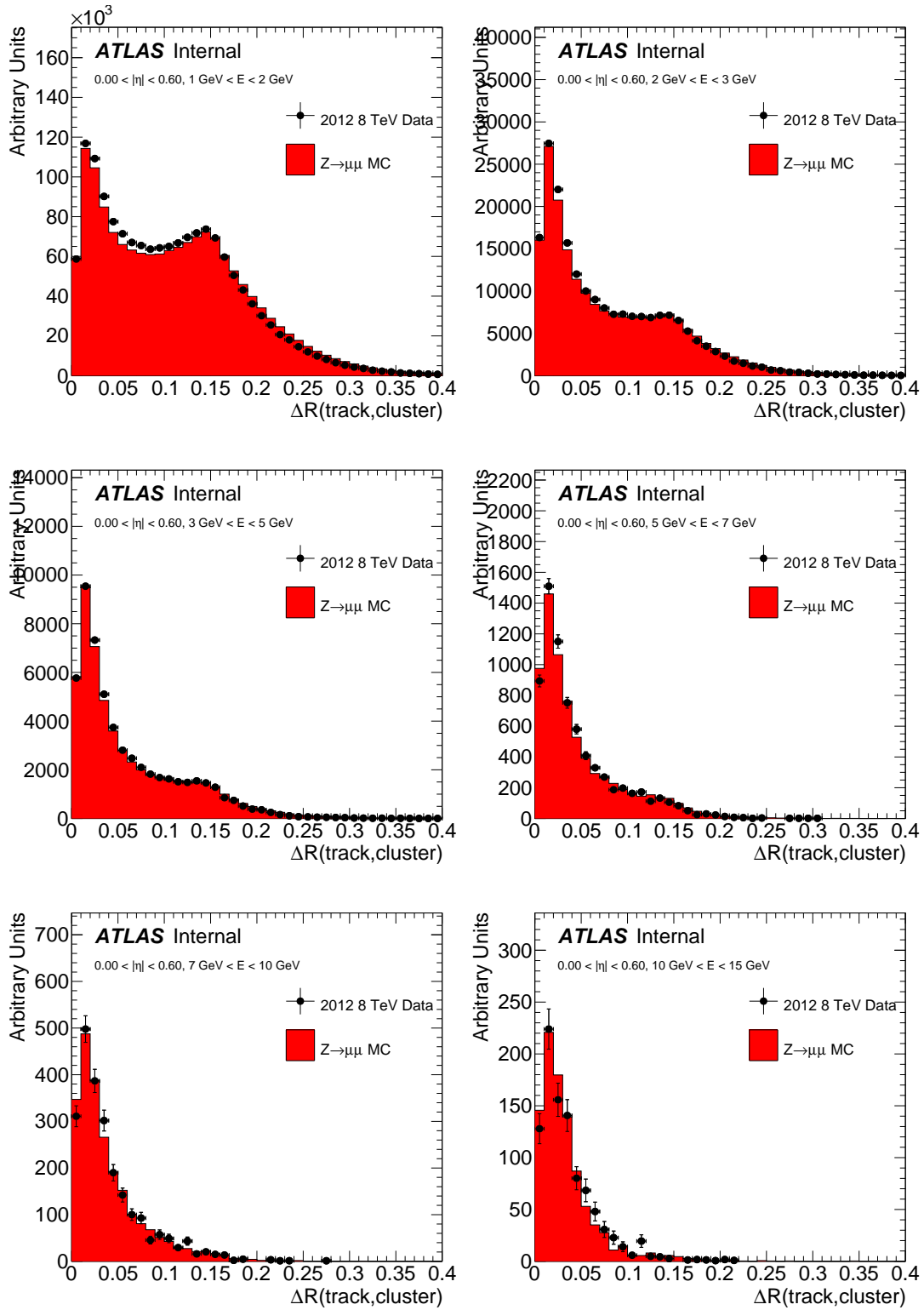


Figure 52: The  $\Delta R$  between isolated tracks and clusters in  $Z \rightarrow \mu\mu$  events in the barrel of the detector.

Not reviewed, for internal circulation only

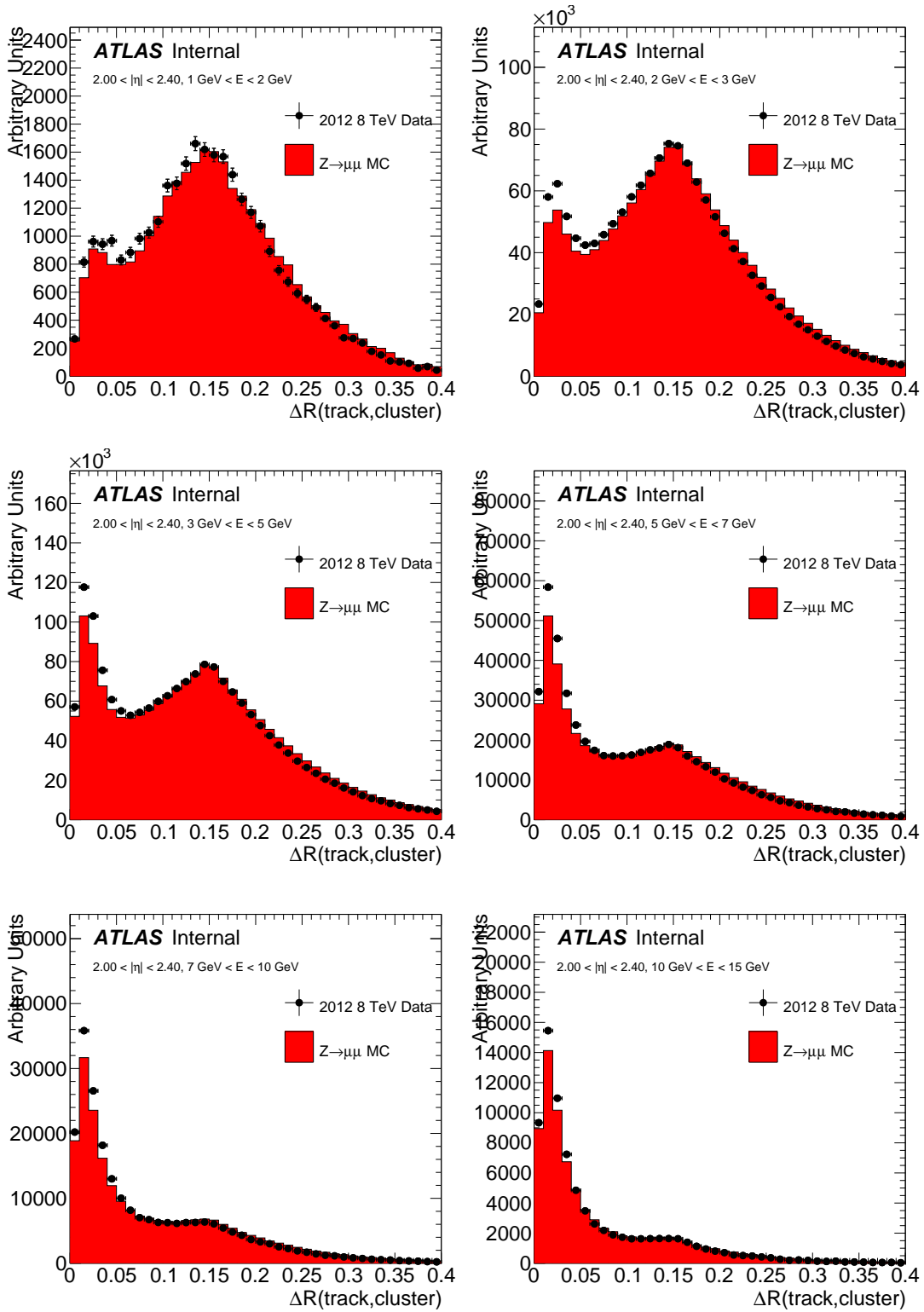


Figure 53: The  $\Delta R$  between isolated tracks and clusters in  $Z \rightarrow \mu\mu$  events in the endcap of the detector.

Not reviewed, for internal circulation only

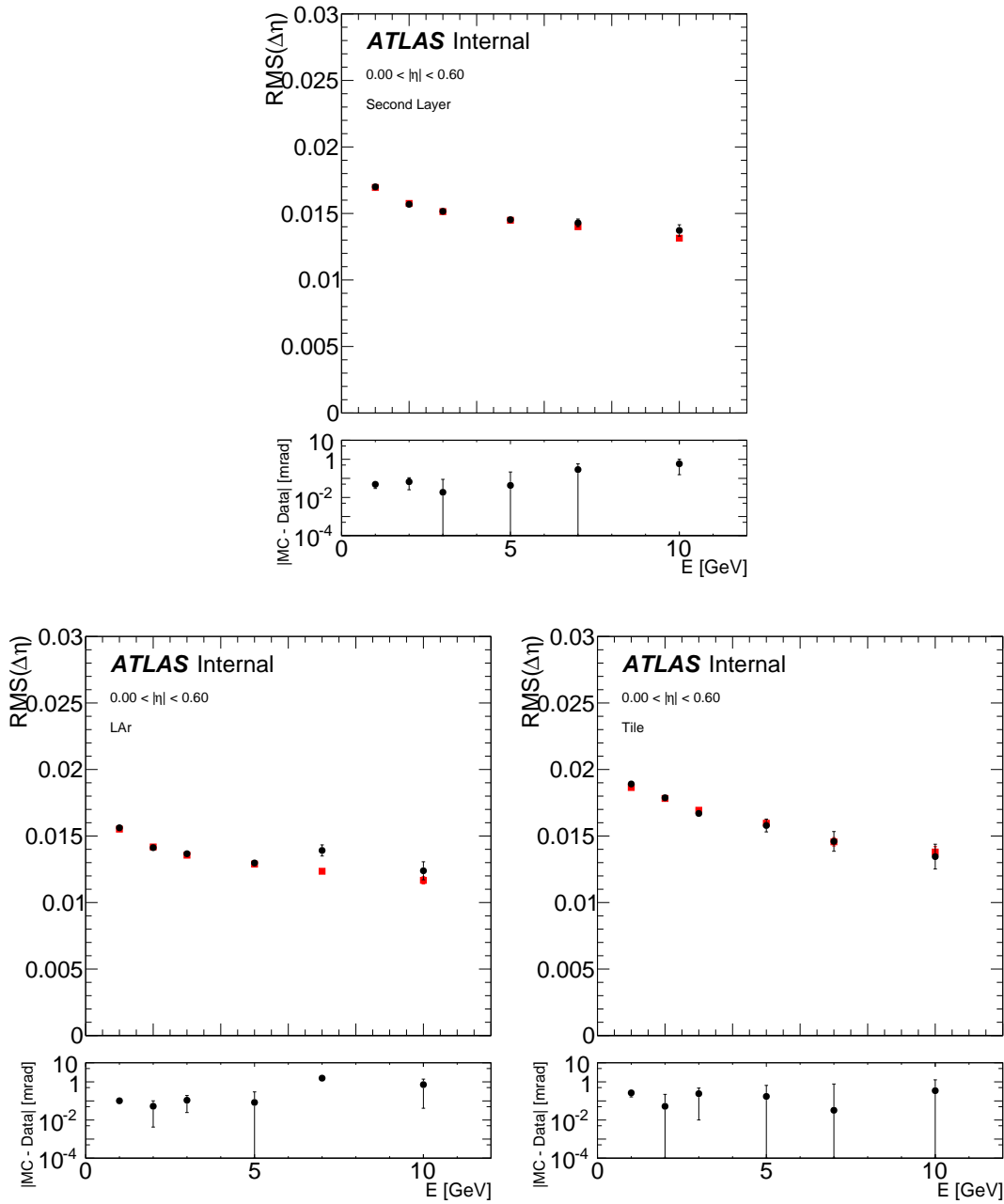


Figure 54: The differences between data and MC for the RMS of the  $\Delta\eta$  between isolated single particle tracks and clusters for various regions of the calorimeter in the barrel.

Not reviewed, for internal circulation only

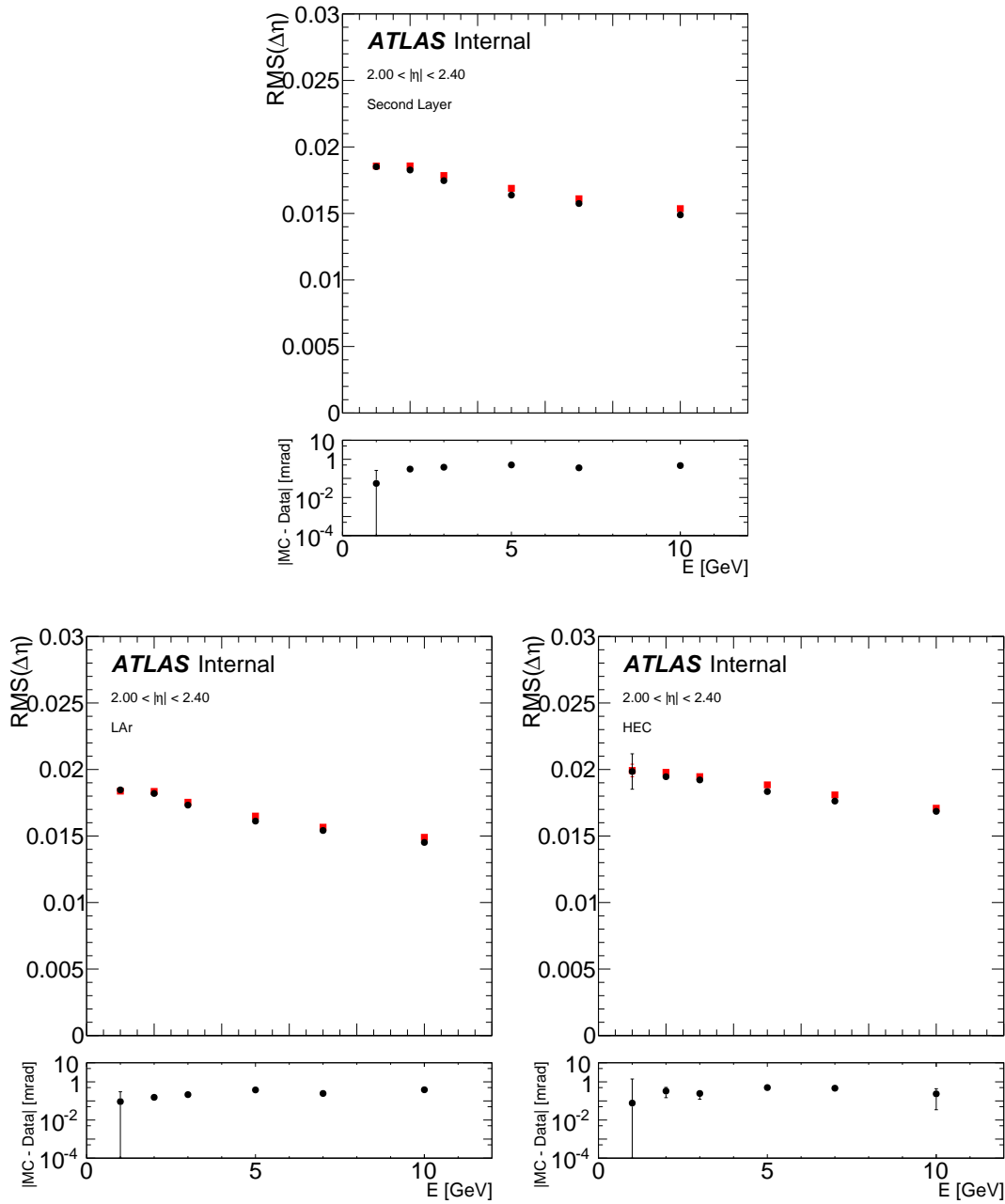


Figure 55: The differences between data and MC for the RMS of the  $\Delta\eta$  between isolated single particle tracks and clusters for various regions of the calorimeter in the endcap.

Not reviewed, for internal circulation only

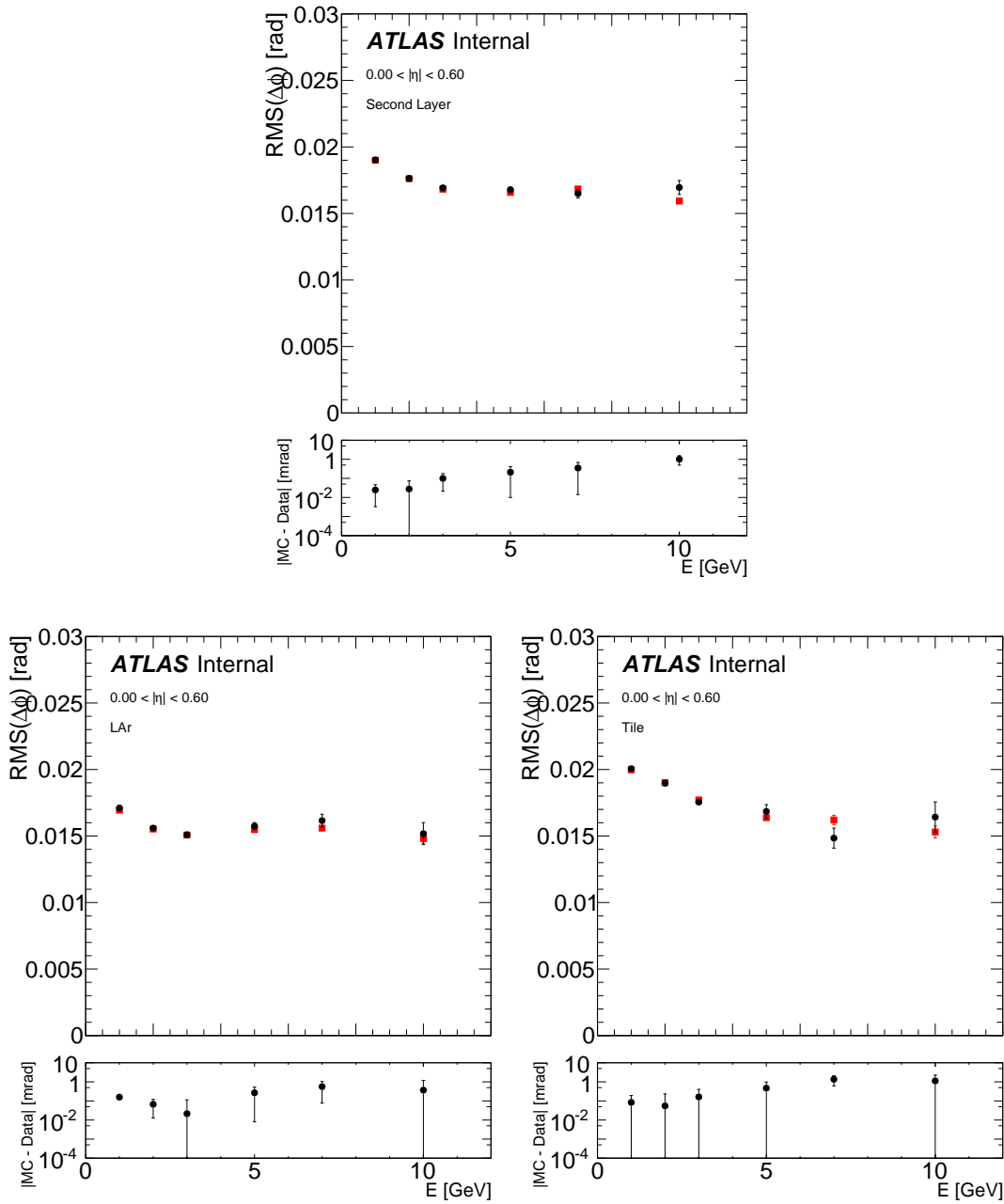


Figure 56: The differences between data and MC for the RMS of the  $\Delta\phi$  between isolated single particle tracks and clusters for various regions of the calorimeter in the barrel.

Not reviewed, for internal circulation only

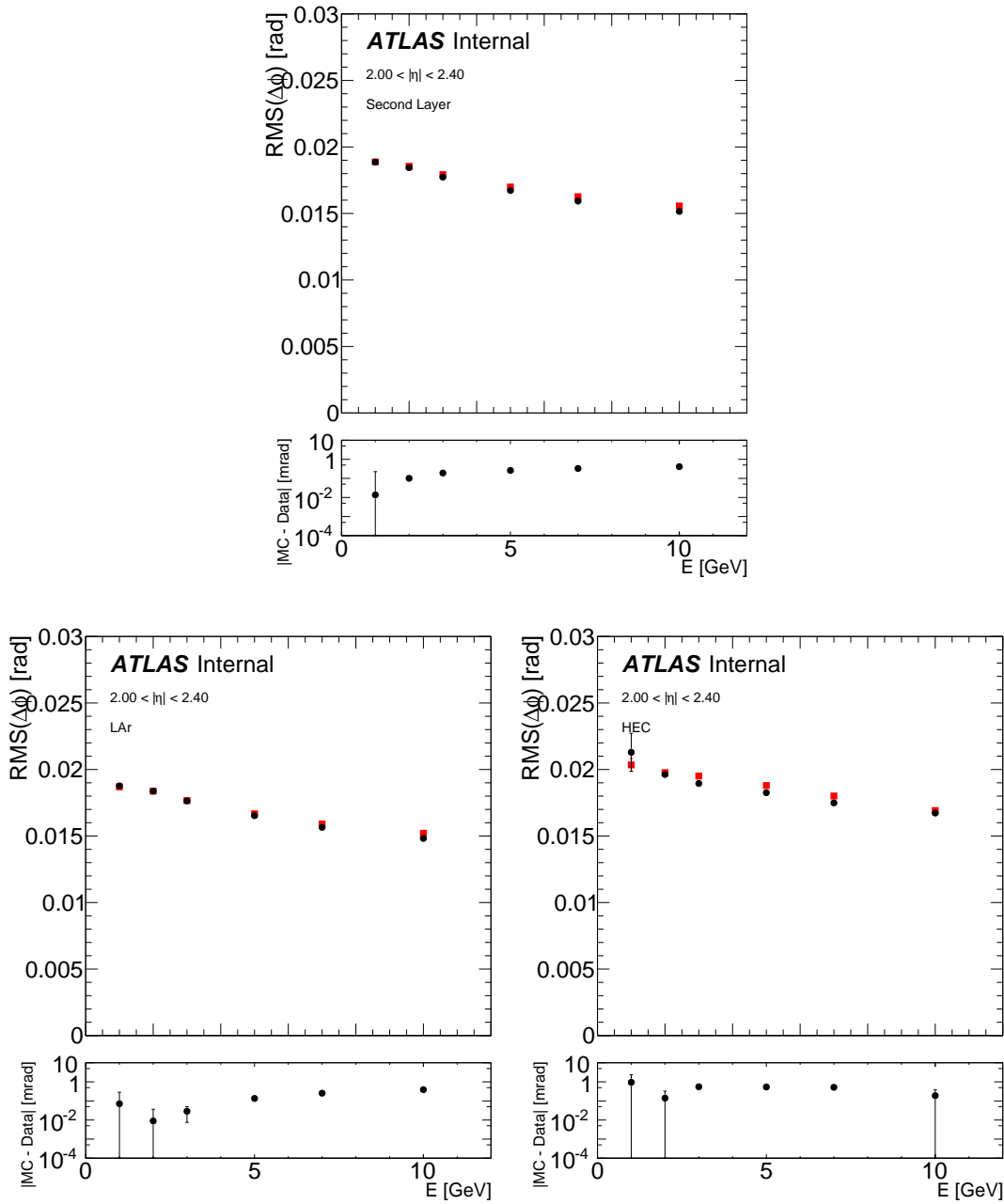


Figure 57: The differences between data and MC for the RMS of the  $\Delta\phi$  between isolated single particle tracks and clusters for various regions of the calorimeter in the endcap.

619 **Cluster Energy Scale** Using the most recent analysis in the 2012 E/p measurement [70], the data/MC  
 620 differences between the average ratio of the LCW cluster energy and the corresponding track momentum  
 621 is used to estimate the cluster energy scale (CES) uncertainty. The ratio between data and MC is bounded  
 622 by the following function

$$f_{\pm}(p|\alpha, \beta) = 1 \pm \alpha \times \left(1 + \frac{\beta \text{ MeV}}{p}\right),$$

623 where  $\alpha(\eta)$  and  $\beta(\eta)$  are two dimensionless  $\eta$ -dependent functions and  $p$  is the cluster momentum.  
 624 Figures 58, 59, 60, 61 show the estimated  $\alpha$  and  $\beta$  in six bins of  $\eta$ . To estimate the impact of the CES  
 625 uncertainty, the clusters inside the jet are scaled using the function  $f$ . Taking into account the correlations  
 626 between the CES uncertainty is non-trivial and so two approaches are used (and the more conservative is  
 627 retained):

- 628 1. For the ‘up’ (‘down’) uncertainty, multiply the four-vector of all clusters inside the jet by  $f_+(p|\alpha, \beta)$   
 629 ( $f_-(p|\alpha, \beta)$ ). The shift will be coherent for all clusters, but the actual scaling will change based  
 630 on  $p$  and  $\eta$ .
- 631 2. There is only one uncertainty: multiply the four-vector of each cluster by a random number with  
 632 mean one and standard deviation  $f_+(p|\alpha, \beta) - 1$ . Generate the random numbers for this procedure  
 633 in strips of  $\eta$  (with bin size half that of the E/p measurement bins) to allow for some coherence,  
 634 but still mostly emulating local fluctuations.

635 Note that the E/p measurement subtracts out the impact of neutral particles and so strictly speaking,  
 636 the numbers are relevant only for charged pion induced clusters. We apply the same CES uncertainty to  
 637 all clusters; if the CES uncertainty were to be dominant, this may need to be revisited.

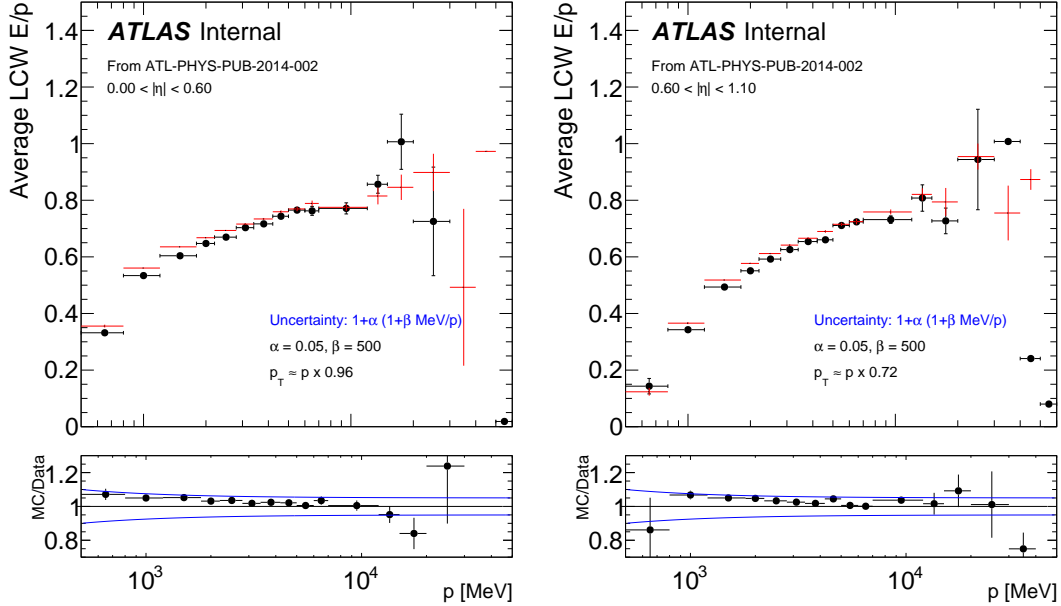


Figure 58: The average LCW E/p for  $0 < |\eta| < 0.6$  (left) and  $0.6 < |\eta| < 1.1$  (right), using the same analysis framework as in Ref. [70] (but LCW is not in the public note). The blue band in the ratio shows the estimated uncertainty used for the cluster energy scale uncertainty.

Not reviewed, for internal circulation only

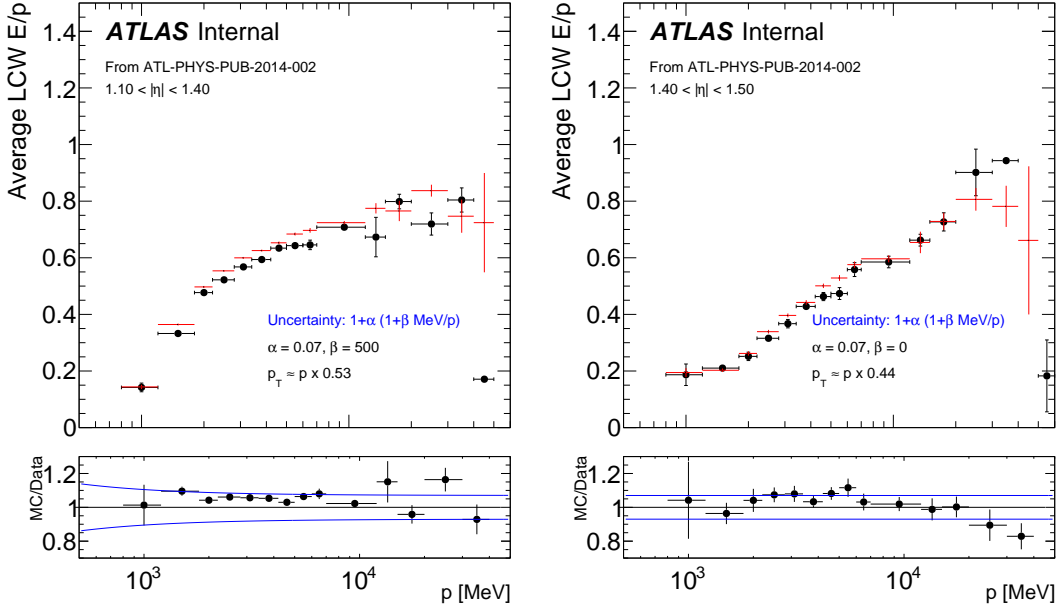


Figure 59: The average LCW E/p for  $1.1 < |\eta| < 1.4$  (left) and  $1.4 < |\eta| < 1.5$  (right), using the same analysis framework as in Ref. [70] (but LCW is not in the public note). The blue band in the ratio shows the estimated uncertainty used for the cluster energy scale uncertainty.

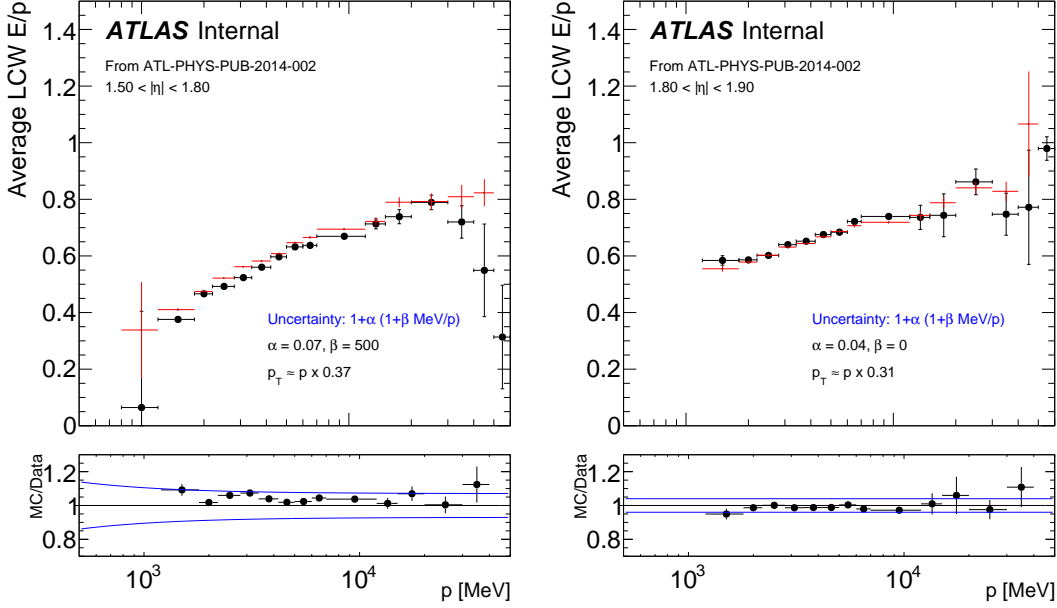


Figure 60: The average LCW E/p for  $1.5 < |\eta| < 1.8$  (left) and  $1.8 < |\eta| < 1.9$  (right), using the same analysis framework as in Ref. [70] (but LCW is not in the public note). The blue band in the ratio shows the estimated uncertainty used for the cluster energy scale uncertainty.

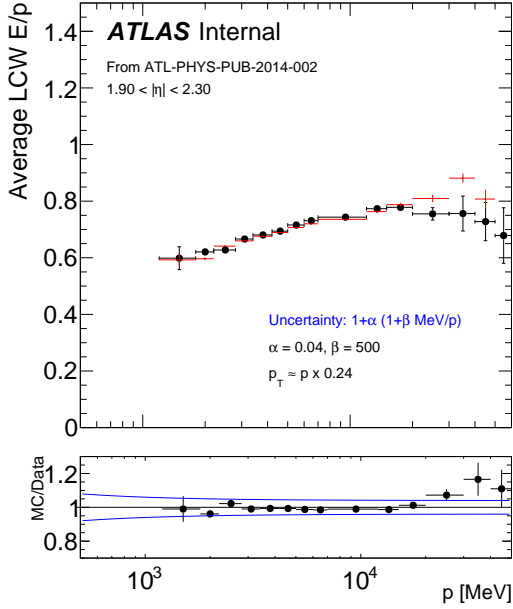


Figure 61: The average LCW  $E/p$  for  $1.9 < |\eta| < 2.3$ , using the same analysis framework as in Ref. [70] (but LCW is not in the public note). The blue band in the ratio shows the estimated uncertainty used for the cluster energy scale uncertainty.

638 **Cluster Energy Lost in Dead Material** Based on studies of single hadron response at  $\sqrt{s} = 900$  GeV,  
 639 clusters with energy below 2.5 GeV are randomly removed if an independently drawn random  
 640 number  $r \leq 25\% \times \exp(-2E/\text{GeV})$ , where  $E$  is the cluster energy.

641 **Luminosity uncertainty** An uncertainty of 2.8% on the integrated luminosity is assumed as per the  
 642 same methodology as that detailed in Ref [28,29], from a preliminary calibration of the luminosity  
 643 scale derived from beam-separation scans performed in November 2012. The only impact of  
 644 the luminosity uncertainty is the relative normalization of the multijets background to the other  
 645 backgrounds. There is no other contribution as we are measuring a shape and are not otherwise  
 646 sensitive to the overall normalization.

647 **Trigger Efficiency** To be determined in a standard way, expected to be very small and since this only  
 648 changes the acceptance, impacts **both** the track and calorimeter pull angle.

649 **Lepton Energy Scale and Resolution** To be determined in a standard way, expected to be very small  
 650 and since this only changes the acceptance, impacts **both** the track and calorimeter pull angle.

651 **MET Resolution** To be determined in a standard way , expected to be very small and since this only  
 652 changes the acceptance, impacts **both** the track and calorimeter pull angle.

653 ***b*-tagging** The flavour tagging CP group provides  $p_T$  dependance scale factor uncertainties that are  
 654 applied as event weights. Uncertainties are provided for the  $b$ ,  $c$  and light contributions separately.  
 655 We use the  $b$ -tagging CDI file 2014-Winter-8TeV-MC12-CDI.root and follow the  $b$ -tagging CP  
 656 group recommendations [71]. Impacts **both** the track and calorimeter pull angle.

657 **Unfolding Procedure** Then, the standard method for evaluating the systematic uncertainty from the  
 658 procedure is to re-weight the MC to the data and take the difference between the unfolded re-

659 weighted reconstructed MC to the re-weighted truth MC of the same generator. See [72, 73] for  
 660 more details of the method and Sec. 9.4.1 for the uncertainty in this analysis. Impacts **both** the  
 661 track and calorimeter pull angle.

### 662 8.1.1 Detector-level comparisons

663 Figure 62 shows comparisons between the charged and all particles pull angle distributions obtained  
 664 using the nominal PowHeg+PYTHIA monte carlo samples, and the samples obtained after making the  
 various smearings and scaling described above.

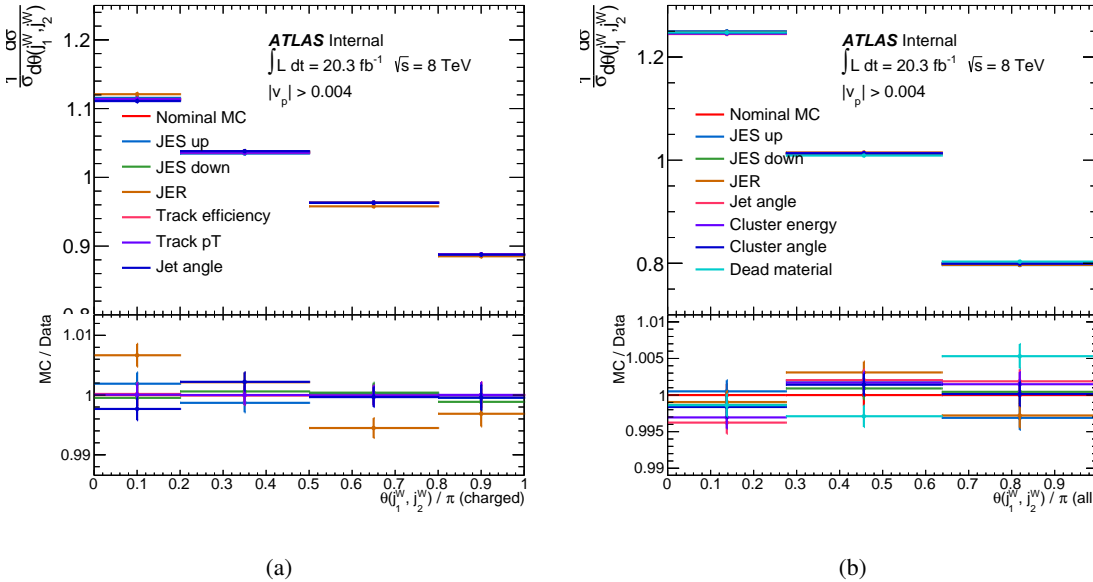


Figure 62: Detector level comparisons of (a) the charged particle and (b) the all particles pull angle distributions obtained after applying various sources of experimental systematic uncertainty.

665 In both cases all of the systematic uncertainties are small - less than 1% in every bin. For the charged  
 666 particle pull angle the jet energy scale produces the largest shift. The jet energy scale produces shifts  
 667 of less than 0.5%, and the track-based uncertainties are negligible. For the all particles pull angle the  
 668 uncertainty associated with the amount of dead material produces the largest shift. The jet energy scale  
 669 and resolution produce shifts of comparable size in the final bin, and the cluster-based uncertainties are  
 670 very small across the distribution.

672 The experimental uncertainties are propagated through the unfolding by repeating the entire unfold-  
 673 ing procedure using a response matrix derived using the smeared and scaled MC events. The results are  
 674 shown in Section 9.4.

## 675 8.2 Theoretical Uncertainties

676 Theory uncertainties will impact both the unfolded distribution and the predictions for the truth distribu-  
 677 tions that are compared with the unfolded data.

678 **PDF** : To be determined in a standard way , expected to be very small and since this only changes the  
 679 acceptance, impacts **both** the track and calorimeter pull angle.

680 **Shower Model** : Compare Pythia and Herwig showering for a fixed hard scatter generator. Since truth  
 681 level studies show that the pull angle is largely independent of the hard scatter generator, it will suf-  
 682 fice to compare the two full detector simulation samples (Powheg+Pythia and MC@NLO+Herwig)  
 683 for the uncertainty due to the response matrix and then on the unfolded distribution, we can fix  
 684 Powheg and compare the differences in Pythia versus Herwig and also fix Herwig and compare the  
 685 differences in Powheg and MC@NLO (expected to be very small). Figure 63 shows the truth pull  
 686 distributions for various shower models. As stated, the difference between Powheg and MC@NLO  
 687 for fixed Herwig is small, but there is a significant difference between Herwig and Pythia. Impacts  
 688 **both** the track and calorimeter pull angle.

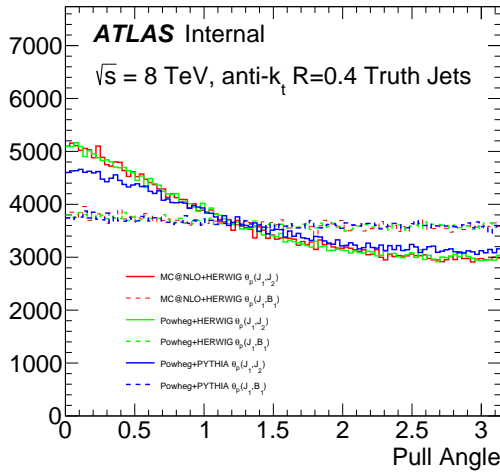


Figure 63: Truth level distributions comparing Pythia and Herwig.

689 **Color Reconnection** : While the color reconnection in the parton shower is also due to the exchange of  
 690 color charge, it is expected to not have a large impact on the jet pull distribution as the pull vector  
 691 should be set by the color flow at the hard scatter. This is supported by studies in the 2012 BOOST  
 692 report [47] and also first studies in ATLAS using the low CR Perugia tune. Figure 64 compares  
 693 the nominal PYTHIA tune (P2011C) with the 2012 Perugia lowCR tune [45] (as well as a tune for  
 694 higher MPI). The lowCR Perugia tune differs from the nominal tune in the method and strength for  
 695 calculating the reconnection probability for colored partons in the PS. The two parameters which  
 696 differ are MSTP(95) (probability calculation method) and MSTP(78) (strength of the connection).  
 697 In the lowCR tune, the probability for a string piece to preserve its original connection is given by

$$P_{\text{keep}} = (1 - \zeta \times \text{MSTP}(78))^{n_{\text{int}}},$$

698 where  $n_{\text{int}}$  is the number of parton-parton interactions in the current event. The parameter  $\zeta^{-1} =$   
 699  $1 + \text{MSTP}(77)^2 \times \langle p_T \rangle^2$  is a way to make this  $p_T$  dependent. In all the Perugia tunes,  $\text{MSTP}(77)=1$ .  
 700 The probability in the nominal tune is given by

$$P_{\text{keep}} = (1 - \zeta \times \text{MSTP}(78))^{\langle n_s \rangle(y_1, y_2)},$$

701 where this tries to be more ‘local’ with the function  $\langle n_s \rangle(y_1, y_2)$  that counts the number of string  
 702 pieces (not counting the ones under consideration) between the rapidity endpoints of the piece

under consideration  $y_1$  and  $y_2$ . The loCR tune is set to be just barely consistent with the minimum bias data, with as low a CR setup as possible. There is also a Perugia tune for noCR, which sets  $P_{\text{keep}} = 1$  and is in bad agreement with several data distributions. This sample exists at the evgen level in the ATLAS simulation.

Figure 64 shows that the impact from varying the CR tune is very small at truth level,  $\lesssim 1\%$ . This small change cannot be explained by kinematics (various kinematic re-weighting procedures have been studied). The impact on the unfolding will be negligible, as the change at truth level will also be reflected at reco level and thus the impact on the response matrix will be less than the impact on the truth distribution, which is already small. However, the  $\lesssim 1\%$  is not small in absolute sense compared to the truth level distributions we are trying to probe (the pull angle deviates from uniform only at the 10% level). Thus, we add the truth variations from the CR tune as part of an uncertainty band on the predicted truth level distributions in the unfolding (both for the nominal and the color flipped samples, for which the same relative difference on the nominal is applied<sup>12</sup>). As a cross-check that the impact on the unfolding is negligible, we perform the unfolding using AFII response matrices and compare to the nominal AFII-unfolded result (the CR tune is not simulated using fastsim).

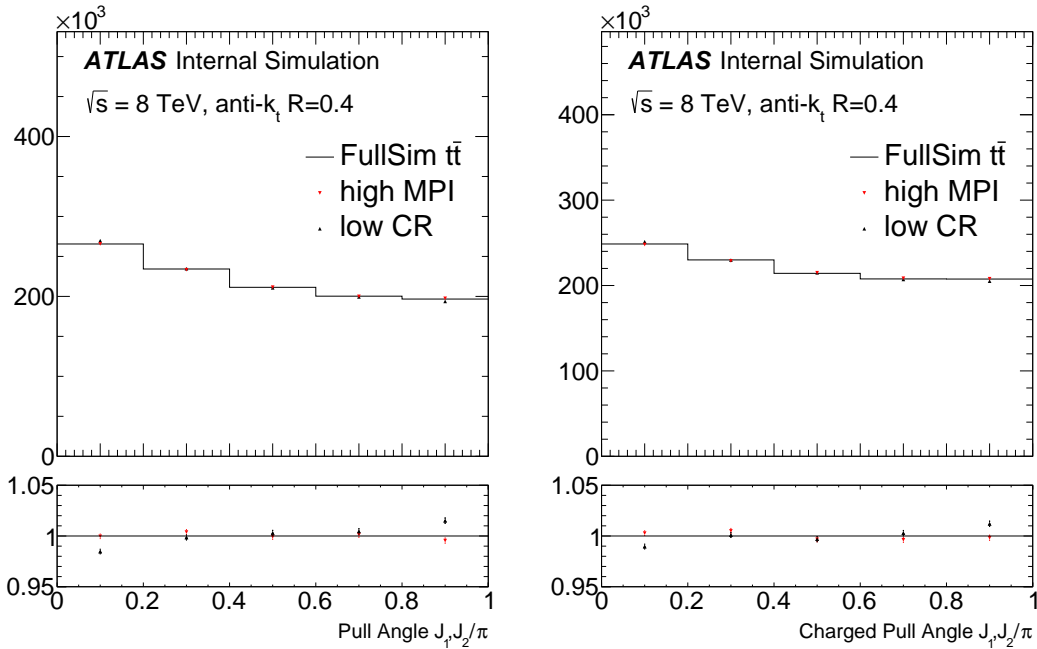


Figure 64: Truth level distributions comparing the nominal and low CR tunes of Pythia.

**Renormalization and factorization scales** : To estimate the impact of the fixed order calculations involved in the  $t\bar{t}$  prediction, the renormalization and factorization scales are varied in the usual way ( $\times 2$  and  $\times 0.5$ ) from their nominal values. Figure 66 shows the pull angle distribution for the various scale variations and as expected, the impact on the pull angle distribution is minor, about 1% in the most sensitive region at small pull angle. These samples only exist as EVGEN and so the same procedure (except for the cross-check) stipulated for the CR systematic is applied here.

<sup>12</sup>We have checked that the truth-level impact of the CR is at the same level as for the nominal  $t\bar{t}$  in Fig. 65 by using the ATLAS production system to privately generate samples of 20k events of flipped + nominal Pythia tune and flipped + low CR Pythia tune.

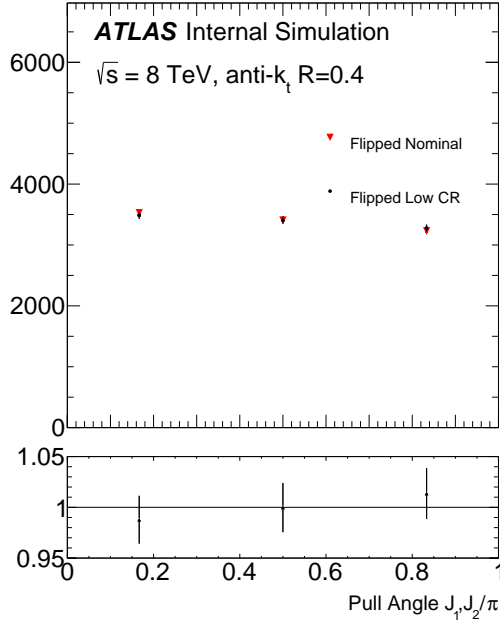


Figure 65: Truth level distributions comparing the nominal and low CR tunes of Pythia for the color-flipped sample. The samples used to generate these plots were produced with the ATLAS MC production system privately over 20k events. The flipped nominal is the usual flipped MC with the standard Pythia shower while the flipped CR uses the same low CR Pythia tune as is used to evaluate the systematic uncertainty in  $t\bar{t}$ . The same Powheg events are used for both variations, so the error bars are over-estimated (samples are partially correlated).

725 **ISR/FSR** : Figure 67 shows the impact on the pull angle distribution due to variations in the ISR/FSR  
 726 modeling. Note that these samples use AcerMC for the matrix element and not Powheg. The  
 727 ISR/FSR could impact the pull angle either directly by introducing more radiation around the two  
 728 selected jets or indirectly by changing the event kinematics or by changing the number of jets in  
 729 the event (and thus impact the combinatorics of which jets are selected). After re-weighting the  
 730  $\Delta R$  and leading jet  $p_T$  for the samples<sup>13</sup>, Fig. 68 (all particles pull) and Fig. 69 (charged particle  
 731 pull) show that like the other generator systematic uncertainties considered so far, the impact is at  
 732 the  $\lesssim 1\%$  level. Therefore, they are treated in the same way as for the CR/MPI uncertainties.

733 **Top Quark Mass** : Powheg MC samples with various top quark masses (165, 170, 175 and 180 GeV)  
 734 have been generated and simulated with the full detector simulation. The impact from changing  
 735 the top quark mass is a change in kinematics which affects the pull angle indirectly due to changes  
 736 in acceptance and also indirectly since the color flow depends on kinematics. This is studied by  
 737 varying the response matrix and investigating the impact on the unfolded result. The variation is  
 738 also included in the uncertainty band on the truth level predictions (see Fig. 70).

739 **Color Flow Model** : The color inverted sample with the same matrix element generator and shower +  
 740 hadronization model is used to study the impact on the response matrix. Since all relevant samples  
 741 are produced with a full detector simulation, one can determine this systematic uncertainty directly

<sup>13</sup>This does remove a possible impact on the pull angle, but also normalizes some of the differences between Powheg and AcerMC. Since the ratio between more/less ISR/FSR marginally changed, the re-weighting most likely had little impact on the former.

Not reviewed, for internal circulation only

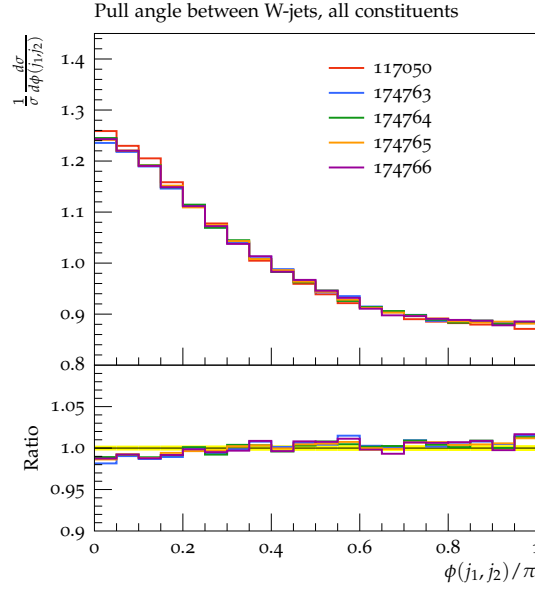


Figure 66: The truth pull angle distribution for various scale variations of the  $t\bar{t}$  MC. 174763 has 2× the renormalization scale, 174764 has half the nominal renormalization scale, 174765 has twice the renormalization scale and 174766 has half the renormalization scale. The 117050 is the nominal  $t\bar{t}$  sample.

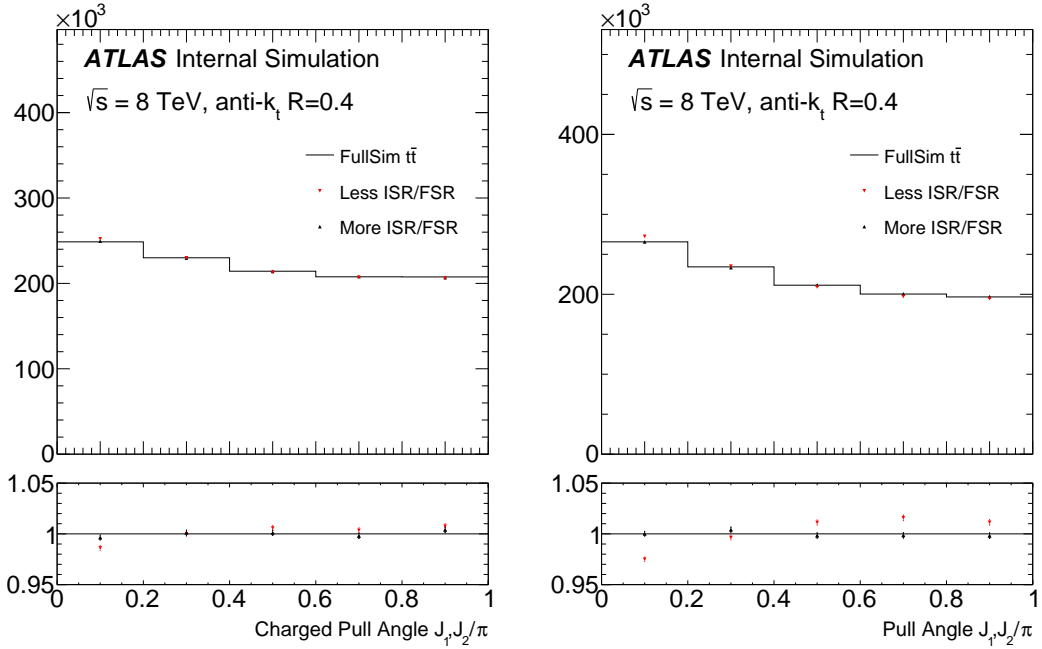


Figure 67: Truth level distributions comparing the nominal with various ISR/FSR settings (using AcerMC).

742  
743

by determining the change in the unfolded result by using a different MC to determine the response matrix.

Not reviewed, for internal circulation only

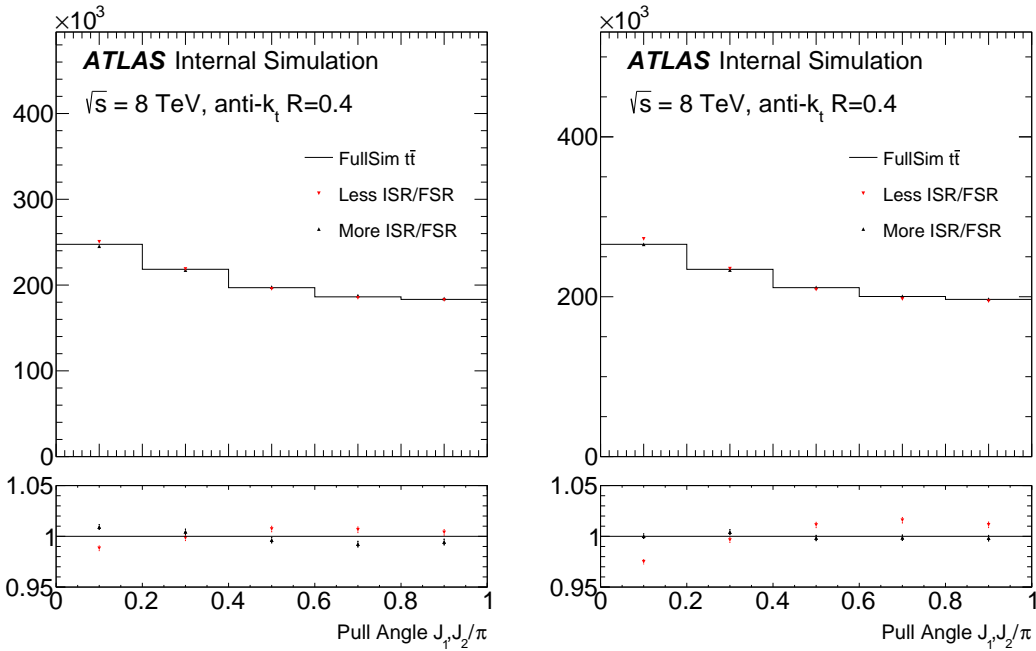


Figure 68: The ISR/FSR variations before re-weighting and after re-weighting the  $\Delta R$  and leading jet  $p_T$  distributions.

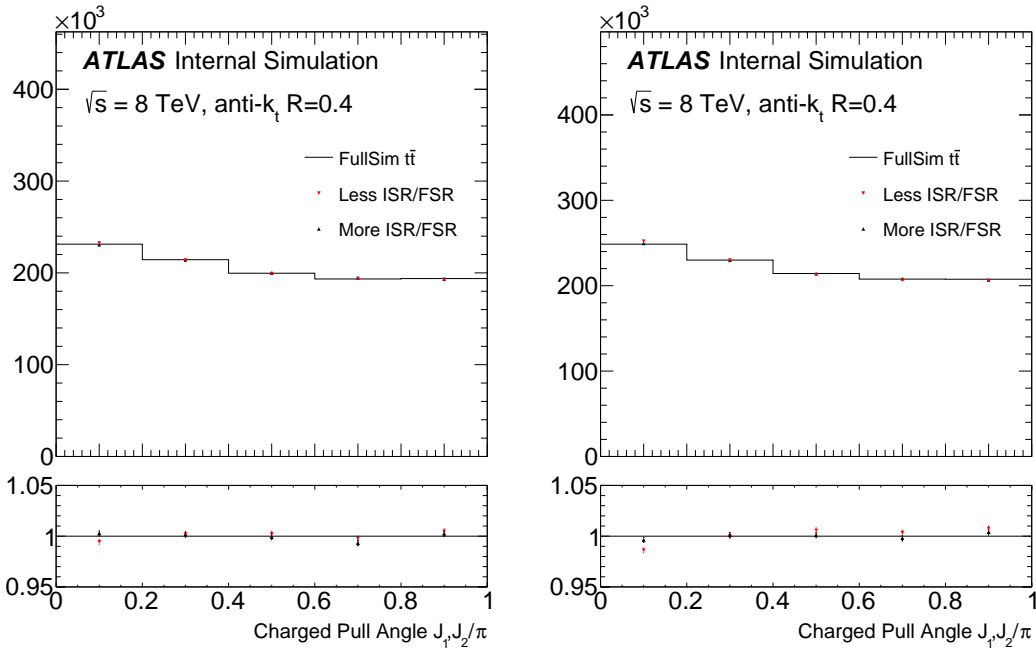


Figure 69: The ISR/FSR variations before re-weighting and after re-weighting the  $\Delta R$  and leading jet  $p_T$  distributions.

744 **Background Normalization** : In the background subtraction, we vary the  $W+jets$  normalization factors  
 745 from the uncertainties in the charge asymmetry method uncertainties.

Not reviewed, for internal circulation only

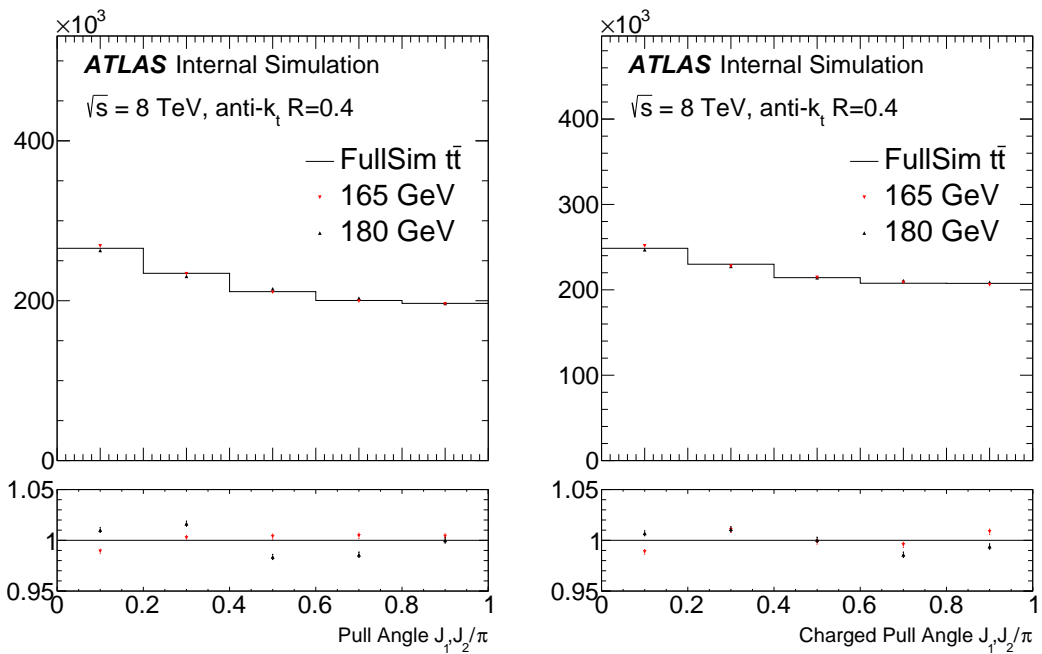


Figure 70: Extreme top quark mass variations for the all particles (left) and charged particles (right) pull angles.

## 746 9 Results

### 747 9.1 Unfolding

748 The goal of unfolding is to correct the measured data for effects arising from the finite efficiency, ac-  
 749 ceptance and resolution of the detector. In this analysis an iterative Bayesian unfolding technique was  
 750 chosen to correct the data, the details of which will be given in what follows.

751 By treating each bin of a histogram as an element in a vector or matrix, we can write

$$\mathbf{A} \cdot \mathbf{x} = \mathbf{y} \quad (8)$$

752 where  $\mathbf{x}$  is the true distribution we are interested in,  $\mathbf{y}$  is the distribution we measure and  $\mathbf{A}$  is a matrix  
 753 – often the “response”, “smearing” or “transfer” matrix – which encodes information about the detector  
 754 and transforms the distributions from true to measured.

755 After writing the problem as in equation (8), it is tempting to think that the solution is simply to invert  
 756 the matrix  $\mathbf{A}$  and apply it to our measured distribution  $\mathbf{y}$ . However, it is argued by D’Agostini [74] that  
 757 since the problem of unfolding is inherently a probabilistic one, we should use probabilistic methods to  
 758 solve it.

759 The problem can be reformulated by writing the *probability* for finding an event in bin  $i$  of the true  
 760 distribution,  $d'_i$ , as

$$d'_i = \sum_j P(T_i|M_j) d_j = \sum_j \theta_{ij} d_j \quad (9)$$

761 where  $P(T_i|M_j)$  is an element of the ‘unfolding matrix’  $\theta_{ij}$  and gives us the probability for finding an  
 762 event in bin  $i$  of the true distribution, given that we measured one in bin  $j$ .  $d_j$  is the probability for  
 763 finding an event in bin  $j$  of the measured distribution.

764 Using Bayes’ theorem it is possible to rewrite the unfolding matrix as

$$\theta_{ij} = P(T_i|M_j) = \frac{P(M_j|T_i) \cdot P(T_i)}{\sum_i P(M_j|T_i) \cdot P(T_i)} = \frac{a_{ji} \cdot P(T_i)}{\sum_i a_{ji} \cdot P(T_i)}, \quad (10)$$

765 where  $P(M_j|T_i) = a_{ji}$  are elements of the response matrix introduced in equation (8), and  $P(T_i)$  is the  
 766 probability of finding an event in bin  $i$  of the true distribution. This is often referred to as the prior  
 767 probability distribution and is typically taken to be the particle-level distribution produced by the MC.

768 We are now able to tackle the problem of unfolding, since we can construct the response matrix from  
 769 our Monte Carlo events. If we generate a large number of events in each bin  $T_i$  we can observe which  
 770 bins they fall in after being passed through a simulation of the detector. This information can then be  
 771 used, with equations (10) and (9), to attempt to recover the shape of the true distribution.

772 One potential drawback of Bayesian unfolding is the biasing of the result by the prior probability  
 773 distribution. The problem can be somewhat avoided by applying the full unfolding procedure to the data  
 774 distribution iteratively, and using the output of each round of unfolding as the input to the next. The  
 775 elements of the unfolding matrix then become

$$\theta_{ij}^n = \frac{a_{ji} \cdot P(d'_{i,n-1})}{\sum_i a_{ji} \cdot P(d'_{i,n-1})} \quad ; \quad n \geq 1 \quad ; \quad d'_{i,0} := T_i \quad (11)$$

776 where  $d'_{i,n-1}$  is the probability of finding an event in bin  $i$  of the true distribution after  $n - 1$  iterations  
 777 of the unfolding, and other symbols are as defined in equations (10) and (9). As already mentioned the  
 778 initial prior distribution,  $d'_{i,0}$  is taken to be the MC particle-level distribution,  $T_i$ .

779 The probability of finding an event in bin  $i$  of the true distribution after  $n$  iterations of unfolding,  $d_{i,n}$   
 780 is then given by

$$d'_{i,n} = \sum_j \theta_{ij}^n \cdot d_j \quad (12)$$

781 As the number of iterations increases, the bias from the Monte Carlo particle-level distribution de-  
 782 creases. However, at the same time, statistical fluctuations are amplified and the statistical uncertainty  
 783 is increased. Therefore a reasonable number of iterations must be used to balance the decreasing bias  
 784 against the increasing uncertainty. The number of iterations is therefore usually kept small.

785 The iterative Bayesian unfolding procedure used in this analysis is implemented in the **EWUnfolding**  
 786 package. Originally written by members of the ATLAS Standard Model W/Z and Electroweak groups,  
 787 the package is essentially a wrapper to **RooUnfold** [75] with added functionality for assessing statistical  
 788 and systematic uncertainties in a consistent way. A description and discussion of the unfolding procedure  
 789 implemented in the **EWUnfolding** package can be found in [76], but we repeat it here for completeness.

790 Unfolding begins by defining the following quantities:

- 791 • **d** – the original data distribution with n bins. The value of the distribution in bin  $i$  is labelled  $d_i$ .
- 792 • **b** – the distribution of expected background events with n bins. The value of the background  
 793 distribution in bin  $i$  is  $b_i$ .
- 794 • **y** – the signal distribution with n bins. The value of the signal distribution in bin  $i$  is  $y_i$ .
- 795 • **x** – the unfolded distribution with n bins. The value of the unfolded distribution in bin  $i$  is  $x_i$ .

796 The following quantities are also defined:

- 797 • The response matrix, **A**, is used to correct for bin-to-bin migrations between the reconstructed and  
 798 truth-level distributions. It is defined, and filled with, *only* events which pass the event selection,  
 799 and fall into the required fiducial volume at truth *and* reconstructed level.
- 800 • Fiducial factors:  $f_i = \frac{N_i^{\text{truth} \wedge \text{reco}}}{N_i^{\text{reco}}}$ , for each bin of the *reconstructed* distribution, which corrects for  
 801 reconstructed-level events which did not fall into the fiducial region defined at truth-level and thus  
 802 have no associated truth-value which can be used during the unfolding. Note that bin  $i$  here is  
 803 defined by the *reconstructed-level* value of the variable.
- 804 • Correction factors:  $c_i = \frac{N_i^{\text{reco} \wedge \text{truth}}}{N_i^{\text{truth}}}$ , for each bin of the unfolded distribution, which account for  
 805 efficiency and acceptance losses on going from truth to reco. Note that bin  $i$  is defined here by the  
 806 *truth-level* value of the variable.

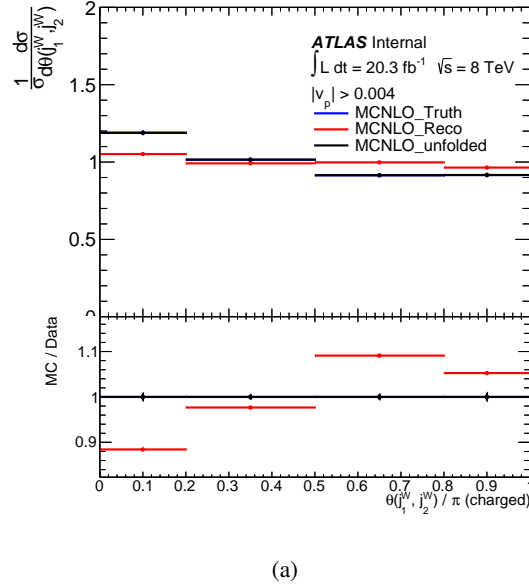
807 With these quantities in hand, we can construct the values of the signal and unfolded distributions as  
 808 follows:

$$\begin{aligned} y_i &= (d_i - b_i) \cdot f_i \\ x_i &= (\boldsymbol{\theta} \cdot \mathbf{y})_i / c_i \end{aligned} \tag{13}$$

809 where  $\boldsymbol{\theta}$  is the unfolding matrix, constructed from the response matrix, **A**, and prior as in equation (10).

## 810 9.2 Unfolding Checks

811 The simplest check to perform is a check of the technical implementation of the unfolding code. This  
 812 can be done by unfolding a reco-level MC distribution, using events from the same MC sample to fill the  
 813 response matrix. For example, after using MC@NLO events to fill the response matrix and define the other  
 814 necessary correction factors, unfolding a reco-level distribution from MC@NLO should produce exactly  
 815 the truth-level distribution. An example of this check is shown in Figure 71, where the reco-level pull  
 816 angle distribution produced by MC@NLO has been unfolded using the same MC@NLO events in unfolding  
 817 procedure. The unfolded distribution matches the truth-level distribution exactly, as expected.



(a)

Figure 71: Reco-level (red) pull-angle distribution from MC@NLO unfolded using the same MC events in the unfolding procedure. The unfolded distribution (black) matches the truth-level distribution (blue) exactly.

### 9.2.1 Number of Iterations

We have studied how the unfolded results change as a function of the regularization parameter (which for iterative Bayesian unfolding is the number of iterations). Figure 72 shows the value of the unfolded value in each of the four bins of the pull angle when unfolding Powheg with MC@NLO. After a certain number of iterations, the results saturate. The point of saturation depends on the scale of the resolution, as indicated by a toy study shown in Fig. 73 in which a uniform distribution (truth) + Gaussian is unfolded (the pull angle has  $\sigma/\text{Range} \sim 0.3$ ). One does not necessarily want to use the number of iterations corresponding to the saturation point; the bias might be smaller with a smaller number of iterations.

The optimal number of iterations was studied further by investigating how the size of uncertainties that assess the bias associated with the unfolding chance with increasing numbers of iterations.

The uncertainty associated with the color model, discussed below, is estimated by unfolding the data using the nominal PowHeg+PYTHIA and the color-flipped MC samples and comparing the results. Figure 74 shows the ratio between the pull angle distributions unfolded using the two sets of MC samples, and using different numbers of iterations in the Bayesian unfolding. These ratios are used to define the uncertainty, and it can be seen that the uncertainty decreases with increasing numbers of iterations. The all particles pull angle distribution (Figure 74(a)) has the larger color model uncertainty and it can be seen that the uncertainty can be reduced from around 10% when just 2 iterations are used, to around 3% when 20 iterations are used.

The unfolding non-closure uncertainty is explained in detail in Section 9.4.1 and is estimated by looking at the ratios shown in Figure 75. In this case the uncertainty increases with increasing numbers of iterations used in the unfolding, and the increase in non-closure uncertainty must be balanced against the decrease in color model uncertainty.

The final uncertainty that must be considered when studying numbers of iterations is the statistical uncertainty. The uncertainty bars in Figures 74 and 75 show the size of the statistical uncertainty, which increases with increasing numbers of iterations.

Tables 6 and 7 show approximate values of the three previously mentioned uncertainties for several

Not reviewed, for internal circulation only

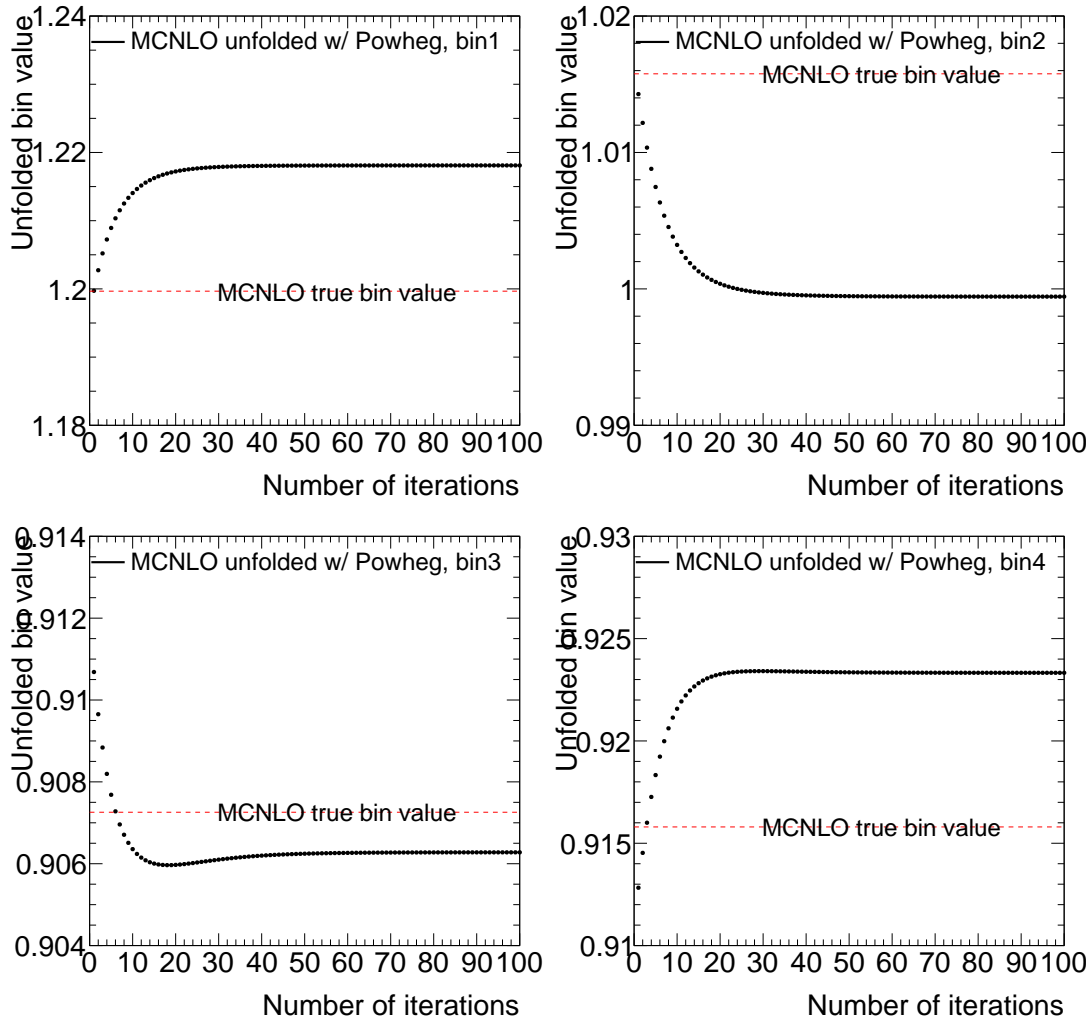


Figure 72: An illustration of the unfolded results as a function of the number of iterations with the iterative Bayesian unfolding technique.

<sup>844</sup> choices of the number of iterations used in the unfolding. After summing the uncertainties in quadrature it  
<sup>845</sup> is clear that for the all particles pull angle 15 iterations would be optimal, while for the charged particles pull angle 4 iterations produces the smallest combined uncertainty.

$N_{\text{iterations}}$	Stats.(%)	Non-closure(%)	Color model(%)	Sum in quad.(%)
4	1.0	2.0	7.0	7.3
7	1.5	2.8	5.0	5.9
10	1.8	3.2	4.0	5.4
<b>15</b>	<b>2.0</b>	<b>3.8</b>	<b>3.3</b>	<b>5.2</b>
20	2.3	4.1	3.0	5.6

Table 6: Approximate size of uncertainties on the all particles pull angle distribution as a function of the number of iterations used in the unfolding.

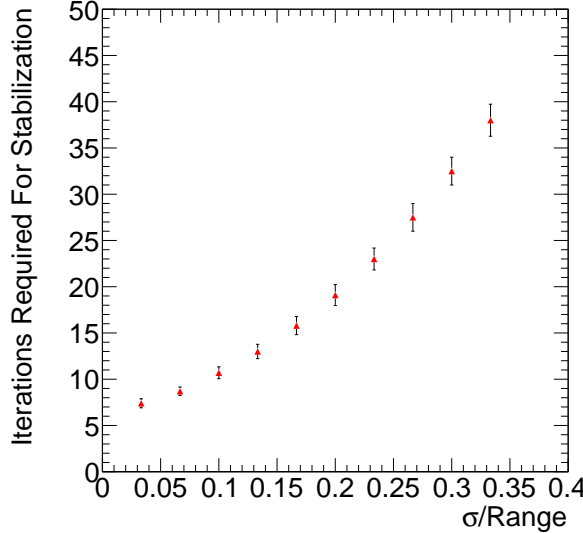


Figure 73: The number of iterations required for the unfolded results to saturate. The ‘data’ is a toy model of a uniform distribution (truth) with Gaussian noise.

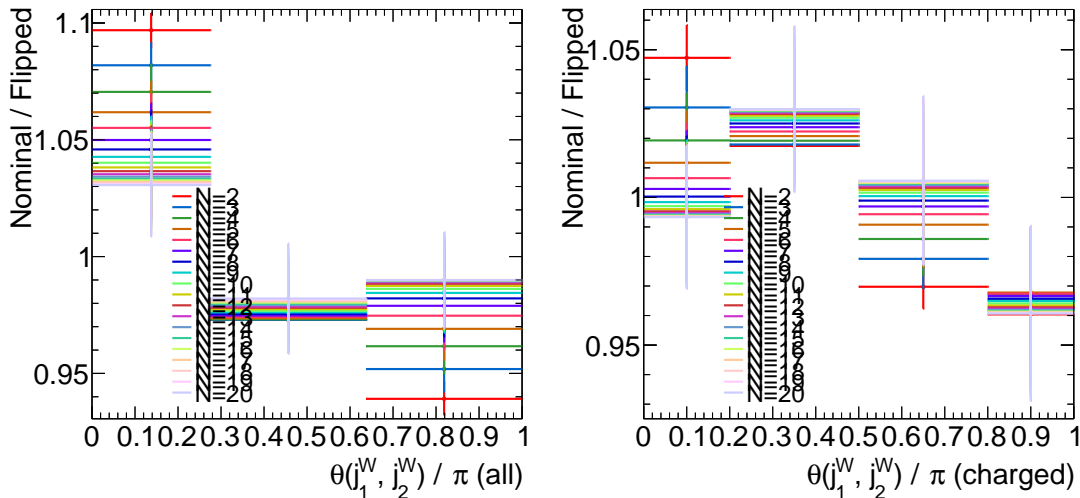


Figure 74: Ratios of pull angle distributions unfolded with PowHeg+PYTHIA and color-flipped MC samples, using different numbers of iterations.

### 847 9.2.2 Statistical Pull

848 Figure 76 shows the statistical pull for the charged pull angle. The statistical pull for a particular pseudo-  
 849 experiment  $j$  and for a particular bin  $i$  is defined as  $(x_{ij} - \bar{x}_i)/\sigma_{ij}$ , where  $x_{ij}$  is the value determined  
 850 from the unfolding,  $\bar{x}_i$  is the average value over the ensemble and  $\sigma_{ij}$  is the statistical uncertainty deter-  
 851 mined from our unfolding procedure. The set of pseudo-experiments are generated by bootstrapping the  
 852 data. Figure 76 shows that since the RMS values for the pull distributions are consistent with unity, the  
 853 uncertainties are correctly estimated.

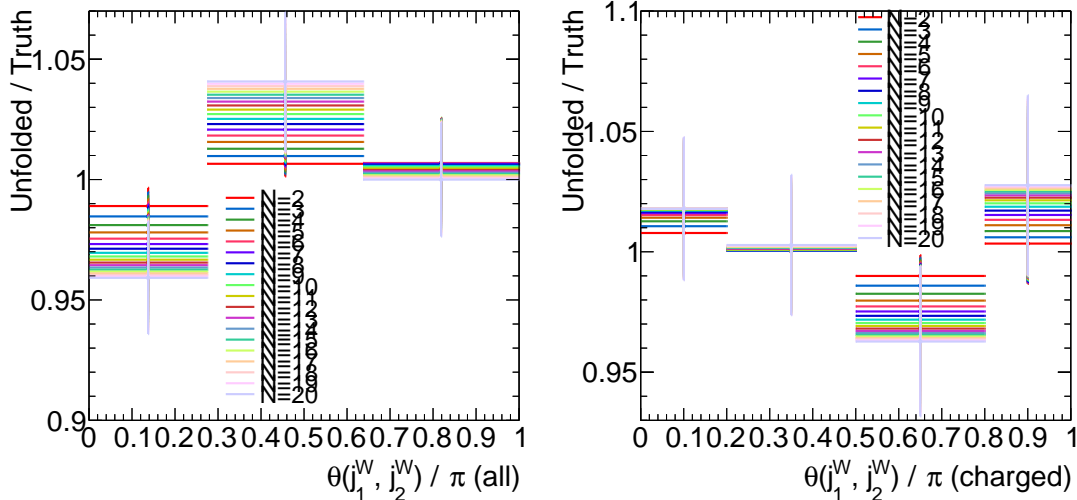


Figure 75: Non-closure uncertainty on the all particles (a) and charged particles (b) pull angle distributions, evaluated when different numbers of iterations are used in the Bayesian unfolding.

$N_{\text{iterations}}$	Stats.(%)	Non-closure(%)	Color model(%)	Sum in quad.(%)
4	1.5	1.8	2.0	3.1
7	2.0	2.5	2.5	4.1
10	2.3	3.0	2.8	4.7
15	2.5	3.5	3.0	5.2
20	2.5	3.8	3.0	5.4

Table 7: Approximate size of uncertainties on the charged particles pull angle distribution as a function of the number of iterations used in the unfolding.

### 854 9.3 Cross-checks and closure tests

855 In Figure 77 the MC@NLO reco-level pull angle distributions have been unfolded using a response matrix  
 856 created using events from PowHeg+PYTHIA. When comparing the unfolded reco-level distributions with  
 857 the MC@NLO truth-level distributions it can be seen that PowHeg+PYTHIA does a reasonable job. The  
 858 unfold distribution looks much more like the the truth-level distribution than the original reco-level one,  
 859 although there is some residual difference between the MC@NLO unfolded and truth-level disitrbutions  
 860 which is currently under investigation.

861 Figure 78 shows the comparisions of pull angle distributions in data after unfolding using either  
 862 MC@NLO or PowHeg+PYTHIA MC events to define the response matrix and other correction factors.

863 Figure 79 shows the results of unfolding the charged particles pull angle distribution using to different  
 864 methods; the nominal iterative Bayesian technique using four iterations, and the SVD technique with a  
 865 regularisation parameter of three. The two results are approximately identical, and give us confidence  
 866 that our default unfolding technique is a reasonable one.

### 867 9.4 Systematic uncertainties

868 The various sources of experimental systematic uncertainty are propagated through the unfolding ma-  
 869 chinery by deriving new response matrices using the MC events in which the kinematics of the relevant  
 870 physics objects have been smeared or shifted by the appropriate amounts. The complete unfolding pro-

Not reviewed, for internal circulation only

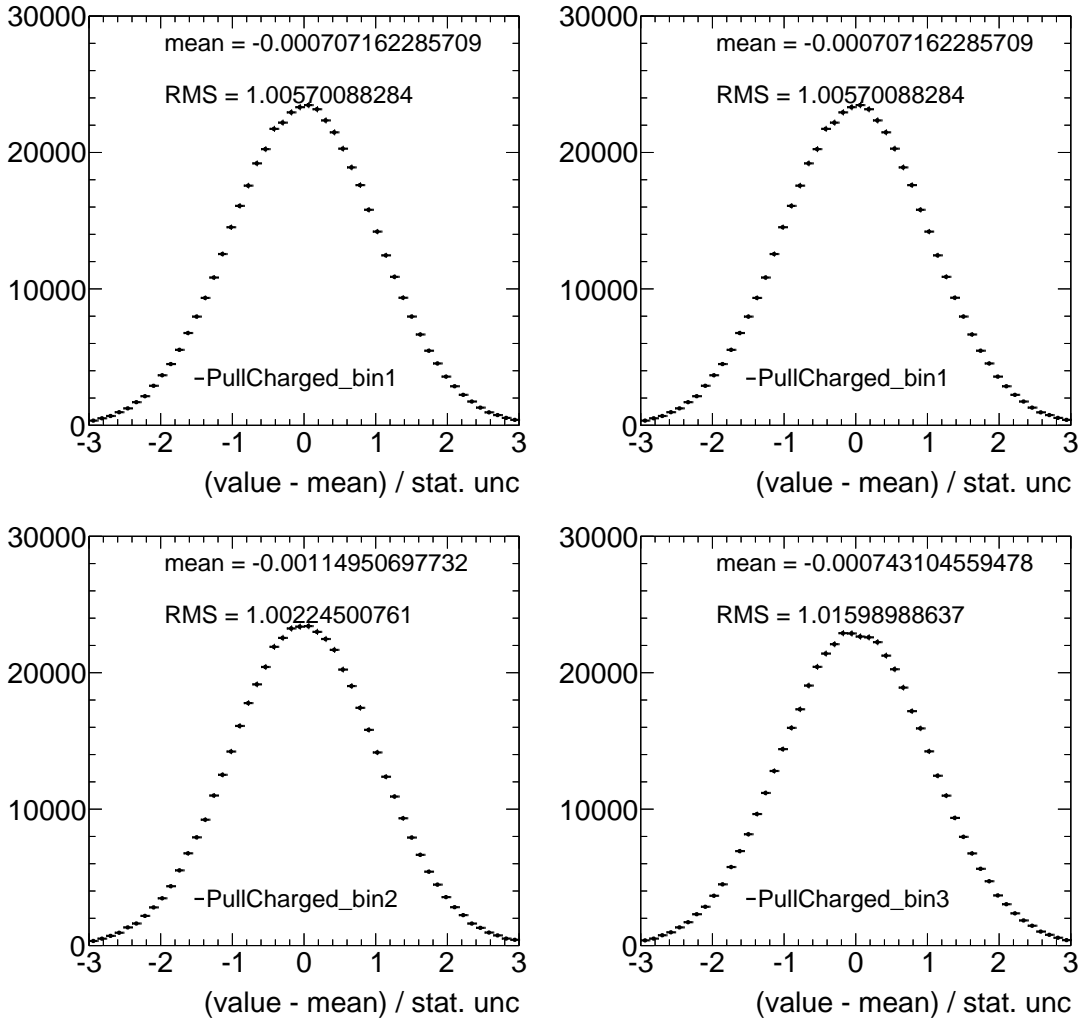


Figure 76: The statistical pull for the four bins of the charged pull angle.

871 cedure is repeated using the new response matrices, and the results are compared to the unfolded result  
 872 obtained using the nominal (PowHeg+PYTHIA) MC sample. Any differences are assigned as the corre-  
 873 sponding uncertainty.

#### 874 9.4.1 Unfolding non-closure

875 Following the guidelines outlines on the ATLAS Standard Model group's TWiki page [73], an uncertainty  
 876 due to the non-closure of the unfolding technique is estimated by first comparing the shapes of the *reco-*  
 877 *level* signal monte carlo with the data. Figure 80 shows the ratio of the charged particles pull angle  
 878 distribution in data compared to the PowHeg+PYTHIA  $t\bar{t}$  prediction. The ratio is fitted with a second-order  
 879 polynomial (shown in red), which is used to define a reweighting function. An equivalent reweighting  
 880 function is defined for the all particles pull angle. The reweighting function is then used to reweight the  
 881 reco-level PowHeg+PYTHIA  $t\bar{t}$  events. After the reweighting the data and reco-level MC agreement is  
 882 much improved, as shown in Figure 81.

883 The reweighted reco-level distribution in MC is then unfolded using the nominal PowHeg+PYTHIA  
 884 MC sample, and the unfolded result is compared to the corresponding reweighted truth-level distribution.

Not reviewed, for internal circulation only

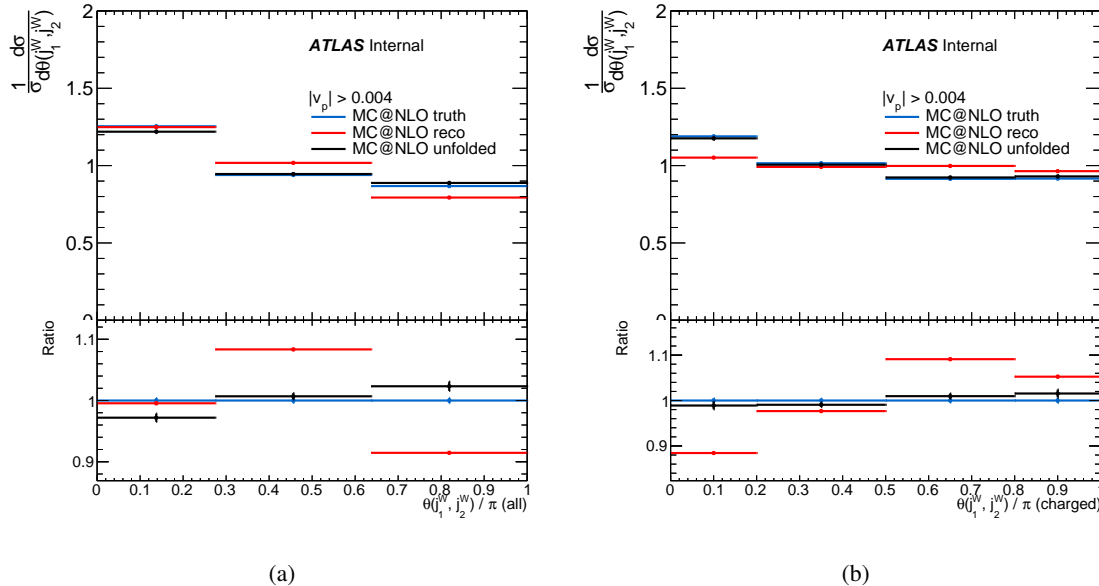


Figure 77: Pull angle distributions calculated with all (a) and charged (b) jet constituents, using recoil-level MC@NLO events (red) that have been unfolded (black) using PowHeg+PYTHIA to create the response matrix and other correction factors. Corresponding truth-level pull-angle distributions from MC@NLO are shown in blue.

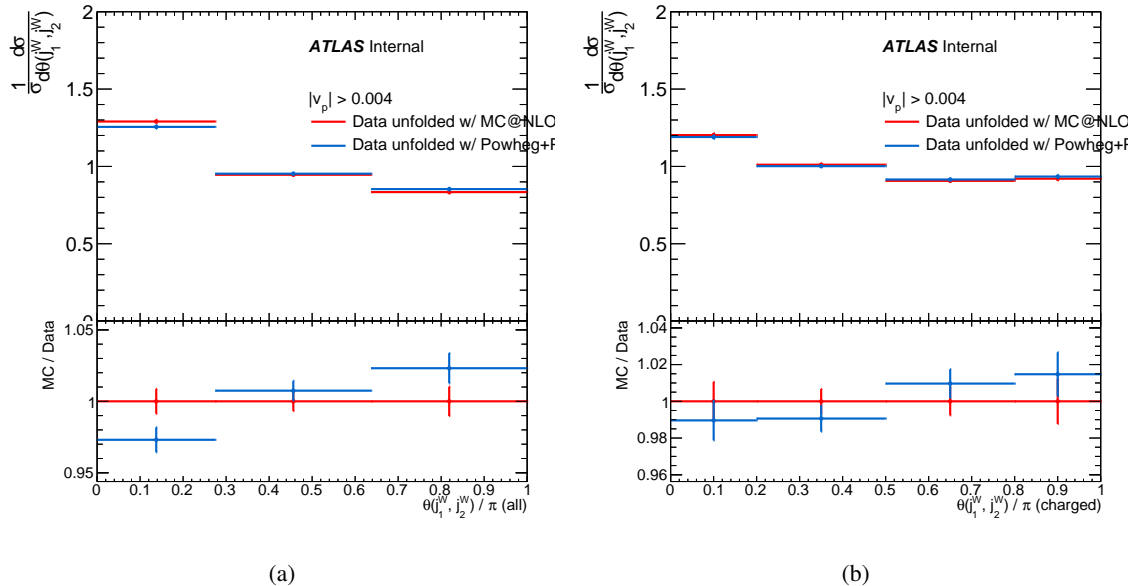
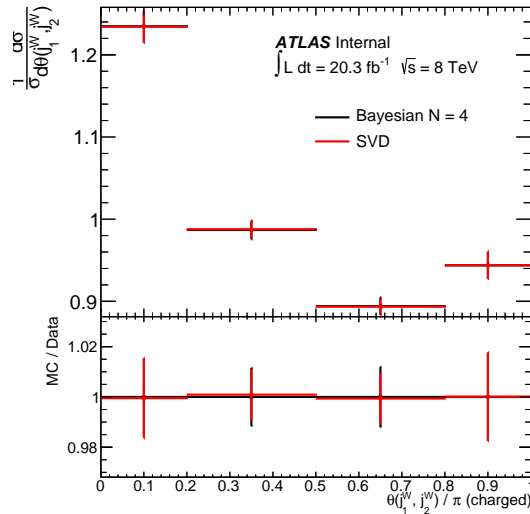


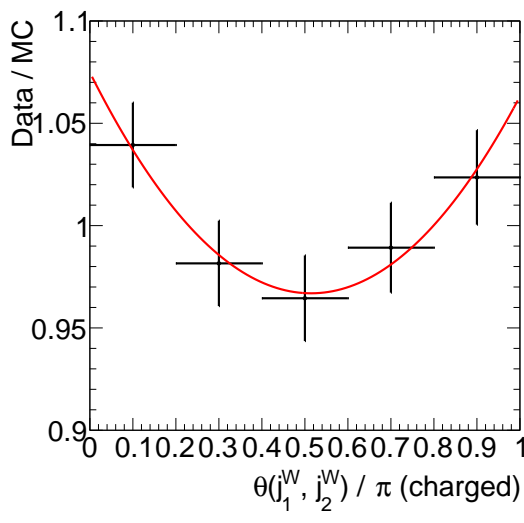
Figure 78: Pull angle distributions in data calculated with all (a) and charged (b) jet constituents and unfolded using MC@NLO (red) or PowHeg+PYTHIA (blue) MC samples.

Figure 82 shows this comparison. The differences between the unfolded reco-level distribution and the reweighted truth-level distribution is taken to be the uncertainty due to non-closure of the unfolding procedure. The unfolding non-closure uncertainty on the all particles and charged particles pull angle



(a)

Figure 79: Charged particles pull angle distribution unfolding using iterative Bayesian and SVD unfolding techniques. The two results are very similar.



(a)

Figure 80: Ratio between the charged particles pull angle distribution in data and the PowHeg+PYTHIA  $t\bar{t}$  monte carlo sample. The ratio has been fitted with a second-order polynomial, shown in red.

888 distributions is shown in the systematic uncertainty breakdown plots in Figures 83(a) and (b).

#### 889 9.4.2 Systematic uncertainty breakdown

890 Figures 83(a) and (b) show breakdowns of the systematic uncertainties on the all particles and charged  
 891 particles pull angles. Details of the experimental systematic uncertainties are presented in Section 8.  
 892 The experimental systematic uncertainties are very small in both distributions. Typically less than 1%  
 893 in every bin. The “MC Gen.” uncertainty is obtained by comparing the default unfolded result with that

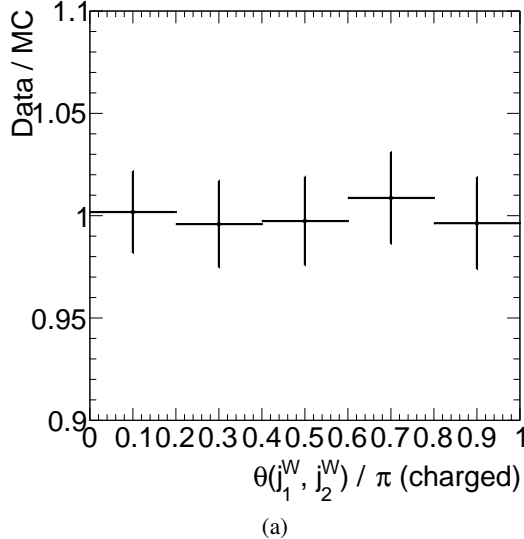


Figure 81: Ratio between the charged particles pull angle distribution in data and the PowHeg+PYTHIA  $t\bar{t}$  monte carlo sample after the MC has been reweighted.

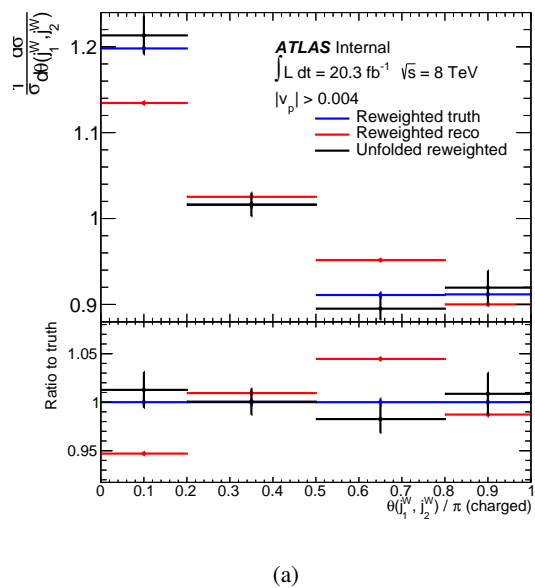


Figure 82: The reweighted reco-level charged particles pull angle distribution (red) is unfolded with the nominal PowHeg+PYTHIA MC (black) and compared to the corresponding reweighted truth-level distribution (blue). The difference between the unfolded and true distributions is assigned as the uncertainty due to the non-closure of the unfolding procedure.

894 obtained when unfolding using MC@NLO to derive the response matrix. The “MC Gen.” uncertainty is  
 895 less than 1% in each bin of the charged particles pull angle, and 1-2% for the all particles pull angle. It  
 896 comparable to, or smaller than, the size of the data statistical uncertainty in each bin. The “Color model”  
 897 uncertainty is estimated by comparing the nominal unfolded result with that obtained when unfolding  
 898 using the color flipped MC samples to derived the response matrix. This is currently the single largest  
 899 source of uncertainty, around 2-4% in each bin of the charged particles pull angle and 4-7% on the all

900 particles pull angle.

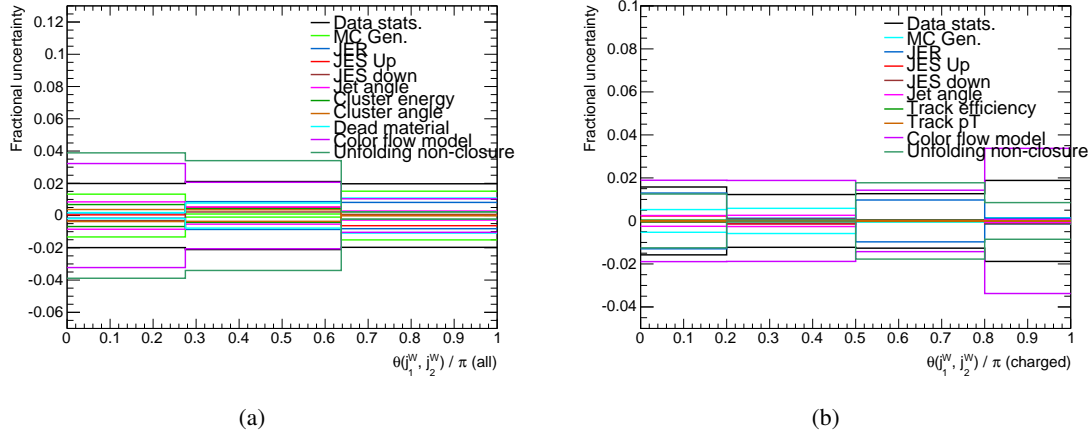


Figure 83: Breakdowns of systematic uncertainties affecting (a) the all particles pull angle and (b) the charged particles pull angle distributions.

## 901 9.5 Unfolded Data

902 Figure 84 shows distributions of the pull angle between the two  $W$  daughter jets calculated using all (a)  
 903 and charged (b) jet constituents. The data were unfolded using MC@NLO and four iterations of Bayesian  
 904 unfolding. Data are compared to predictions from the next-to-leading order generators MC@NLO+HERWIG  
 905 and PowHeg+PYTHIA. Background events are subtracted from the data before unfolding.

Not reviewed, for internal circulation only

Not reviewed, for internal circulation only

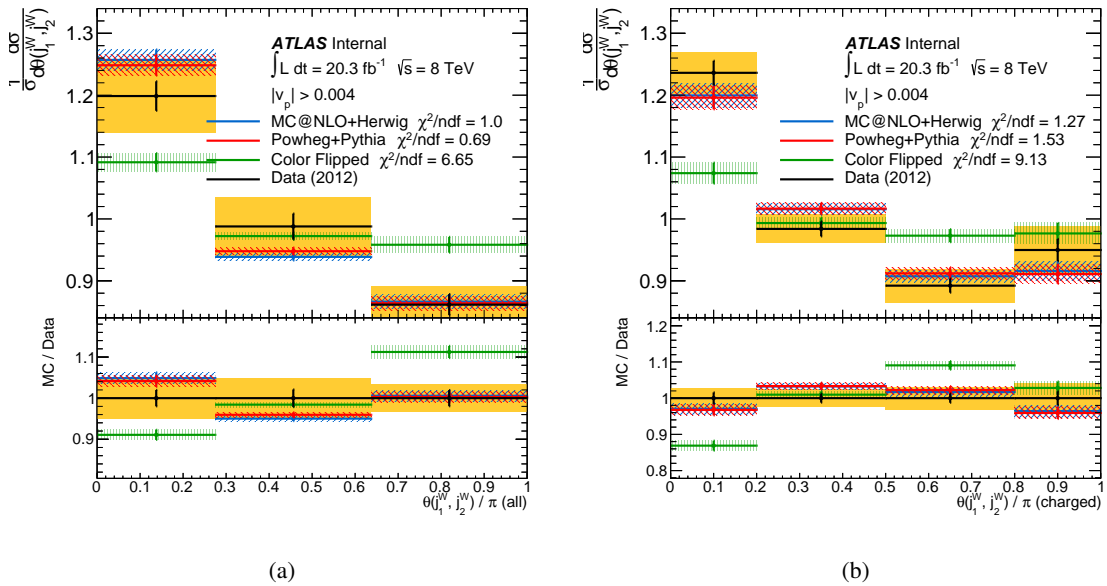


Figure 84: Unfolded pull angle distributions (black) calculated using all (a) and charged (b) jet constituents compared to predictions from MC@NLO+HERWIG (blue), PowHeg+PYTHIA (red) and the color-flipped model (green). Data points are shown in black with the associated statistical uncertainty shown as the black error bars. Yellow bars show the sum-in-quadrature of the statistical and systematic uncertainties.  $\chi^2$  comparisons between the data and each monte carlo prediction show that the data are described better by the Standard Model  $t\bar{t}$  predictions.

## 906 10 Summary and Conclusions

907 Documented in this note is a measurement of the jet pull angle between the hadronic decay products  
908 of  $W$  bosons in  $t\bar{t}$  events. The jet pull angle is a variable constructed to contain information about the  
909 distribution of energy within a jet relative to another jet in the event. As constructed, this angle has  
910 been shown in truth level studies to be sensitive color flow. In addition to unfolding the jet pull angle  
911 distribution, we have compared the unfolded distribution to particle-level models of color flow. The  
912 (charged) pull angle data are in good agreement with the nominal Standard Model color flow model, at  
913  $0.2\sigma$  ( $1.4\sigma$ ) in a Gaussian equivalent  $Z$  score, and are incompatible with an inverted color flow model at  
914  $2.4\sigma$  ( $4.7\sigma$ ). Because we have shown that the pull angle is indeed sensitive to the color flow it will be a  
915 useful tool in determining the color structure of as-of-yet undiscovered resonances in the future.

## 916 11 Todo List

917 The following items are in no particular order.

- 918 • Replace the Herwig dibosons with the Sherpa samples. We have the samples, but have technical  
919 difficulties in the top fiducial package (parses the truth record, which is notoriously different in  
920 Sherpa). Dibosons are a very small background ( $\ll 1\%$ ) and so this will have a negligible impact.
- 921 • Add the subdominant experimental uncertainties on luminosity, muon scale factors, etc. and the  
922 subdominant theory uncertainty on the  $W+jets$  normalization from the charge asymmetry method  
923 uncertainty.
- 924 • Incorporate the experimental uncertainties in the background subtraction.

## 925 References

- 926 [1] JADE Collaboration Collaboration, W. Bartel et al., *Particle Distribution in Three Jet Events*  
 927 *Produced by  $e^+ e^-$  Annihilation*, Z.Phys. **C21** (1983) 37.
- 928 [2] M. Althoff, W. Braunschweig, F. Kirschfink, and H. Martyn, *A study of 3-jet events in  $e^+ e^-$*   
 929 *annihilation into hadrons at 34.6 GeV c.m. energy*, Zeitschrift fr Physik C Particles and Fields **29**  
 930 no. 1, (1985) 29–40. <http://dx.doi.org/10.1007/BF01571375>.
- 931 [3] H. Aihara, M. Alston-Garnjost, J. Bakken, A. Barbaro-Galtieri, A. Barnes, and B. Barnett, *Tests of*  
 932 *models for quark and gluon fragmentation in  $e^+ e^-$  annihilation at  $\sqrt{s} = 29$  GeV*, Zeitschrift fr  
 933 Physik C Particles and Fields **28** no. 1, (1985) 31–44. <http://dx.doi.org/10.1007/BF01550246>.
- 934 [4] H. Aihara, M. Alston-Garnjost, and B. et al., *Tests of Models for Parton Fragmentation by Means*  
 935 *of Three-Jet Events in  $e^+ e^-$  Annihilation at  $s=29$  GeV*, Phys. Rev. Lett. **54** (1985) 270–273.  
 936 <http://link.aps.org/doi/10.1103/PhysRevLett.54.270>.
- 937 [5] (TPC/Two-Gamma) Collaboration, *Comparison of the Particle Flow in  $q\bar{q}g$  and  $q\bar{q}\gamma$  Events in*  
 938  *$e^+ e^-$  Annihilation*, Phys. Rev. Lett. **57** (1986) 945–948.  
 939 <http://link.aps.org/doi/10.1103/PhysRevLett.57.945>.
- 940 [6] P. D. Sheldon, G. H. Trilling, and A. e. a. Petersen, *Comparison of the particle flow in Three-Jet*  
 941 *and radiative Two-Jet Events from  $e^+ e^-$  Annihilation at Ec.m.=29 GeV*, Phys. Rev. Lett. **57** (1986)  
 942 1398–1401. <http://link.aps.org/doi/10.1103/PhysRevLett.57.1398>.
- 943 [7] F. Abe, M. Albrow, D. Amidei, C. Anway-Wiese, G. Apollinari, M. Atac, P. Auchincloss, P. Azzi,  
 944 N. Bacchetta, A. R. Baden, W. Badgett, and M. W. Bailey, *Evidence for color coherence in  $p\bar{p}$*   
 945 *collisions at  $\sqrt{s} = 1.8$  TeV*, Phys. Rev. D **50** (1994) 5562–5579.  
 946 <http://link.aps.org/doi/10.1103/PhysRevD.50.5562>.
- 947 [8] D0 Collaboration Collaboration, B. Abbott et al., *Color coherent radiation in multijet events from*  
 948  *$p\bar{p}$  collisions at  $\sqrt{s} = 1.8$  TeV*, Phys.Lett. **B414** (1997) 419–427, [arXiv:hep-ex/9706012](https://arxiv.org/abs/hep-ex/9706012)  
 949 [*hep-ex*].
- 950 [9] CMS Collaboration Collaboration, S. Chatrchyan et al., *Probing color coherence effects in  $pp$*   
 951 *collisions at  $\text{sqrt}(s) = 7$  TeV*, [arXiv:1311.5815](https://arxiv.org/abs/1311.5815) [*hep-ex*].
- 952 [10] L3 Collaboration Collaboration, P. Achard et al., *Search for color reconnection effects in*  
 953  *$e^+ e^- \rightarrow W^+ W^- \rightarrow$  hadrons through particle flow studies at LEP*, Phys.Lett. **B561** (2003)  
 954 202–212, [arXiv:hep-ex/0303042](https://arxiv.org/abs/hep-ex/0303042) [*hep-ex*].
- 955 [11] DELPHI Collaboration Collaboration, J. Abdallah et al., *Investigation of colour reconnection in*  
 956  *$WW$  events with the DELPHI detector at LEP-2*, Eur.Phys.J. **C51** (2007) 249–269,  
 957 [arXiv:0704.0597](https://arxiv.org/abs/0704.0597) [*hep-ex*].
- 958 [12] L3 Collaboration Collaboration, M. Acciarri et al., *Evidence for gluon interference in hadronic  $Z$*   
 959 *decays*, Phys.Lett. **B353** (1995) 145–154.
- 960 [13] ALEPH Collaboration Collaboration, S. Schael et al., *Test of Colour Reconnection Models using*  
 961 *Three-Jet Events in Hadronic  $Z$  Decays*, Eur.Phys.J. **C48** (2006) 685–698,  
 962 [arXiv:hep-ex/0604042](https://arxiv.org/abs/hep-ex/0604042) [*hep-ex*].

Not reviewed, for internal circulation only

- 963 [14] D0 Collaboration Collaboration, B. Abbott et al., *Evidence of color coherence effects in  $W + \text{jets}$*   
 964 *events from  $p\bar{p}$  collisions at  $\sqrt{s} = 1.8 \text{ TeV}$* , Phys.Lett. **B464** (1999) 145–155,  
 965 arXiv:hep-ex/9908017 [hep-ex].
- 966 [15] J. Gallicchio and M. D. Schwartz, *Seeing in Color: Jet Superstructure*, Phys.Rev.Lett. **105** (2010)  
 967 022001, arXiv:1001.5027 [hep-ph].
- 968 [16] J. Gallicchio, J. Huth, M. Kagan, M. D. Schwartz, K. Black, et al., *Multivariate discrimination*  
 969 *and the Higgs + W/Z search*, JHEP **1104** (2011) 069, arXiv:1010.3698 [hep-ph].
- 970 [17] D0 Collaboration, *Search for the standard-model Higgs boson in the  $ZH \rightarrow b\bar{b}v\bar{v}$  channel in  $6.4 \text{ fb}^{-1}$  of  $p\bar{p}$  collisions at  $\sqrt{s} = 1.96 \text{ TeV}$* , D0 Note 6087-CONF.
- 971 [18] CMS Collaboration, *Search for invisible decays of Higgs bosons in vector boson fusion and*  
 972 *associated ZH production modes*, arXiv:1404.1344 [hep-ex].
- 973 [19] CMS Collaboration, *Search for the standard model Higgs boson produced in association with a  $W$  or a  $Z$  boson and decaying to bottom quarks*, arXiv:1310.3687 [hep-ex].
- 974 [20] D0 Collaboration Collaboration, V. M. Abazov et al., *Measurement of color flow in  $t\bar{t}$  events from*  
 975  *$p\bar{p}$  collisions at  $\sqrt{s} = 1.96 \text{ TeV}$* , Phys.Rev. **D83** (2011) 092002, arXiv:1101.0648 [hep-ex].
- 976 [21] M. Cacciari, G. P. Salam, and G. Soyez, *The Anti- $k(t)$  jet clustering algorithm*, JHEP **0804** (2008)  
 977 063.
- 978 [22] W. Lampl et al., *Calorimeter clustering algorithms: description and performance*,  
 979 ATL-LARG-PUB-2008-002. <https://cdsweb.cern.ch/record/1099735>.
- 980 [23] C. Cojocaru et al., *Hadronic calibration of the ATLAS liquid argon end-cap calorimeter in the*  
 981 *pseudorapidity region  $1.6 < |\eta| < 1.8$  in beam tests*, Nucl. Instrum. Meth. A **531** (2004) 481.
- 982 [24] ATLAS Collaboration, *Pile-up subtraction and suppression for jets in ATLAS*,  
 983 ATLAS-CONF-2013-083 (2013). <https://cds.cern.ch/record/1570994>.
- 984 [25] M. Cacciari, G. P. Salam, and G. Soyez, *The Catchment Area of Jets*, JHEP **0804** (2008) 005.
- 985 [26] ATLAS Collaboration, *Reconstruction and Modeling of Jet Pull with the ATLAS Detector*, In  
 986 Preparation.
- 987 [27] <https://twiki.cern.ch/twiki/bin/viewauth/AtlasComputing/CommonD3PD>.
- 988 [28] ATLAS Collaboration Collaboration, G. Aad et al., *Luminosity Determination in pp Collisions at*  
 989  *$\sqrt{s}=7 \text{ TeV}$  Using the ATLAS Detector at the LHC*, Eur.Phys.J. **C71** (2011) 1630,  
 990 arXiv:1101.2185 [hep-ex].
- 991 [29] ATLAS Collaboration, *Luminosity Determination in pp Collisions at  $\sqrt{s} = 7 \text{ TeV}$  using the*  
 992 *ATLAS Detector in 2011*, ATLAS-CONF-2011-116. <http://cdsweb.cern.ch/record/1376384>.
- 993 [30] ATLAS Collaboration, *The ATLAS Simulation Infrastructure*, Eur. Phys. J. C **70** (2010) 823.
- 994 [31] GEANT4 Collaboration, *Geant4 - a simulation toolkit*, Nuclear Instruments and Methods in  
 995 Physics Research A **506** (2003) 250.
- 996 [32] T. Sjöstrand, S. Mrenna, and P. Skands, *A brief introduction to PYTHIA 8.1*, Comput. Phys.  
 997 Commun. **178** (2008) 852.

Not reviewed, for internal circulation only

- 1000 [33] C. ATLAS, M. Beckingham, M. Duehrssen, E. Schmidt, M. Shapiro, M. Venturi, J. Virzi,  
 1001 I. Vivarelli, M. Werner, S. Yamamoto, and T. Yamanaka, *The simulation principle and*  
 1002 *performance of the ATLAS fast calorimeter simulation FastCaloSim*, Tech. Rep.  
 1003 ATL-PHYS-PUB-2010-013, CERN, Geneva, Oct, 2010.
- 1004 [34] P. Nason, *A new method for combining NLO QCD with shower Monte Carlo algorithms*, JHEP  
 1005 **0411** (2004) 040.
- 1006 [35] S. Frixione, P. Nason, and C. Oleari, *Matching NLO QCD computations with parton shower*  
 1007 *simulations: the POWHEG method*, JHEP **0711** (2007) 070.
- 1008 [36] S. Alioli, P. Nason, C. Oleari, and E. Re, *A general framework for implementing NLO calculations*  
 1009 *in shower Monte Carlo programs: the POWHEG BOX*, JHEP **1006** (2010) 001.
- 1010 [37] H.-L. Lai et al., *New parton distributions for collider physics*, Phys. Rev. D **82** (2010) 074024.
- 1011 [38] J. Gao et al., *The CT10 NNLO Global Analysis of QCD*, arXiv:1302.6246 [hep-ph].
- 1012 [39] S. Frixione and B. R. Webber, *Matching NLO QCD computations and parton shower simulations*,  
 1013 JHEP **0206** (2002) 029.
- 1014 [40] S. Frixione, P. Nason, and B. R. Webber, *Matching NLO QCD and parton showers in heavy flavor*  
 1015 *production*, JHEP **0308** (2003) 007, arXiv:hep-ph/0305252 [hep-ph].
- 1016 [41] G. Corcella et al., *HERWIG 6: An Event generator for hadron emission reactions with interfering*  
 1017 *gluons (including supersymmetric processes)*, JHEP **0101** (2001) 010.
- 1018 [42] J. M. Butterworth, J. R. Forshaw, and M. H. Seymour, *Multiparton interactions in*  
 1019 *photoproduction at HERA*, Z. Phys. C **72** (1996) 637.
- 1020 [43] M. L. Mangano et al., *ALPGEN, a generator for hard multiparton processes in hadronic*  
 1021 *collisions*, JHEP **0307** (2003) 001.
- 1022 [44] ATLAS Top Group, “ATLAS Top Group W+jets MC Recomendation.”  
 1023 <https://twiki.cern.ch/twiki/bin/view/AtlasProtected/TopMC12WjetsSamples>.
- 1024 [45] P. Z. Skands, *Tuning Monte Carlo Generators: The Perugia Tunes*, Phys. Rev. D **82** (2010) 074018.
- 1025 [46] ATLAS Collaboration, *First tuning of HERWIG+JIMMY to ATLAS data*,  
 1026 ATL-PHYS-PUB-2010-014, 2010.
- 1027 [47] A. Altheimer, A. Arce, L. Asquith, J. Backus Mayes, E. Bergeaas Kuutmann, et al., *Boosted*  
 1028 *objects and jet substructure at the LHC. Report of BOOST2012, held at IFIC Valencia, 23rd-27th*  
 1029 *of July 2012*, Eur.Phys.J. **C74** (2014) 2792, arXiv:1311.2708 [hep-ex].
- 1030 [48] J. Alwall, R. Frederix, S. Frixione, V. Hirschi, F. Maltoni, et al., *The automated computation of*  
 1031 *tree-level and next-to-leading order differential cross sections, and their matching to parton*  
 1032 *shower simulations*, arXiv:1405.0301 [hep-ph].
- 1033 [49] A. Alloul, N. D. Christensen, C. Degrande, C. Duhr, and B. Fuks, *FeynRules 2.0 - A complete*  
 1034 *toolbox for tree-level phenomenology*, Comput.Phys.Commun. **185** (2014) 2250–2300,  
 1035 arXiv:1310.1921 [hep-ph].
- 1036 [50] ATLAS JetETmiss CP Group, “JetEtmissRecommendations2012.”  
 1037 <https://twiki.cern.ch/twiki/bin/viewauth/AtlasProtected/JetEtmissRecommendations2012>.

- Not reviewed, for internal circulation only
- 1038 [51] ATLAS Collaboration, *Measurement of the b-tag Efficiency in a Sample of Jets Containing Muons*  
 1039       with  $5 \text{ fb}^{-1}$  of Data from the ATLAS Detector, ATLAS-CONF-2012-043 (2012).  
 1040       <https://cds.cern.ch/record/1435197>.
  - 1041 [52] <https://twiki.cern.ch/twiki/bin/viewauth/AtlasProtected/TopCommonObjects#Muons>.
  - 1042 [53] K. Rehermann and B. Tweedie, *Efficient Identification of Boosted Semileptonic Top Quarks at the*  
 1043       *LHC*, JHEP **1103** (2011) 059, arXiv:1007.2221 [hep-ph].
  - 1044 [54] ATLAS Collaboration Collaboration, *Prospects for top anti-top resonance searches using early*  
 1045       *ATLAS data.*, Tech. Rep. ATL-PHYS-PUB-2010-008, CERN, Geneva, Jul, 2010.
  - 1046 [55] <https://twiki.cern.ch/twiki/bin/viewauth/AtlasProtected/TopCommonObjects#Electrons>.
  - 1047 [56] ATLAS Collaboration, *Performance of Missing Transverse Momentum Reconstruction in ATLAS*  
 1048       *studied in Proton-Proton Collisions recorded in 2012 at 8 TeV*, ATLAS-CONF-2013-082.
  - 1049 [57] SLAC Jet/MET/bTag group, “ProofAna Analysis Framework.”  
 1050       <https://twiki.cern.ch/twiki/bin/view/AtlasSandboxProtected/ProofAna>.
  - 1051 [58] A. Buckley, J. Butterworth, L. Lonnblad, D. Grellscheid, H. Hoeth, et al., *Rivet user manual*,  
 1052       Comput.Phys.Commun. **184** (2013) 2803–2819, arXiv:1003.0694 [hep-ph].
  - 1053 [59] T. Gleisberg, S. Hoeche, F. Krauss, M. Schonherr, S. Schumann, et al., *Event generation with*  
 1054       *SHERPA 1.1*, JHEP **0902** (2009) 007, arXiv:0811.4622 [hep-ph].
  - 1055 [60] T. Carli, A. Lister, A. Glazov, A. Tricoli, W. H. Bell, O. Zenin, A. Buckley, and L. DiCaccio,  
 1056       *Draft proposal for truth particle definitions used in ATLAS*, Tech. Rep.  
 1057       ATL-COM-PHYS-2014-439, CERN, Geneva, May, 2014.
  - 1058 [61] K. Becker et al., *Estimation of Fake Lepton Background for Top Analyses Using the  $\sqrt{s} = 8 \text{ TeV}$*   
 1059       *Dataset*, Tech. Rep. ATL-COM-PHYS-2013-1100, CERN, Geneva, Aug, 2013.
  - 1060 [62] *Update on the jet energy scale systematic uncertainty for jets produced in proton-proton collisions*  
 1061       *at  $\sqrt{s} = 7 \text{ TeV}$  measured with the ATLAS detector*, Tech. Rep. ATLAS-CONF-2011-007, CERN,  
 1062       Geneva, 2011.
  - 1063 [63] M.Begel et al., “JES from Tracks with Release 16.”  
 1064       [https://www.dropbox.com/s/nyit1hwuyaazwbc/trackjesqcd7tev\\_jan11.pdf](https://www.dropbox.com/s/nyit1hwuyaazwbc/trackjesqcd7tev_jan11.pdf).
  - 1065 [64] F. Gescini, *Measurement of Jet Angular Resolution*, Tech. Rep. ATL-COM-PHYS-2013-1467,  
 1066       CERN, Geneva, Oct, 2013.
  - 1067 [65] ATLAS Collaboration Collaboration, G. Aad et al., *Measurement of Dijet Azimuthal*  
 1068       *Decorrelations in pp Collisions at  $\sqrt{s} = 7 \text{ TeV}$* , Phys.Rev.Lett. **106** (2011) 172002,  
 1069       arXiv:1102.2696 [hep-ex].
  - 1070 [66] ATLAS Collaboration Collaboration, G. Aad et al., *ATLAS measurements of the properties of jets*  
 1071       *for boosted particle searches*, Phys.Rev. **D86** (2012) 072006, arXiv:1206.5369 [hep-ex].
  - 1072 [67] ATLAS Collaboration Collaboration, G. Aad et al., *Study of Jet Shapes in Inclusive Jet Production*  
 1073       *in pp Collisions at  $\sqrt{s} = 7 \text{ TeV}$  using the ATLAS Detector*, Phys.Rev. **D83** (2011) 052003,  
 1074       arXiv:1101.0070 [hep-ex].

- Not reviewed, for internal circulation only
- 1075 [68] A. Ahmed et al., *Supporting Document: Measurement of the W cross section and asymmetry in the*  
1076 *electron and muon decay channels at  $\sqrt{s}=7$  TeV*, Tech. Rep. ATL-COM-PHYS-2010-477,  
1077 CERN, Geneva, Jul, 2010. ===*;* this is a backup note for the WZ Xsection analysis (ICHEP  
1078 ATLAS preliminary).
- 1079 [69] M. Begel, M. Campanelli, R. Caputo, R. Dhullipudi, J. Gray, J. Hobbs, J. Hoffman, P. Kreiger,  
1080 H. Ma, S. Majewski, F. Paige, M.-A. Pleier, M. Rijssenbeek, R. Rios, J. Robinson, G. Rosenbaum,  
1081 L. Sawyer, and P. Steinberg, *Azimuthal Decorrelations in Dijet Events at  $\sqrt{s}=7$  TeV*, Tech. Rep.  
1082 ATL-PHYS-INT-2010-110, CERN, Geneva, Sep, 2010.
- 1083 [70] *A measurement of single hadron response using data at  $\sqrt{s} = 8$  TeV with the ATLAS detector*,  
1084 Tech. Rep. ATL-PHYS-PUB-2014-002, CERN, Geneva, Mar, 2014.
- 1085 [71] ATLAS b-tagging CP Group, “Flavour Tagging calibration results in 2014.”  
1086 <https://twiki.cern.ch/twiki/bin/view/AtlasProtected/BTagCalib2014>.
- 1087 [72] A. Armbruster, K. Kroeninger, B. Malaescu, and F. Spano, *Practical considerations for unfolding*,  
1088 Tech. Rep. ATL-COM-PHYS-2014-277, CERN, Geneva, Apr, 2014.
- 1089 [73] <https://twiki.cern.ch/twiki/bin/viewauth/AtlasProtected/StandardModelUnfolding>.
- 1090 [74] G. D’Agostini, *Improved iterative Bayesian unfolding*, arXiv:1010.0632 [hep-ph] (2010).
- 1091 [75] T. Adye, *Unfolding algorithms and tests using RooUnfold*, arXiv:1105.1160  
1092 [physics.data-an].
- 1093 [76] The ATLAS Collaboration, *A Measurement of WZ Production in Proton-Proton Collisions at*  
1094  *$\sqrt{s} = 7$  TeV with the ATLAS Detector*, ATL-COM-PHYS-2012-488 (2012).

1095 **A Simulation Details**

1096 **A.1 QCD octet electroweak boson**

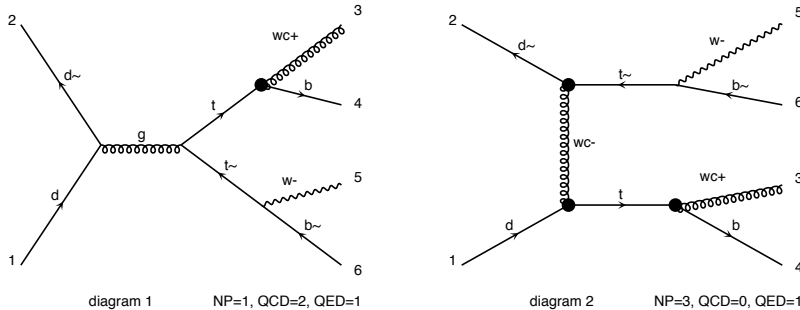


Figure 85: Example leading order Feynman diagrams for the  $W$  octet Madgraph model.

1097 This section describes an alternative exotic color flow simulation. As briefly described earlier, the  
 1098  $W$  boson color octet is created as a ‘complete’ phenomenological model, with Feynman rules specified  
 1099 at leading order. See Fig. 85 for example leading order Feynman diagrams. These rules are converted  
 1100 into a MadGraph [48] model using FeynRules 2.0.25 [49] in the form of Universal FeynRules Output  
 1101 (UFO). For instance, the part of the decay.py file corresponding to the new  $W_c$  ( $c$  for color) particle has  
 1102 the following form.

```
Decay_WC_plus_ = Decay(name = 'Decay_WC_plus_',
  particle = P.WC_plus_,
  partial_widths = {(P.c,P.b_tilde):'((-2*CLq2x3**2*gL**2*MB**2 ...
  (P.c,P.d_tilde):'((-2*CLq2x1**2*gL**2*MC**2 ...
  (P.c,P.s_tilde):'((-2*CLq2x2**2*gL**2*MC**2 ...
  (P.t,P.b_tilde):'((-2*CLq3x3**2*gL**2*MB**2 ...
  (P.t,P.d_tilde):'((-2*CLq3x1**2*gL**2*MD**2 ...
  (P.t,P.s_tilde):'((-2*CLq3x2**2*gL**2*MS**2 ...
  (P.u,P.b_tilde):'((-2*CLq1x3**2*gL**2*MB**2 ...
  (P.u,P.d_tilde):'((-2*CLq1x1**2*gL**2*MD**2 ...
  (P.u,P.s_tilde):'((-2*CLq1x2**2*gL**2*MS**2 ...
```

1103 The LHE header contains the information about the quantum numbers of the new particle. One  
 1104 cannot use a  $W'$  PDG ID, since many showering models have the  $W'$  preprogrammed as a color singlet and  
 1105 thus these programs will not run properly or at all. For convenience, we have chosen the PDG ID 99.

```
#=====
# QUANTUM NUMBERS OF NEW STATE(S) (NON SM PDG CODE)
#=====

Block QNUMBERS 99 # wc+
  1 3 # 3 times electric charge
  2 3 # number of spin states (2S+1)
  3 8 # color rep (1: singlet, 3: triplet, 8: octet)
  4 1 # Particle/Antiparticle distinction (0=own anti)
```

Not reviewed, for internal circulation only

Below is the LHE output for the generation of a single event's hard scatter. The production here is specified by  $pp > tt \sim wc + bw - b$  after importing the new model. Note that the  $W$  octet contains two color quantum numbers (as it is an octet) so when it decays to quarks, the two quarks will not be color connected in the sense that one will not have the anti-color of the other.

```
<event>
  8   0  0.2145307E-02  0.2273129E+03  0.7818609E-02  0.1135623E+00
     21  -1   0   0  504  502  0.00000000000E+00  0.00000000000E+00  0.23317214730E+03  0.23317214730E+03  0.00000000000E+00  0.  -1.
     21  -1   0   0  502  503  0.00000000000E+00  0.00000000000E+00  -0.22088504908E+03  0.22088504908E+03  0.00000000000E+00  0.  -1.
    -6   2   1   2   0  503  0.12569990089E+03  0.77501171926E+02  0.10399245352E+02  0.22673646609E+03  0.17173929084E+03  0.  0.
     6   2   1   2  504   0  -0.12569990089E+03  0.77501171926E+02  0.18878528714E+01  0.22732073029E+03  0.17281277065E+03  0.  0.
    99   1   4   4  504  501  -0.44270369871E+02  0.97393941160E+02  -0.31200716041E+02  0.13707975191E+03  0.79824358925E+02  0.  0.
     5   1   4   4  501   0  -0.81429531015E+02  0.19892769234E+02  0.33088568912E+02  0.90240978386E+02  0.46999998093E+01  0.  1.
   -24   1   3   3   0   0  0.15867742991E+03  0.53876402780E+02  0.67963364763E+01  0.18573990418E+03  0.79824358925E+02  0.  0.
    -5   1   3   3   0  503  -0.32977529023E+02  0.23624769146E+02  0.36029088760E+01  0.40996561908E+02  0.46999998093E+01  0.  1.
```

Figure 86: The LHE output of one event generated with the color octet model using MadGraph.

Currently, this model is implemented in our private (PYTHIA) showering framework. Fig. 87 shows the distribution of the pull angle between the  $W$  daughter candidate jets for the  $W$  octet model and the SM  $W$  singlet. The  $W$  daughter jets are chosen as the two jets of  $p_T > 25$  GeV with invariant mass closest to  $m_W \sim 80$  GeV. As expected, the SM  $W$  jets show a significant peak near zero indicating a color connection, whereas the octet model is mostly uniform indicating a lack of a color connection (since the jets are connected to other objects in the event). ATLAS implementation and validation is ongoing. As of v0.3 of this note, we are still integrating the  $W$  octet model into the ATLAS MC production system. This will not be ready in time for a preliminary result.

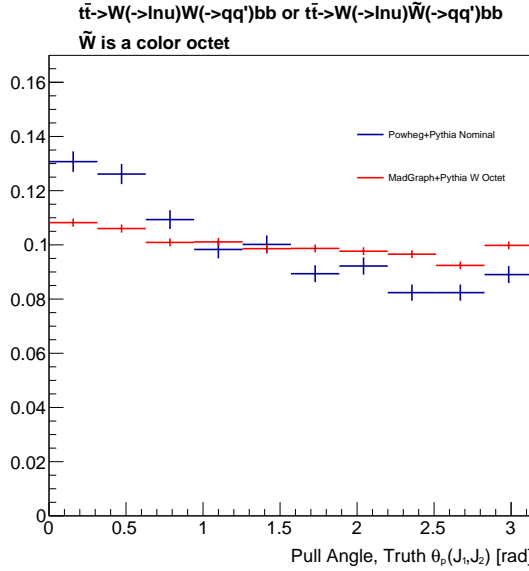


Figure 87: The pull angle distribution between the  $W$  daughters (determined by the jets of  $p_T > 25$  GeV with invariant mass closest to 80 GeV) for a color octet  $W$  and a color singlet model.

## 1118 B Additional Experimental Studies

### 1119 B.1 Jet Origin Correction

1120 As part of the most recent recommendations from the JetETmiss CP group, the  $\eta$  of jets is corrected so  
 1121 that the angle is computed with respect to the primary vertex and not the geometric center of the detector,  
 1122 see Fig. 88 for a schematic description. The practical implication of the origin correction is that the jet  
 1123  $\eta$  resolution, the RMS of the  $\Delta\eta$  between reconstructed and truth jets in simulation, is much improved.  
 1124 This is shown clearly in Fig. 89, where it is shown that the  $\phi$  resolution is largely unaffected by the origin  
 1125 correction, but the  $\eta$  resolution is a factor of two better.

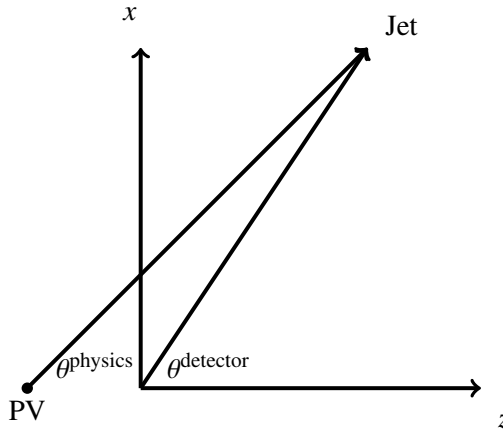


Figure 88: A schematic diagram of the origin correction. The quantity  $\theta^{\text{detector}}$  is the angle in the  $zx$  plane measured with respect to the geometric center of the detector, whereas the ‘true’  $\theta^{\text{physics}}$  that we desire is offset and based from the primary vertex (PV).

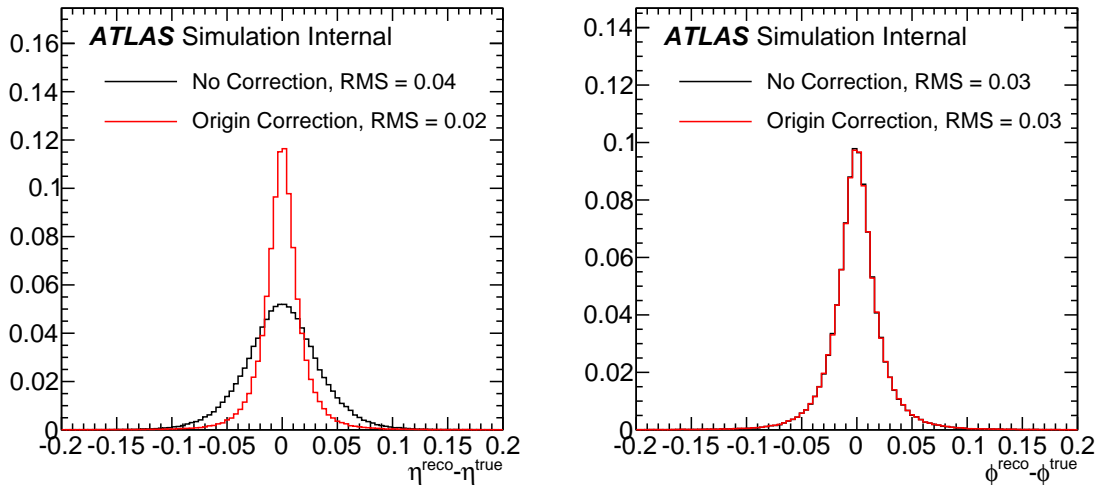


Figure 89: The  $\eta$  (left) and  $\phi$  (right) jet angular resolution before and after the jet origin correction. The resolution is defined as the RMS of the  $\Delta\eta$  or  $\Delta\phi$  between the reconstructed jet and the  $\Delta R < 0.4$  matched truth jets.

Not reviewed, for internal circulation only

Dedicated performance studies [26] have shown that the jet pull angle is very sensitive to the jet angular resolution. Figure 90 are from Ref. [26] and show the impact of reducing the angular resolution on the jet pull angle. The right plot of Fig. 90 shows that for the track based pull, which uses the calorimeter jet axis, the reconstructed distribution is much closer to the truth distribution after the calorimeter jet axis is replaced with the truth jet axis ( $J_1$  Truth,  $B_1$  Truth). The pull angle for this study is  $\theta_P(J_1, B_1)$ , which is the pull angle between the leading  $W$  daughter jet and the leading  $b$  jet, which are expected to have no color connection and thus the distribution is uniform at truth level. The angular resolution of the ‘lever’ jet (in this case  $B_1$ ) does not impact the distribution all that much (compare the dotted versus solid lines in Fig. 90 for a fixed color). The peak at  $\pi/2$  is a characteristic of the resolution smearing and is explained in detail in Ref. [26].

The calorimeter pull angle in Fig. 90 shows a much different transformation when the angular resolution is ‘removed.’ As with the track pull angle, the angular resolution of the lever arm jet does not impact the distribution. However, there is a significant change in the shape when the truth axis for  $J_1$  is replaced with the truth jet axis. Part of the reason for the big change in shape is that while the jet center is now corrected, the jet constituents are not corrected. Thus, there is essentially a random smearing applied that differentiates the ‘angular scale’ of the clusters and the jet. This was not present for the track pull angle, because its constituents, inner detector tracks, are measured independently of the calorimeter jet position.

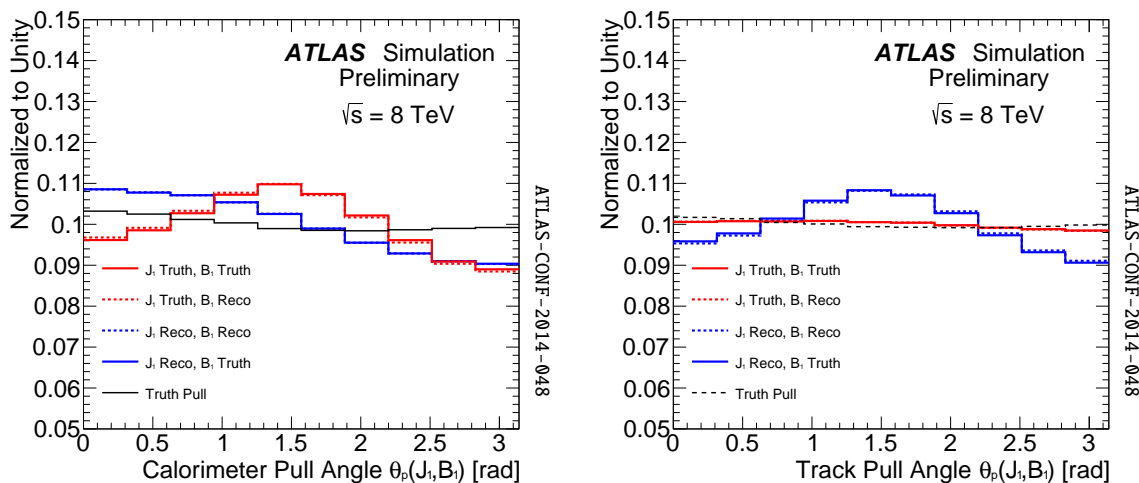


Figure 90: The impact of ‘removing’ the jet angular resolution by replacing reconstructed axis with truth matched axes (figure from Ref. [26]).

Figures 91 and 92 compare the pull angle between the  $W$  daughter jets used in the present measurement before and after the origin correction. The difference in the charged pull angle is rather small (Fig. 92), but there is a significant change in shape for the all particles pull angle (Fig. 91), which is qualitatively the same as in Fig. 90. This suggests that we need to further consider correcting the constituents. In principle, each cluster could be origin corrected just as the jet axis is corrected. However, since the angle that the clusters make with the jet is already small, the correction  $\Delta\eta^{\text{jet}} = \eta^{\text{detector}} - \eta^{\text{physics}}$  is a good approximation for the correction. Furthermore, shifting the clusters by  $\Delta r^{\text{jet}}$  preserves the pull vector, since it depends on differences between constituents and the jet center. Figures 93 and 94 compare the pull angle between the  $W$  daughter jets used in the present measurement before and after the origin correction applied to both clusters and to the jet axis. By construction, there is no effect on the track pull (Fig. 94), but the all particles pull (Fig. 93) has been restored to the shape expected before any correction.

1155 The full correction for clusters that is used in the analysis is described in Sec. 4.1.2 and Sec. 4.1.1.

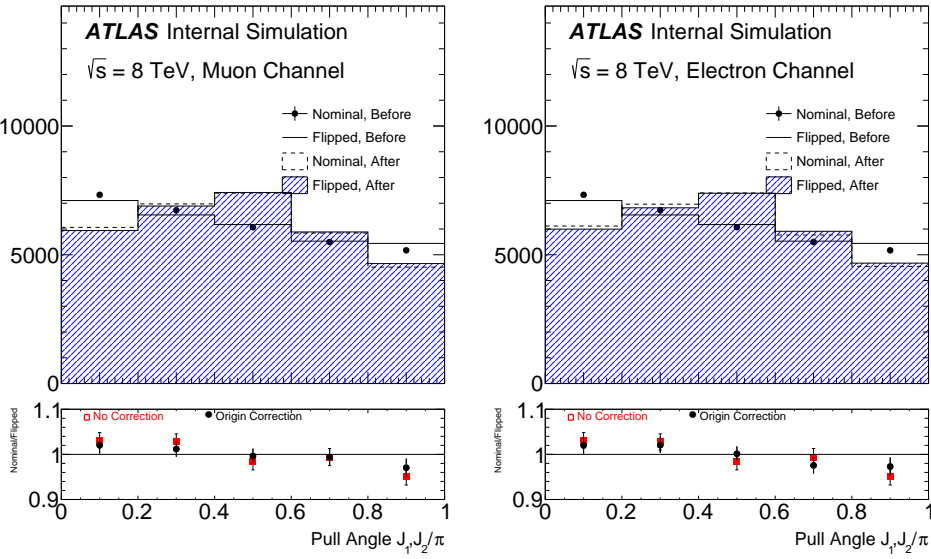


Figure 91: The all particles pull angle in simulation for the muon channel (left) and the electron channel (right) before any jet origin calibration (point with error bar and solid line) and after the origin correction is applied for the jet centers only (dashed line and filled area). The lines called ‘nominal’ are for the un-flipped  $t\bar{t}$  samples while the ‘flipped’ areas correspond to the color flipped samples. An important comparison is how the difference between flipped and un-flipped changes before and after the correction. This is shown in the bottom panel.

Not reviewed, for internal circulation only

Not reviewed, for internal circulation only

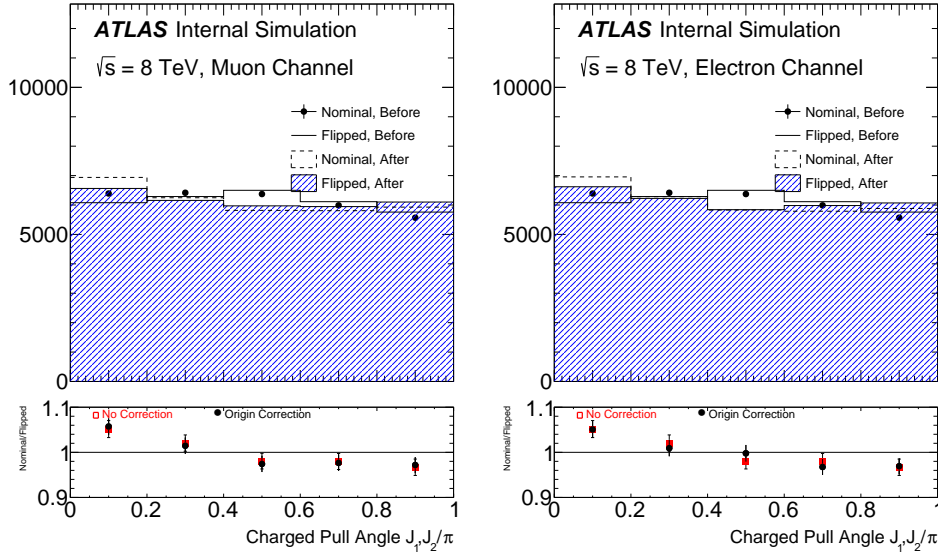


Figure 92: The charged particles pull angle in simulation for the muon channel (left) and the electron channel (right) before any jet origin calibration (point with error bar and solid line) and after the origin correction is applied for the jet centers only (dashed line and filled area). The lines called ‘nominal’ are for the un-flipped  $t\bar{t}$  samples while the ‘flipped’ areas correspond to the color flipped samples. An important comparison is how the difference between flipped and un-flipped changes before and after the correction. This is shown in the bottom panel.

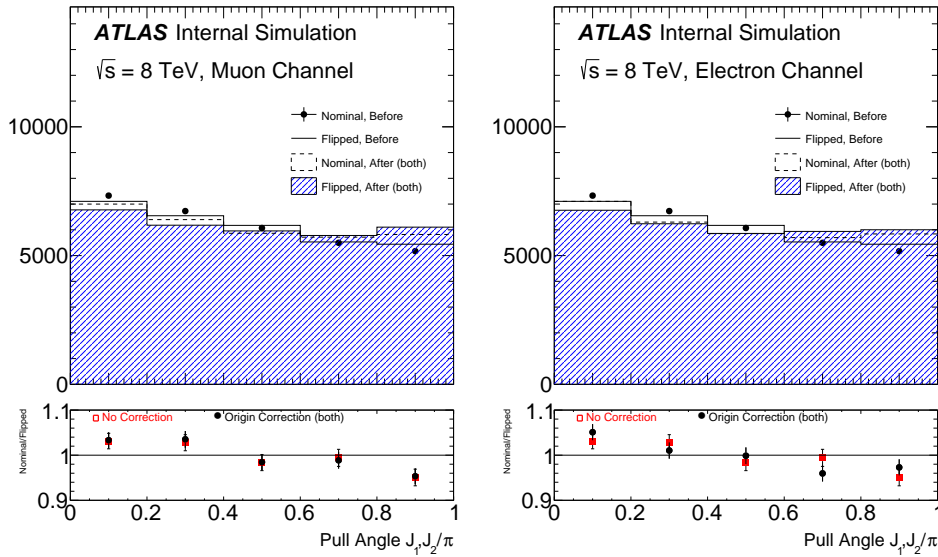


Figure 93: The all particles pull angle in simulation for the muon channel (left) and the electron channel (right) before any jet origin calibration (point with error bar and solid line) and after the origin correction is applied for both jets and constituents (dashed line and filled area). The lines called ‘nominal’ are for the un-flipped  $t\bar{t}$  samples while the ‘flipped’ areas correspond to the color flipped samples. An important comparison is how the difference between flipped and un-flipped changes before and after the correction. This is shown in the bottom panel.

Not reviewed, for internal circulation only

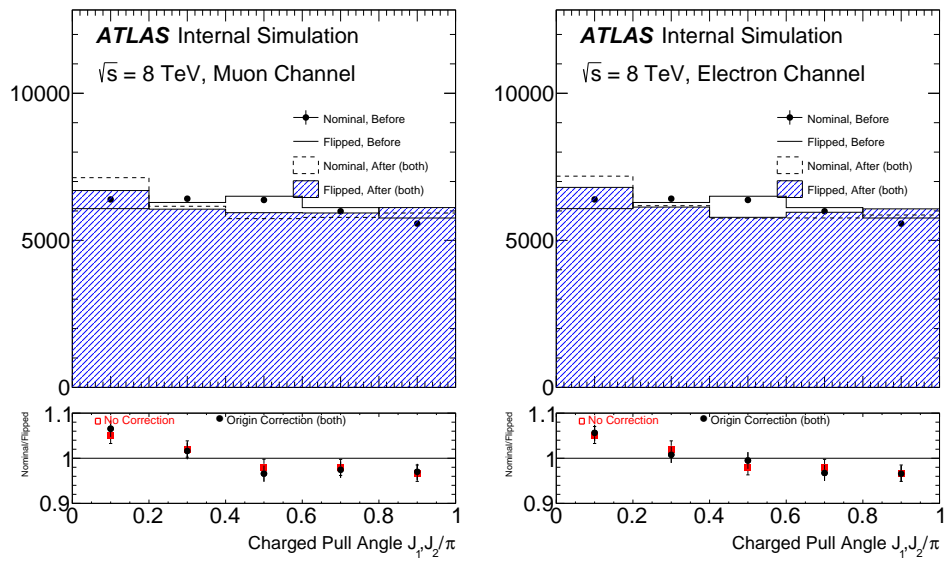


Figure 94: The charged particles pull angle in simulation for the muon channel (left) and the electron channel (right) before any jet origin calibration (point with error bar and solid line) and after the origin correction is applied for both jets and constituents (dashed line and filled area). The lines called ‘nominal’ are for the un-flipped  $t\bar{t}$  samples while the ‘flipped’ areas correspond to the color flipped samples. An important comparison is how the difference between flipped and un-flipped changes before and after the correction. This is shown in the bottom panel.

## 1156 B.2 Jet Angular Resolution from Track Jets

1157 One way to determine the jet angular resolution uncertainty is to use the resolution of the calorimeter jet  
 1158 to track jet angular distance, which has been measured in ATLAS [64]. We can use the uncertainties on  
 1159 this measurement of the  $p_T$  and  $\eta$  dependent resolutions for our estimate of the angular resolution on the  
 1160 jet axes used in the measurement. We do not use this as the baseline uncertainty for several reasons:

- 1161 1. The uncertainty in the jet angular resolution should be very correlated with the uncertainties on the  
 1162 clusters. The uncertainty computed with the track jet difference would treat these uncertainties as  
 1163 fully correlated.
- 1164 2. The uncertainties determined with the track jet method are very large, which seems to be partially  
 1165 due to limited MC statistics in the measurement [64]. Many further studies would be required  
 1166 before the track jet method could be a viable option.

1167 The rest of this section describes how one would extract the jet angular resolution uncertainty from the  
 1168 measurement. Reference [64] reports a measurement of the resolutions (RMS or  $\sigma$ ) of  $\Delta\phi = \phi_{\text{track jet}} -$   
 1169  $\phi_{\text{calo jet}}$  and  $\Delta\eta = \eta_{\text{track jet}} - \eta_{\text{calo jet}}$ . We can write

$$\sigma_{\Delta\phi} \sim \sqrt{\sigma_{\phi_{\text{track jet}}}^2 + \sigma_{\phi_{\text{calo jet}}}^2}. \quad (14)$$

1170 Which then gives us an estimate

$$\sigma_{\sigma_{\Delta\phi}}^2 \sim \sigma_{\sigma_{\phi_{\text{track jet}}}}^2 \sigma_{\phi_{\text{track jet}}}^2 + \sigma_{\sigma_{\phi_{\text{calo jet}}}}^2 \sigma_{\phi_{\text{calo jet}}}^2 \quad (15)$$

1171 Compared to the calorimeter angular resolution uncertainty, the track jet angular resolution uncertainties  
 1172 should be second order. Thus, we can approximate  $\sigma_{\sigma_{\phi_{\text{track jet}}}} \ll \sigma_{\sigma_{\phi_{\text{calo jet}}}}$  to arrive at an estimate:

$$\sigma_{\sigma_{\phi_{\text{calo jet}}}}(p_T, \eta) \sim \frac{\sigma_{\sigma_{\Delta\phi}}(p_T, \eta) \sigma_{\Delta\phi}(p_T, \eta)}{\sigma_{\phi_{\text{calo jet}}}(p_T, \eta)}. \quad (16)$$

1173 Then, if we want to smear the jet axis so that the resolution  $\sigma \rightarrow \sigma + \sigma_\sigma$ , we must solve for  $s$ :

$$\sigma^2 + s^2 = (\sigma + \sigma_\sigma)^2, \quad (17)$$

1174 which has the solution

$$s = \sqrt{2\sigma\sigma_\sigma + \sigma_\sigma^2}. \quad (18)$$

1175 The first step is to extract the resolutions  $\sigma_{\eta, \phi}$ . Note that the uncertainties derived here are **only**  
 1176 **valid when the jet origin correction has been applied**. This is because without the correction, the  $\eta$   
 1177 resolution is much worse in the MC than in the data; thus, before the origin correction one must apply  
 1178 a correction before assessing uncertainties. With the origin correction, no correction is required and the  
 1179 factor  $s$  from Eq. 18 which we derive below can be directly applied.

1180 Figure 95 shows the scaling of the  $\eta$  and  $\phi$  jet resolution with  $p_T$ . Simple functional forms ( $a +$   
 1181  $b/p_T$ ) are chosen to match the low  $p_T$  and asymptotic  $p_T$  behavior of the resolution. The  $\eta$  dependence  
 1182 of the resolution is shown in Fig. 96.

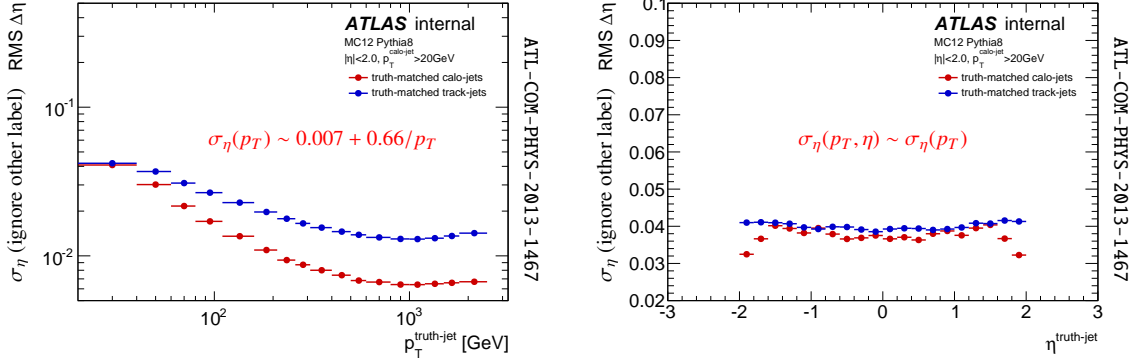


Figure 95: The  $p_T$  dependance of the  $\eta$  (left) and  $\phi$  (right) jet angular resolution. Plots are from ATL-COM-PHYS-2013-1467 with the functional form determined here overlaid on top.

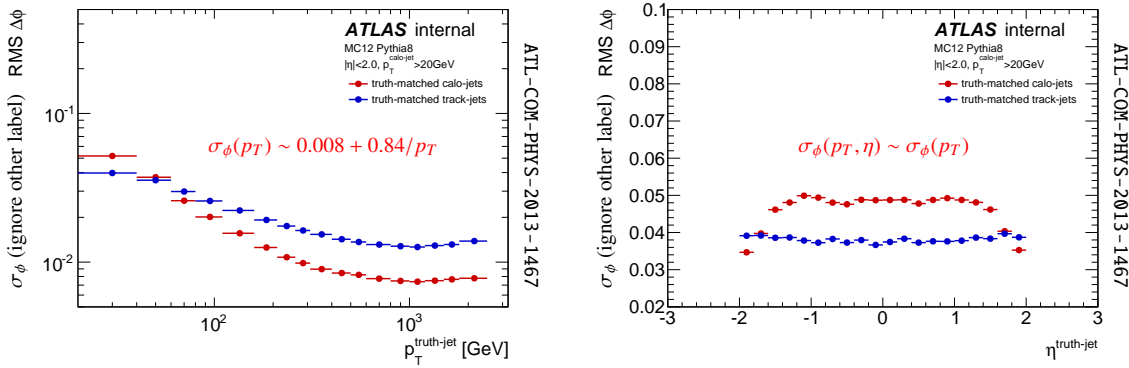


Figure 96: The  $\eta$  dependance of the  $\eta$  (left) and  $\phi$  (right) jet angular resolution. Plots are from ATL-COM-PHYS-2013-1467 with the functional form determined here overlaid on top.

While the resolutions  $\sigma_{\Delta\phi}$  and  $\sigma_{\Delta\eta}$  are  $p_T$  dependent, the uncertainty on these resolutions is fairly stable at about 10% (See Fig. 97):

$$\sigma_{\sigma_{\Delta\eta}}(p_T) \sim 0.1 \times \sigma_{\Delta\eta} \quad (19)$$

$$\sigma_{\sigma_{\Delta\phi}}(p_T) \sim 0.1 \times \sigma_{\Delta\phi} \quad (20)$$

The uncertainty on the  $\Delta\eta$  resolution is largely independent of  $\eta$  (see Fig. 98):

$$\sigma_{\sigma_{\Delta\eta}}(p_T, \eta) \sim \sigma_{\sigma_{\Delta\eta}}(p_T) \quad (21)$$

$$\sigma_{\sigma_{\Delta\phi}}(p_T, \eta) \sim \sigma_{\sigma_{\Delta\phi}}(p_T) \quad (22)$$

The same issue about the  $\eta$  resolution as with the  $p_T$  dependance: we can see  $\sigma_{\Delta\eta}(p_T, \eta) \sim \sigma_{\Delta\eta}(p_T)$  is not quite true without the origin correction. Tabulating the formulas according to Eq. 15 leads to functional forms for the angular resolution uncertainties shown in Eq. 23.

$$\sigma_{\sigma_{\eta_{\text{calo jet}}}(p_T, \eta)} \sim \frac{0.1 \times \left(0.01 + \frac{1.1 \text{ GeV}}{p_T}\right)^2}{\left(0.006 + \frac{0.66 \text{ GeV}}{p_T}\right)} \quad (23)$$

$$\sigma_{\sigma_{\phi_{\text{calo jet}}}(p_T, \eta)} \sim \frac{0.1 \times \left(0.015 + \frac{1.2 \text{ GeV}}{p_T}\right)^2}{\left(0.008 + \frac{0.84 \text{ GeV}}{p_T}\right)} \quad (24)$$

1189 The actual amount to smear each jet angle by, following Eq. 18, are then given by

$$\sigma_{\text{smear } \eta}(p_T, \eta) = \sqrt{2\sigma_{\sigma_{\eta_{\text{calo jet}}}}(p_T, \eta)\sigma_{\eta_{\text{calo jet}}}(p_T, \eta) + \sigma_{\sigma_{\eta_{\text{calo jet}}}}^2(p_T, \eta)} \quad (25)$$

$$\sigma_{\text{smear } \eta}(p_T, \eta) = \sqrt{2\sigma_{\sigma_{\phi_{\text{calo jet}}}}(p_T, \eta)\sigma_{\phi_{\text{calo jet}}}(p_T, \eta) + \sigma_{\sigma_{\phi_{\text{calo jet}}}}^2(p_T, \eta)}. \quad (26)$$

1190 Figure 99 shows plots of the fractional angular resolution uncertainty  $\sigma_\sigma/\sigma$  and also the amount by  
1191 which the angles should be smeared,  $\sigma_{\text{smear}}$ .

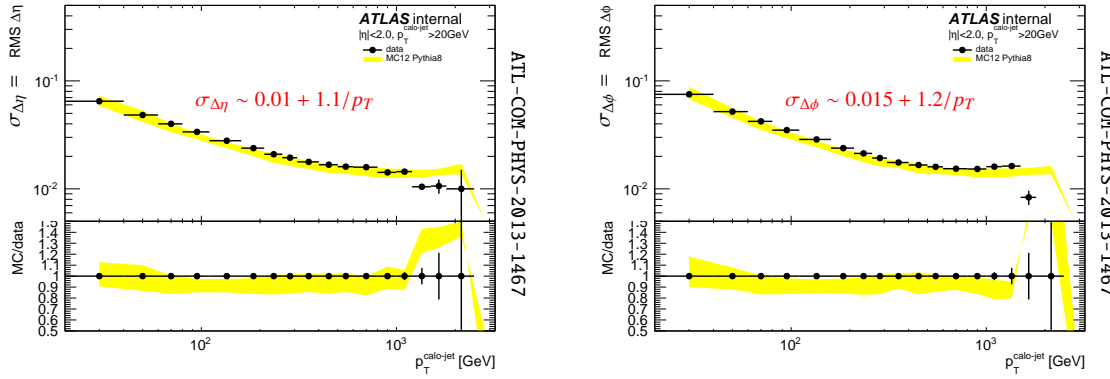


Figure 97: The  $p_T$  dependance of the  $\Delta\eta$  (left) and  $\Delta\phi$  (right) resolutions and uncertainties. Plots are from ATL-COM-PHYS-2013-1467 with the functional form determined here overlaid on top.

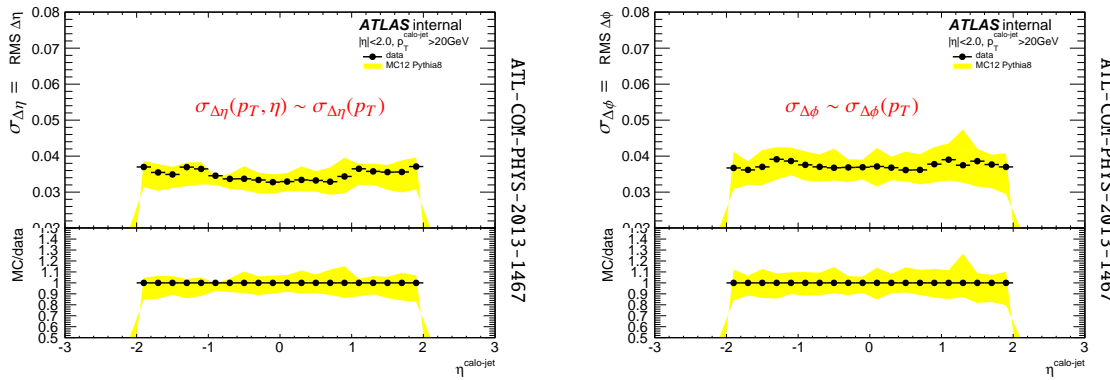


Figure 98: The  $\eta$  dependance of the  $\Delta\eta$  (left) and  $\Delta\phi$  (right) resolutions and uncertainties. Plots are from ATL-COM-PHYS-2013-1467 with the functional form determined here overlaid on top.

Not reviewed, for internal circulation only

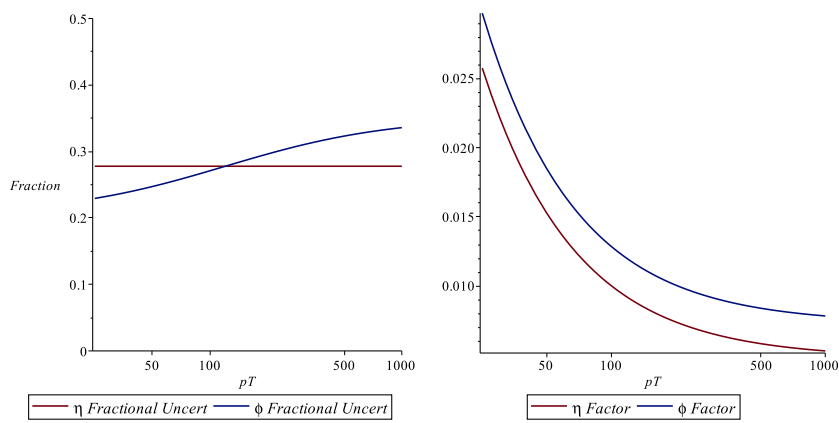


Figure 99: The fractional angular resolution uncertainty  $\sigma_\sigma/\sigma$  (left) and also the amount by which the angles should be smeared,  $\sigma_{\text{smear}}$  (right).

### 1192 B.3 Cluster Energy Modeling for non-isolated Tracks

1193 Figures 100, 101, and 102 show the energy distribution of clusters comparing the data and  $t\bar{t}$  MC in  
 1194 various bins of the cluster isolation. The MC is normalized by area to the data. An isolation moment of  
 1195 one is very isolated and zero is very not-isolated.

Not reviewed, for internal circulation only

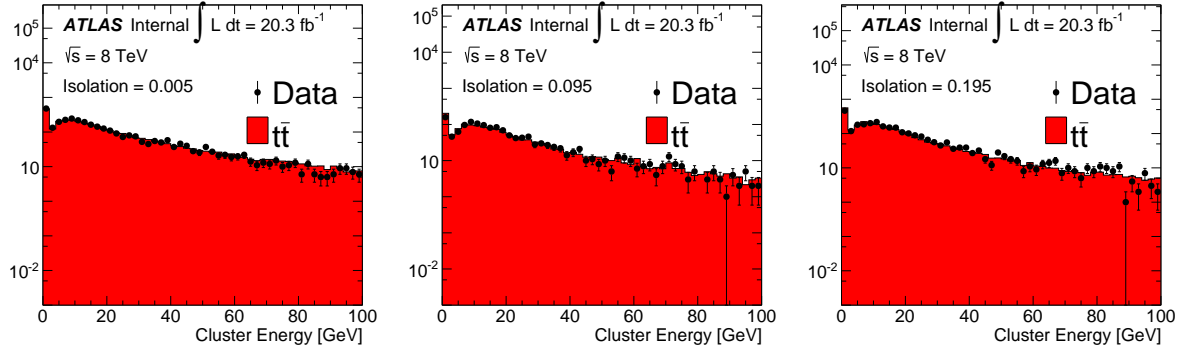


Figure 100: The energy distribution of clusters for non-isolated clusters.

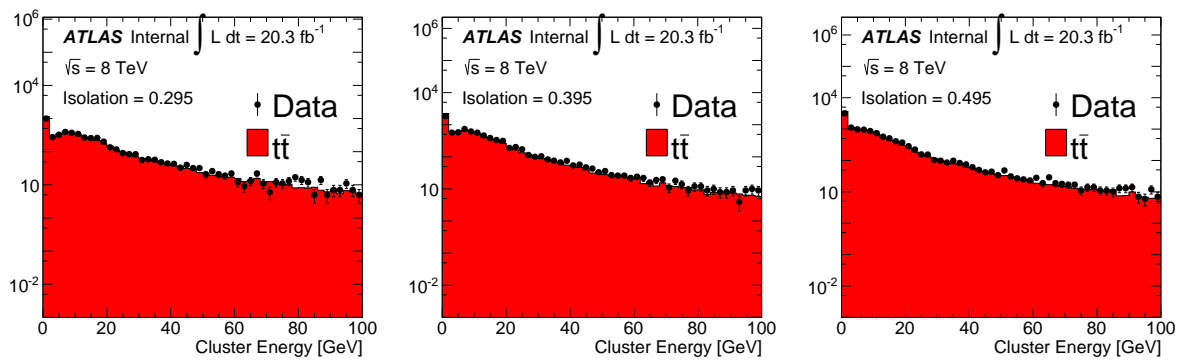


Figure 101: The energy distribution for clusters in the middle of the isolation distribution.

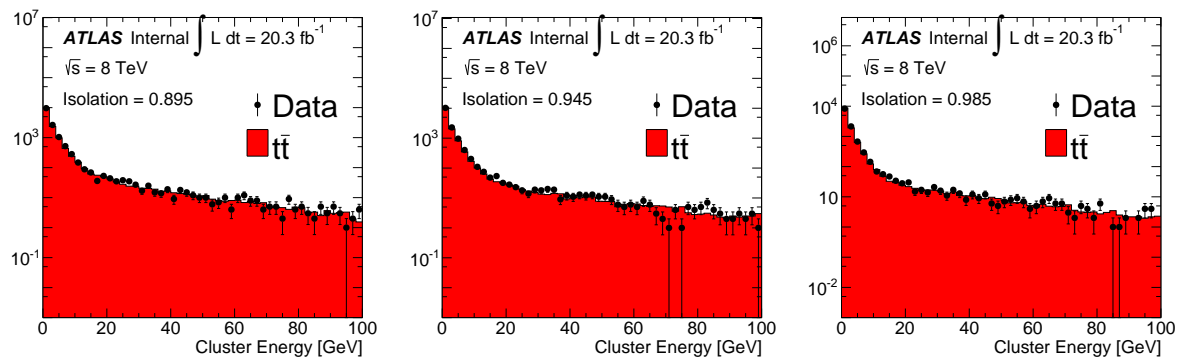


Figure 102: The energy distribution for well-isolated clusters.